

NUMERICAL INVESTIGATION OF THE FLUIDELASTIC INSTABILITY OF TWO-PHASE
FLOW IN A PARALLEL TRIANGULAR TUBE ARRAY

by

Omar Sadek

A thesis submitted to the
School of Graduate and Postdoctoral Studies in partial
fulfillment of the requirements for the degree of

Doctor of Philosophy in Mechanical Engineering

Faculty of Engineering and Applied Science

University of Ontario Institute of Technology (Ontario Tech University)

Oshawa, Ontario, Canada

May 2021

© Omar Sadek, 2021

Thesis Examination Information

Submitted by: **Omar Sadek**

Doctor of Philosophy in Mechanical Engineering

Thesis title:

Numerical investigation of the fluidelastic instability of two-phase flow in a parallel triangular tube array

An oral defense of this thesis took place on May 4, 2021 in front of the following examining committee:

Examining Committee:

Chair of Examining Committee	Dr. Sayyed Ali Hussein
Research Supervisor	Dr. Atef Mohany
Research Co-supervisor	Dr. Marwan Hassan, University of Guelph
Examining Committee Member	Dr. Martin Agelin-Chaab
Examining Committee Member	Dr. Brendan MacDonald
University Examiner	Dr. Ahmad Barari
External Examiner	Dr. Njuki Mureithi, École Polytechnique de Montréal

The above committee determined that the thesis is acceptable in form and content and that a satisfactory knowledge of the field covered by the thesis was demonstrated by the candidate during an oral examination. A signed copy of the Certificate of Approval is available from the School of Graduate and Postdoctoral Studies.

Abstract

Steam generators are always susceptible to vibrations induced by the flow in either the shell or tube sides. The fluidelastic instability phenomenon (FEI) is considered one of the most devastating flow excitations since it may cause excessive wear and structural failure to the tubes in a short time span, yet the phenomenon is not well understood. The U-bend region of the steam generator is very prone to the FEI and the flow in this region is characterized by a two-phase nature. Most studies of this phenomenon have been carried out experimentally on specific tube arrays at certain conditions, and design guidelines were developed based on them. Thus, a need emerges to provide a model to predict the onset of FEI at any flow condition or geometry.

Firstly, this research focuses on developing and validating a model to predict the onset of FEI in two-phase flows. Secondly, the work attempts to address the problem of varying the flow's angle of attack inside the U-bend, known as flow's approach angle, and how it influences the onset of the instability. Finally, due to the curvature of the tubes inside the U-bend region, they are not tuned to a single natural frequency, a case known as frequency detuning. The presented work inspects the effect of frequency detuning and the key parameters controlling its influence.

In this study, a model based on Computational Fluid Dynamics was proposed to simulate the onset of FEI. The model was validated and tested for a two-phase air-water flow in parallel triangular array against FEI in transverse and streamwise directions. Predictions obtained were in good agreement with experiments in the literature. Furthermore, the influence of flow approach angle was relatively understood and an efficient approximate semi-analytical model was successfully developed to predict the FEI dynamic forces at any flow angle. Finally, isolation of FEI mechanisms was carried out. Generally, frequency detuning was found to stabilize the tube bundle and its effect is sensitive to the mass-damping parameter. This work is a step forward towards a better understanding and an accurate prediction of the onset of FEI in the U-bend region.

Keywords:

Fluidelastic instability; steam generators; two-phase; approach angle; frequency detuning.

Author's Declaration

I hereby declare that this thesis consists of original work of which I have authored. This is a true copy of the thesis, including any required final revisions, as accepted by my examiners.

I authorize the University of Ontario Institute of Technology (Ontario Tech University) to lend this thesis to other institutions or individuals for the purpose of scholarly research. I further authorize University of Ontario Institute of Technology (Ontario Tech University) to reproduce this thesis by photocopying or by other means, in total or in part, at the request of other institutions or individuals for the purpose of scholarly research. I understand that my thesis will be made electronically available to the public.

Omar Sadek

Statement of Contributions

I hereby certify that the work described in Chapter 3 has been published as:

Sadek, O., Mohany, A., & Hassan, M. (2018). Numerical investigation of the cross flow fluidelastic forces of two-phase flow in tube bundle. *Journal of Fluids and Structures*, 79, 171-186. <https://doi.org/10.1016/j.jfluidstructs.2017.11.009>

And the work described in Chapter 4 has been published as:

Sadek, O., Mohany, A., & Hassan, M. (2020). Numerical simulation of streamwise fluidelastic instability of tube bundles subjected to two-phase cross flow. *Journal of Fluids and Structures*, 92, 102816. <https://doi.org/10.1016/j.jfluidstructs.2019.102816>

While the work presented in Chapter 5 has been submitted to the Journal of fluids and structures as:

Sadek, O., Mohany, A., & Hassan, M. (2021). The prediction of fluidelastic forces in triangular tube bundles subjected to a two-phase flow: The effect of the flow approach angle. Submitted to the *Journal of Fluids and Structures*.

And the work in Chapter 6 has been submitted to the Journal of pressure vessel technology as:

Sadek, O., Mohany, A., & Hassan, M. (2021). The mechanisms of fluidelastic instability and the effect of frequency detuning in triangular tube bundles subjected to a two-phase flow. Submitted to the *Journal of pressure vessel technology*.

In all these works, I performed numerical simulations, analysis, and writing the manuscripts.

Acknowledgement

I would like to express my deep gratitude to my supervisors for their continuous help in my work and guidance to complete this thesis. I would also like to thank them for their valuable advices in the different contexts of this document and their tips.

My heartfelt thanks are due to Dr. Atef Mohany for his great help, support, and patience during the time of this work. And many thanks to Dr. Marwan Hassan for his valuable remarks, efforts and guidance during the various stages of this thesis work.

Special thanks go to all my colleagues in the research team: Nadim Arafa, Mahmoud Shaaban, and Moamen Abdelmwigoud for the support, encouragement, and guiding through my work in the research. I managed to made it through because of the joyful and supportive attitude we all shared in the team.

Finally, I would like to express my great appreciation to my family and my friends for their continuous care, patience, tolerance, encouragement, and support.

Table of Contents

Thesis Examination Information.....	i
Abstract.....	ii
Author’s Declaration.....	iii
Statement of Contributions	iv
Acknowledgement	v
List of Tables	x
List of Figures	xi
List of abbreviations	xvi
Chapter 1. Background	1
1.1. Introduction	1
1.2. Objectives.....	3
1.3. Thesis outline	4
Chapter 2. Literature Review	6
2.1. Models of fluidelastic instability.....	7
2.2. Fluidelastic instability in two-phase flow	10
2.3. Uncertainties in Fluidelastic instability measurements.....	11
2.4. Fluidelastic instability in U-bend region.....	12
2.5. Numerical techniques	16
2.6. Summary	18
Chapter 3. Numerical investigation of the cross flow fluidelastic forces of two-phase flow in tube bundle.....	20
3.1. Introduction	21
3.2. Modeling and governing equations	24
3.3. Unsteady fluid/structure interaction modeling.....	27

3.3.1.	Hybrid Analytical-CFD Model	27
3.3.2.	Direct Flow/Structure Coupling.....	29
3.4.	Flow Domain Simulation	29
3.5.	Results and discussion.....	32
3.5.1.	Sensitivity analyses.....	32
3.5.2.	Data validation	36
3.6.	Unsteady forces in two-phase flow	38
3.7.	Stability Threshold Prediction.....	39
3.7.1.	Hybrid Analytical-CFD Model	39
3.7.2.	Direct Flow/Structure Simulation	42
3.8.	Conclusions	44
Chapter 4. Numerical simulation of streamwise fluidelastic instability of tube bundles subjected to two-phase cross flow.....		46
4.1.	Introduction	47
4.2.	System modelling.....	50
4.2.1.	Flow field model	50
4.2.2.	Hybrid analytical-flow field model.....	53
4.2.3.	Direct flow/structure coupling model	55
4.2.4.	Dynamic mesh treatment	55
4.2.5.	Flow domain and setup	56
4.3.	Results and discussion.....	60
4.4.	Conclusion.....	74
Chapter 5. The prediction of fluidelastic forces in triangular tube bundles subjected to a two-phase flow: The effect of the flow approach angle.....		76
5.1.	Introduction	77
5.2.	Model Description.....	79

5.2.1. Instability analysis	82
5.3. Results	85
5.3.1. Flow forces.....	85
5.3.2. Flow visualization.....	92
5.3.3. FEI force - Approach angle in a semi analytical model.....	94
5.3.4. Stability analysis	98
5.4. Conclusion.....	102
Chapter 6. The mechanisms of fluidelastic instability and the effect of frequency detuning in triangular tube bundles subjected to a two-phase flow	104
6.1. Introduction	105
6.2. Methodology	107
6.2.1. Flow domain	108
6.2.2. Numerical flow and two-phase models	108
6.2.3. Harmonic oscillator model.....	111
6.2.4. Flow/Structure coupling.....	111
6.2.5. FEI mechanisms isolation.....	114
6.3. Results and discussions	114
6.3.1. Transverse FEI.....	116
6.3.2. Streamwise FEI.....	124
6.4. Conclusion.....	128
Chapter 7. Summary and Conclusions.....	130
7.1. Thesis summary.....	130
7.2. Conclusions	131
7.3. Original contributions	133
7.3.1. Numerical investigation of the cross flow fluidelastic forces of two-phase flow in tube bundle	133

7.3.2. Numerical simulation of streamwise fluidelastic instability of tube bundles subjected to two-phase cross flow	133
7.3.3. The prediction of fluidelastic forces in triangular tube bundles subjected to a two-phase flow: The effect of the flow approach angle	133
7.3.4. The mechanisms of fluidelastic instability and the effect of frequency detuning in triangular tube bundles subjected to a two-phase flow.....	134
7.4. Recommendations for future work.....	134
Bibliography	136
Appendix A.....	147
A.1. Numerical investigation of the cross flow fluidelastic forces of two-phase flow in tube bundle.....	147
A.2. Numerical simulation of streamwise fluidelastic instability of tube bundles subjected to two-phase cross flow.....	148

List of Tables

Table 4.1: Phase angle of the kernel mode shape. Experiments from Violette et al. (Violette et al., 2006), $\alpha = 80\%$, at the onset of instability.....	73
Table 5.1: Conversion between the approach angle and the orientation angle of the flow.	79
Table 6.1: Deviation percent of each tube's natural frequency from the nominal 8 Hz value for the studied parallel triangular array. $D = 38\text{ mm}$ and $P/D = 1.5$	116

List of Figures

Figure 1.1: Response of a cylinder in an array subjected to cross flow. Adapted from (Païdoussis 1983).	2
Figure 2s.1: Jet switching between tubes and its effect on the size of downstream wakes, (Roberts, 1962a)	6
Figure 2.2: Stability diagram for single row array having a pitch-to-diameter ratio of 1.41. (Connors, 1978)	8
Figure 2.3: Onset of fluidelastic instability for a single flexible tube in a parallel triangular array following the model of Price and Paidoussis (Price and Paidoussis, 1984).	9
Figure 2.4: Steam generator for the CANDU system (Garland, 2014).	13
Figure 2.5: Simulated velocity field distribution at the central plane in a typical CANDU steam generator working at 100% load (Mohany et al., 2012).	14
Figure 2.6: Effect of frequency detuning on streamwise stability constant (Olala & Mureithi, 2016).	16
Figure 3.1: Single degree of freedom simple harmonic damped oscillator under unsteady external force.	29
Figure 3.2: 2-D flow domain for a parallel triangular tube array.	30
Figure 3.3: Mesh topology and refinement around the tubes.	32
Figure 3.4: Mesh sensitivity at $U_R = 9.5$: (a) 0% air void fraction, (b) 60% air void fraction.	33
Figure 3.5: Time step sensitivity at $U_R = 6.6$: (a) 0% air void fraction, (b) 60% air void fraction.	34
Figure 3.6: Contours of absolute slip in the vicinity of tube bundle.....	35
Figure 3.7: Mean slip variation with the bubble Sauter-mean diameter at inlet.....	36
Figure 3.8: Comparison between experimental measurements of (Pettigrew et al., 2005) and simulation results for 50% air void fraction and $U = 5$ m/s for the temporal average of: (a) air void fraction, (b) air bubble velocity [m/s].....	37
Figure 3.9: Lift force coefficient and phase acting on tube C when it oscillates in x-dir compared to the experimental data of (Sawadogo & Mureithi, 2014). For 0% air void fraction: (a) lift force, (b) phase angle.....	38

Figure 3.10: Experimental and simulated lift force coefficient magnitude and phases at different air void fractions for tube c: (a) lift coefficient, (b) phase angle.	39
Figure 3.11: Simulated lift force coefficients magnitude and phases at different air void fractions: (a and b) N tube, (c and d) S tube, (e and f) NE tube, (g and h) SE tube.	40
Figure 3.12: Stability map comparison between the simulation and experiments for 0% air void fraction.	42
Figure 3.13: Stability threshold map obtained from the two-phase flow unsteady forces simulations vs. experimental data from Pettigrew (1989) for air–water flow.....	42
Figure 3.14: Time response of tube C and for 60% air void fraction at $Ur = 2.8$	43
Figure 3.15: Stability threshold map obtained from the two-phase flow unsteady forces simulations and Direct Flow/Structure coupling vs. experimental data from (Pettigrew, Tromp, et al., 1989) for air-water flow.....	44
Figure 4.1: Flow domain.....	58
Figure 4.2: Unstructured mesh pattern for $P/D = 1.3$ domain: a) in the vicinity of tube array, b) between the tubes and the baffle plates.....	60
Figure 4.3: Effect of the turbulence model on the simulated fluidelastic forces relative to the motion of tube C. $P/D = 1.3$, $\alpha = 80\%$, $Ur = 10$: a) Force coefficient, b) phase angle.	61
Figure 4.4: Effect of oscillation frequency on the dynamic fluidelastic forces. $P/D = 1.5$, $\alpha = 60\%$. Experimental data were extracted from (Olala & Mureithi, 2015): a,b) tube C, c,d) tube SW.....	63
Figure 4.5: Effect of the void fraction of the fluidelastic forces and its phase from the tube motion. $P/D = 1.5$, $\alpha = 60\%$. Experimental data were extracted from (Olala & Mureithi, 2015): a,b) tube C, c,d) tube SW.	64
Figure 4.6: Fluidelastic forces and phase angles on Tube C at different void fractions. $P/D=1.7$: a, b) tube C; c, d) tube N; e, f) tube NW; g, h) tube SW; i, j) tube S.	66
Figure 4.7: Fluidelastic forces and phase angles on Tube C at different void fractions. $P/D=1.3$: a, b) tube C; c, d) tube N; e, f) tube NW; g, h) tube SW; i, j) tube S.	68
Figure 4.8: Effect of P/D ratio on fluidelastic force magnitude and phase angle at 60% air: a,b) tube C; c,d) tube SW.....	69

Figure 4.9: Velocity and streamlines of flow in tube bundles with $P/D = 1.3$ (a, b c, d), 1.5 (e, f, g, h), and 1.7 (i, j, k, l) at different instants in the cycle. $\alpha = 80\%$, $Ur = 10$	71
Figure 4.10: Streamwise stability map and validation with experimental data for $P/D = 1.5$	72
Figure 4.11: Streamwise stability map and the effect of pitch-to-diameter ratio.	73
Figure 4.12: Time signals for tubes C, N, NW, SW, and S obtained from the direct flow/structure coupling model at a streamwise FEI. $P/D = 1.5$, $\alpha = 80\%$	74
Figure 5.1: Depiction of the approach angle (ψ) and the orientation angle (θ) of the flow.	79
Figure 5.2: CFD domains for the orientation angles of different tube arrays.	80
Figure 5.3: Analogy of fluid added mass, damping, and stiffness elements to a classical mechanical vibration system.	83
Figure 5.4: The effect of the air void fraction on the fluidelastic forces, F_{xx} acting on Tube C at a 45° orientation (the forces are in the x-dir when Tube C oscillates in the x-dir): a) the force coefficient magnitude, and b) the phase angle.	86
Figure 5.5: Variations in simulated Reynolds numbers at a unity gap velocity of $U_g = 1 \text{ m/s}$ against the air void fraction.	87
Figure 5.6: Variations in the fluidelastic force F_{xx} at high air void fraction values, a 45° orientation, and a $Ur = 15$, for Tube E: a) force coefficient magnitude, and b) phase angle.	88
Figure 5.7: Fluidelastic forces F_{xx} acting on Tube C for different orientation angles. The forces are in the x-dir when Tube C oscillates in the x-dir.	89
Figure 5.8: Fluidelastic forces F_{yy} acting on Tube C for different orientation angles. Forces are in the y-dir when Tube C oscillates in the y-dir.	90
Figure 5.9: Average water flow streamlines for 30° , 37.5° , 45° , 55° and 60° orientation angles at $Ur = 3$. Blue indicates a normal triangular array-like flow pattern, while red is a parallel triangular array-like flow pattern.	93
Figure 5.10: Percentage of parallel triangular flow: a) Hexagonal cell boundary, and b) variation of parallel flow with orientation angle.	94
Figure 5.11: Transformation of coordinates: a) global and local coordinates, b) force vectors, and c) oscillation amplitudes.	96
Figure 5.12: The simulated vs. the calculated semi-analytical fluidelastic force in the x-dir for Tube C, at a $0\% \sim 80\%$ air void fraction. The force coefficient and the phase angle are for:	

a) & b) a 37.5° orientation angle; c) & d) a 45° orientation angle; and e) & f) a 55° orientation angle.....	98
Figure 5.13: The simulated vs. the calculated semi-analytical fluidelastic force in the y-dir for Tube C, at a 0% ~ 80% air void fraction. The force coefficient and the phase angle are for: a) & b) a 37.5° orientation angle; c) & d) a 45° orientation angle; and e) & f) a 55° orientation angle.....	99
Figure 5.14: FEI stability maps for different flow approach angles: a) 30° orientation (normal triangle), b) 37.5° orientation, c) 45° orientation, d) 55° orientation, and e) 60° orientation (parallel triangle). The experimental values are extracted from Weaver & Fitzpatrick (1988).....	100
Figure 5.15: Effect of the flow approach angle on the FEI at MDP= 0.0148. The experimental data are obtained from Yeung & Weaver (1983).	101
Figure 6.1: Flow domain.....	109
Figure 6.2: Structural harmonic oscillator model	111
Figure 6.3: Sketch of the U-bend region in a steam generator showing the gradual increase in tube span Li in the outward radial direction.	115
Figure 6.4: Stability map due to different mechanisms for a flexible kernel in the cross-flow direction (x-dir.). No detuning applied (DM = 0).	117
Figure 6.5: Modal-to-natural frequency ratio due to two different mechanisms for a flexible kernel in the cross-flow direction (x-dir.). No detuning applied (DM = 0).	118
Figure 6.6: Mode shapes at the onset of transverse FEI at MDP= 1 & 5 for the three cases of: a,b) damping mechanism, c,d) stiffness mechanism, and e,f) damping and stiffness mechanisms combined. No detuning applied (DM = 0)	119
Figure 6.7: Effect of frequency detuning on the cross-flow (x-dir) FEI Mechanisms: a, c, e) stability map; b, d, f) modal frequency ratio. Detuning increases with detuning multiplier DM	121
Figure 6.8: Effect of frequency detuning on the cross-flow (x-dir) FEI stability threshold at MDP = 10 : a) damping mechanism, b) stiffness mechanism, and c) damping+stiffness mechanisms.	122
Figure 6.9: Stability map and modal frequency ratio due to two different mechanisms for a flexible kernel in the streamwise direction (y-dir.). No detuning applied (DM = 0).	124

Figure 6.10: Mode shapes at the onset of transverse FEI at MDP= 0.38 (water flow) for the three cases of: a) damping mechanism, b) stiffness mechanism, and c) damping and stiffness mechanisms combined. No detuning was applied ($\mathbf{DM} = \mathbf{0}$).....	126
Figure 6.11: Effect of frequency detuning on the streamwise (\mathbf{y} -dir) FEI Mechanisms: a, c, e) stability map; b, d, f) modal frequency ratio. Detuning increases with detuning multiplier \mathbf{DM}	127
Figure A.1: Screenshot of permission to use the presented journal article in Chapter 3.....	147
Figure A.2: Screenshot of permission to use the presented journal article in Chapter 4.....	148

List of abbreviations

A :	Oscillation amplitude [m].
a :	Volume fraction [-].
c :	Force coefficient [-].
C :	Damping coefficient per unit length [N.s/m ²].
D :	Tube diameter [m].
DM :	Detuning multiplier [-].
f_n :	Natural frequency [Hz].
F :	Force per unit length [N/m].
\mathbf{g} :	Gravity field vector [m/s ²].
k :	Stiffness per unit length [N/m ²].
K :	Stiffness matrix per unit length [N/m ²].
m :	Mass per unit length [kg/m].
MDP :	Mass-damping parameter [-].
M :	Mass matrix per unit length [kg/m].
P :	Pitch [m].
R :	Radius of curvature of tubes in the U-bend region [-].
Re :	Reynold's number [-].
\mathbf{u} :	Flow velocity vector [m/s].
U :	Gap velocity [m/s].
U_r :	Reduced velocity [-].
U_∞ :	Free stream flow velocity [m/s].
x, y :	Spatial coordinates in lift and drag directions [m].
z :	Generalized motion vector [m].

$\alpha_{ij}, \beta_{ij}, \sigma_{ij}, \tau_{ij}$:	Flow added mass coefficients [kg/m ³].
$\alpha'_{ij}, \beta'_{ij}, \sigma'_{ij}, \tau'_{ij}$:	Flow added damping coefficients [-].
$\alpha''_{ij}, \beta''_{ij}, \sigma''_{ij}, \tau''_{ij}$:	Flow added stiffness coefficients [-].
Γ :	Dynamic mesh diffusion coefficient [-].
γ :	Axes rotation angle [°].
δ :	Damping logarithmic decrement parameter [-].
ϕ :	Phase angle [°].
ζ :	Damping ratio [-].
θ :	Orientation angle [°].
ϑ :	Modal angle [°].
Π :	Parallel flow ratio [-].
ρ :	Density [kg/m ³].
μ :	Dynamic viscosity [N.s/m ²].
ν :	Kinematic viscosity [m ² /s].
ψ :	Approach angle [°].
ω :	Angular frequency of the oscillating tube [rad/s].
χ :	Interfacial area concentration [1/m].

Subscripts:

a :	Added flow effect.
c :	Cell.
f :	Flow.
k :	Phase.
m :	Mixture.
p :	Dispersed secondary phase.

- q : Continuous primary phase.
- s : Structure.
- t : Turbulent.

Chapter 1. Background

1.1. Introduction

With the continuing increase of the energy's demand, more efficient and reliable components are sought in power generation facilities. This need is translated into higher efficiency and performance requirements for heat transfer equipment, such as feedwater heaters and steam generators. Consequently, it leads to operation at higher flow speeds. However, the maximum flow speeds are not only controlled by the optimum thermal consideration; other factors such as safety and reliability of designs are major parameters which cannot be ignored. For example, in the Canada Deuterium Uranium (CANDU) type of nuclear power plants, the steam generator is used to transfer the heat from the heavy water in the primary loop (i.e., reactor loop) to the water in the secondary loop (i.e., power generation loop), and generates the steam to run the turbines. Therefore, the steam generators work as the last barrier to prevent the radioactive particles from contaminating the secondary loop since the two working fluids shall not be in a direct contact. Thus, the prevention of leakage or any possible damage to the structure of the steam generators during their operation should be accounted for in the design stage of such devices. One of the factors determining the life span of steam generators is the fluid-dynamic forces. The coupling of these forces with the mechanical flexibility of the structure establishes a serious limit to the maximum flow speeds attainable for safe operation. Such coupling is referred to as Flow-Induced Vibration (FIV).

FIV occurs when the flow passes past a structure and exerts a flow-dependent force on it. Every structure has a degree of flexibility and therefore vibration occurs. This vibration is generally due to one of three phenomena: turbulent buffeting, Vortex-Induced Vibration (VIV) due to vortex shedding or Strouhal periodicity, or Fluidelastic Instability (FEI) (Ziada et al., 2018). A fourth mechanism was also mentioned which is the acoustic resonance (Pettigrew et al., 1991). However, the latter is reported only to occur for gaseous flows. Figure 1.1 shows the relative tube response in an array as a result of a single-phase cross flow. The upstream flow is generally turbulent. The

random pressure and velocity fluctuations in the flow create random forces on the tube. Due to the elasticity of the tube, it vibrates, and the response in this case is called turbulent buffeting. It is characterized by random and small-amplitude vibrations. This type of FIV occurs for parallel and cross-flows relative to the tubes in a tube bundle.

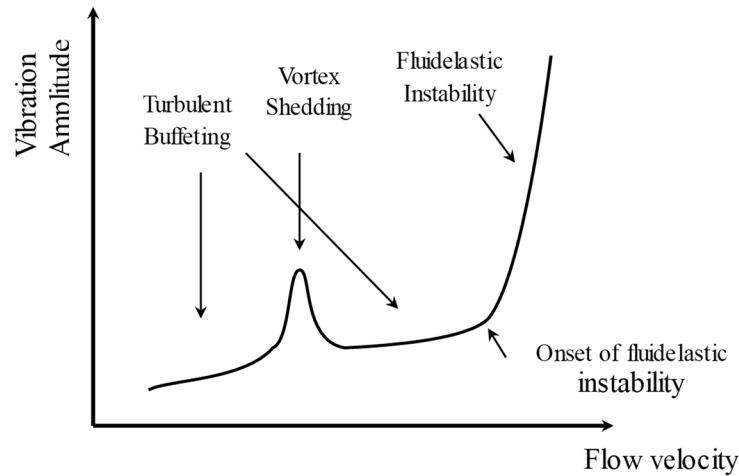


Figure 1.1: Response of a cylinder in an array subjected to cross flow. Adapted from Païdoussis (1983).

On the other hand, the vibration due to vortex shedding is organized and characterized by larger amplitudes. When the fluid flows around a tube, periodic vortices are shed from the tube. These vortices alternate and form a street of vortices in the wake region past the tube, known as Karman Vortex street. The shedding frequency of the vortices is primarily a function of the flow velocity. As it approaches the natural frequency of the structure, a lock-in occurs where the frequency of the vortices is locked into the natural frequency of the tube causing vibrational resonance. The high amplitude of the vibration of the tube is observed until the increase in flow velocity is sufficient for the vortex shedding to exit the lock-in region. This phenomenon is common for flows around bluff bodies.

The third mechanism is fluidelastic instability, which takes place generally at higher flow velocity than vortex shedding and is a self-excited vibration mechanism. When a flow crosses the tubes at a certain velocity, the amplitude of tube oscillation due to buffeting becomes significant compared to the diameter of tube, and then this oscillation introduces a change to the flow field around the tube creating more fluctuating forces on tube. This in turn may establish a positive feedback cycle between the oscillating tube and changing flow field which results in more energy being

transferred to the tube than can be dissipated by its own damping. Hence, a large increase in the amplitude of tube oscillation takes place with a slight increase in flow velocity. The onset of fluidelastic instability is this critical flow velocity at which this rapid increase in the vibration amplitude is observed.

The three aforementioned phenomena contribute to the damage of heat exchangers in different weights during the operation time of the equipment. Turbulent buffeting causes tubes-to-supports fretting wear and thinning. Such damage is serious considering the long lifetime of the equipment. Vortex-induced vibration and fluidelastic instability causes larger vibration amplitude than turbulent buffeting and leads to serious damage in a shorter time span. However, fluidelastic instability is considered the most dangerous FIV mechanism because of the rapid increase in the vibration amplitude and the very short time failure, typically days rather than years (M. Païdoussis et al., 2010). The failure of the tubes is from tube-to-support and tube-to-tube fretting wear as well as clashing of the tubes. In two-phase flow, VIV is observed to be weak due to the disturbance of the wake structure caused by the gaseous phase bubbles (Feenstra et al., 2003; Sun et al., 2009).

1.2. Objectives

As shown in this brief introduction, the steam generators are essential equipment in the nuclear power generation. Since fluidelastic instability is the most devastating FIV mechanism, a safe and reliable design of such a component must avoid reaching the velocity at which this mechanism occurs. In a typical steam generator used in both fossil and nuclear power plants, the shell side flow is moving across the tube bundle at the U-bend region, making it more susceptible to the fluidelastic instability. The flow in the U-bend is of a two-phase nature. Therefore, this work focuses on the study of fluidelastic instability in two-phase flow to address the maximum limit of flow rate for a safe operation of such equipment.

This Ph.D. research aims to develop an approach to predict the critical velocity in the U-bend region of a steam generator. Giving the complexity of the flow dynamics in such a region, experimental data were the basis of the development of the design guidelines for steam generators against the fluidelastic instability phenomenon. Such experiments are very expensive and complex to mimic the actual flow and structural conditions occur in steam generators. With the advancements in computational fluid dynamics techniques, the numerical simulation approach

becomes a suitable candidate due its versatility for geometry and flow conditions' customization. Therefore, it is the approach implemented in this work.

The main objectives of this study are:

1. Developing a numerical-based technique to predict the onset of fluidelastic instability for two-phase air-water flows.
2. Investigating the onset of fluidelastic instability for streamwise direction (i.e. direction parallel to the flow).
3. Investigating the effect of the flow's approach angle in tube bundles on the fluidelastic forces and the onset of fluidelastic instability and developing a model to simulate it.
4. Exploring the influence of tubes' frequency detuning on fluidelastic instability mechanisms to refine the prediction of the stability threshold.

1.3. Thesis outline

This thesis is organized in 7 chapters. The first chapter is an introduction to the topic and it outlines the main objectives of this research, as well as the thesis organization. The second chapter contains the literature review. It focuses on the fluidelastic mechanisms, the prediction models, and the modeling of two-phase flows. Chapters (3-6) represents results and validations in the form of four journal papers. Each paper contains an in-depth literature review and a detailed description of the methodology used. The papers are as follow:

- Chapter 3: A journal paper proposes a numerical model based on Computational Fluid Dynamics (CFD) for predicting the critical velocity of fluidelastic instability under two-phase flow conditions. The model is validated for FEI in transverse direction.
- Chapter 4: the validation of proposed numerical model is extended to the streamwise FEI. Moreover, the effect of the spacing between the tubes is also explored.
- Chapter 5: This paper focuses on investigating the relationship between the FEI critical velocity and the flow approach angle. A semi-analytical transformation for the fluidelastic forces is developed and validated.
- Chapter 6: the paper presented in this chapter investigates the influence of frequency detuning on the onset of fluidelastic instability in a novel approach.

It is worth noting that the papers presented in Chapters 3 and 4 contain a comprehensive description of the used FEI predictive numerical models. Finally, the conclusion and the recommendations for future work are presented in Chapter 7.

Chapter 2. Literature Review

Fluidelastic instability is a self-excited phenomenon that involves a movement-induced excitation (Naudascher & Rockwell, 2012). When flow passes through a tube bundle, this instability can cause the tubes to vibrate in any or both of the perpendicular (transverse) and parallel (streamwise) directions relative to the flow. The observation of the fluidelastic instability started in 1960s with Roberts (1966, 1962a). First, he experimentally investigated the self-excited motion of tubes in single and double rows with air flow. The motion of the tubes in his setup was in the streamwise direction with neighboring tubes oscillate out-of-phase. He attributed this motion to the flow jets between the tubes which switch their directions because of the skewed flow channel formed between a tube and its neighbors. This switch causes a change in the size of the wakes downstream the tubes, as seen in Fig. 2.1. Such a change dynamically affects the drag coefficient of each tube. Then, a positive feedback link is sustained between the tubes motion and the jet switching which leads to the self-sustained motion of the tubes in the in-flow direction.

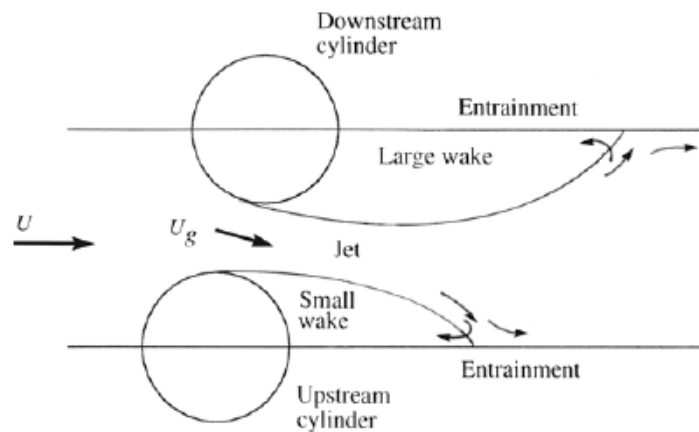


Figure 2.1: Jet switching between tubes and its effect on the size of downstream wakes, (Roberts, 1962)

Following this work, many researches were conducted to reach a better understanding for the underlying mechanisms of the fluidelastic instability. From the analytical point of view, two mechanisms are seen as responsible for the instability, namely, the damping-controlled mechanism and the stiffness-controlled mechanism (Chen, 1983; M. P. Païdoussis, 1983). Both mechanisms exist together and contribute to the onset of fluidelastic instability. The damping-controlled

mechanism is the instability occurs when the total damping acting on the tubes becomes negative. This implies that the damping enhances the response of the tube with time rather than decaying it. Here, the total damping does not refer to only to the classical concept of structural damping which is measured in-vacuum and stagnant flow condition. The flow around the tubes contribute to the total damping by considering terms due to fluid viscosity and the flow velocity itself, as was thoroughly investigated in the literature (Feenstra et al., 2002; Pettigrew & Taylor, 2004; Romberg & Popp, 1999). Therefore, this mechanism exists for the single and multiple degrees of freedom systems. On the contrary, the stiffness-controlled mechanism can only occur for multiple degrees of freedom systems where there are different interactions between the responses of each degree of freedom (a degree of freedom is the independent motion's direction of a tube. A single tube can have two degrees of freedom if it is allowed to vibrate in two orthogonal directions. Therefore, for the tube bank of N flexible tubes, the number of degrees of freedom ranges from N to $2N$). This interaction is represented as a spring between each degree of freedom. Similar to the damping-controlled mechanism, the total stiffness of each spring is a sum of structural and flow-based terms.

2.1. Models of fluidelastic instability

Numerous experimental investigations were conducted and models have been developed to predict the fluidelastic instability for single phase flow. Experimental setups conducting two-phase flows require a higher level of complexity to facilitate the control of the different phases. Following the approach of added flow damping and stiffness, the unsteady model was developed to decompose the unsteady flow forces on oscillating tubes to their added mass, damping, and stiffness parts assuming that the principle of superposition is valid (Chen, 1983; Tanaka & Takahara, 1981). Such decomposition requires a prior knowledge to the flow forces themselves, and thus, they have to be measured experimentally. Although this approach produces an accurate prediction of the onset of instability, it requires extensive measurements for the flow forces on a flexible tube and its neighbors, and a huge data base of these forces that covers a wide range of tube bundle arrangement, spacing-to-diameter ratios, and fluid types. On the other hand, the quasi-static approach was developed by Connors (1970) and Blevins (1974) based on the change of lift and drag coefficients with the change of tubes' static position relative to its equilibrium position. The

model reduces the onset of the instability to a simplified relation known by Connor's equation, as represented in Eq. (2.1):

$$\frac{U_{p,c}}{f_n D} = K \left(\frac{m \delta}{\rho D^2} \right)^{\frac{1}{2}} \quad (2.1)$$

The left-hand side of the equation represents the dimensionless reduced velocity for the flow velocity around the tubes, while the term inside the parentheses in the right-hand side is the dimensionless mass-damping parameter. $U_{p,c}$ is the critical flow velocity at the gap between the tubes, f_n is the natural frequency of the tubes and D is their diameter. m is the mass of tubes per unit length, δ is the damping logarithmic decrement, and ρ is the fluid viscosity. To obtain the constant K , known as Connor's constant, experimental instability data have to be plotted on a log-scale and the value of the constant is found by linear fitting. For the experimental data obtained by Connors for a single row of tubes in air flow, the value of K was 9.9, Fig. 2.2. This equation has been widely used in the industry due its simplicity with different values of the constant K depending on the tube bundle geometrical parameters. However, the model does not provide a deep physical understanding for the fluidelastic instability as it still requires data from the experiments.

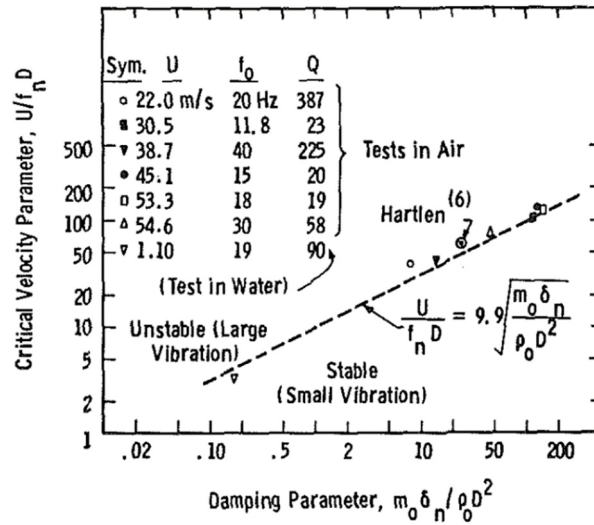


Figure 2.2: Stability diagram for single row array having a pitch-to-diameter ratio of 1.41. (Connors, 1978)

Other stream of model was developed based on the quasi-steady approach where the flow velocity is relatively higher than the tube oscillation velocity. Such approach assumes that the fluid sees

the tubes stationary during its motion. The quasi-steady model produced by Price and Païdoussis (1984) gives a more elaborated stability threshold map than the Connors model. Yet the predicted onset of instability is highly sensitive to a flow retardation parameter μ , Fig. 2.3. Such a parameter was introduced to account for the slowing down of the flow when it approaches a bluff body where the 0 value means no retardation; nevertheless, the model also suffered from the extensive requirement of experimentally measured data for the rate of change of lift and drag coefficients with the displacement and velocity of the moving tubes. However, the needed measured data are less than those needed for the unsteady models.

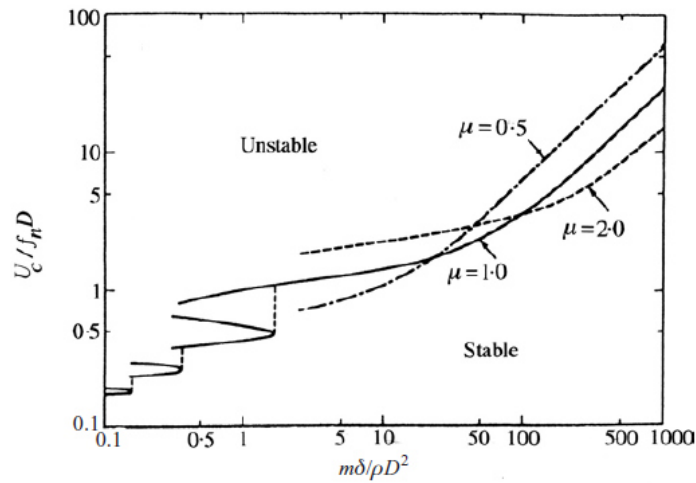


Figure 2.3: Onset of fluidelastic instability for a single flexible tube in a parallel triangular array following the model of Price and Païdoussis (1984).

Another approach for studying the FEI to obtain a semi-analytical model was first pursued by Lever and Weaver for the cross-direction instability of a single flexible tube (Lever & Weaver, 1982) and later modified to for the in-flow instability (Lever & Weaver, 1986), and Yetisir and Weaver for multiple flexible tubes (Yetisir & Weaver, 1993). The analysis assumed a flow cell contains a flexible tube in a tube bundle with two flow channels flows on the two sides of it. The motion of the tube causes a perturbation in the area of the flow channel, which in turn introduces perturbations in the velocity and the pressure fields around the moving tube. However, due to the inertia of the flow, there is a lag between the tube motion and flow perturbations. To evaluate the time lag parameter, they applied the analogy between the case of a tube in cross flow and a flat plat positioned in line with the flow and oscillates in cross direction. They reached a simplified formula for the time lag in a single parameter τ which has to be evaluated experimentally. To relate

the area perturbations to velocity and pressure fields, they used a one-dimensional curvilinear coordinate along the flow channel and the one-dimensional continuity and Navier-Stokes equations were solved analytically.

Despite the deeper physical understanding provided by the semi-analytical model for the parameters affecting the fluidelastic instability, till this day there is no analytical formula for the time lag parameter, which is seen to be a very critical parameter that requires an accurate experimental evaluation for different flow geometries. Yet the main advantage of this model over the unsteady and quasi-steady models is the tremendous reduction in the parameters which is needed to be investigated experimentally.

2.2. Fluidelastic instability in two-phase flow

Less work on the development of theoretical models for the two-phase flow is observed due to the complexity in modeling the interaction between the two phases with each other hence their interaction with the structure. The effect of the two-phase flow on fluidelastic instability has been investigated by many researchers (Feenstra et al., 2000; Nakamura et al., 1995; Pettigrew & Taylor, 1994) and they showed the effect complicates the theoretical models. Therefore, most of the research effort was dedicated to direct experimental investigation of the onset of the fluidelastic instability.

In steam generators the two-phase flow is a steam-water mixture; however, in a laboratory scale experiment, it is practically difficult to control the flow parameters in the loop to simulate the real working conditions at elevated pressure and temperature conditions. Therefore, scarce published work used steam-water flow (Axisa et al., 1985; Hirota et al., 2002). On the other hand, numerous investigations utilized air-water mixtures due to its easiness in operation and cost effectiveness (Inada et al., 1996; Janzen et al., 2005; Mitra et al., 2009; Pettigrew, Tromp, et al., 1989). The results obtained in these works gave a general overview for the characteristic features of the fluidelastic instability in two-phase flows, mainly the dependency on the two-phase flow regimes (bubbly, intermittent, and mist flows). Despite the advantages of air-water mixture, a distinctive deviation in the threshold of the instability's onset is observed relative to the steam-water mixture. This is attributed to the difference in the density ratio between the phases. In air-water mixture this ratio is 830, while for steam-water mixture experiments it is around 33 (Axisa et al., 1985;

Pettigrew, Tromp, et al., 1989). This difference affects the slip between the two-phases (Feenstra et al., 2000) and therefore alters the dynamic forces on the vibrating tubes. As a compromise, other researchers used refrigerants as a two-phase flow (Feenstra et al., 2002; Pettigrew et al., 1995) since its density ratio is closer to steam-water mixture.

In an attempt to obtain a fluidelastic instability's predictive model in two-phase flows, Carlucci (1980) and Pettigrew and Taylor (2004) worked on casting the two-phase flow effect into the Connor's equation by introducing an additional term that represents the two-phase flow damping. They analyzed data for different flow geometries to account for the change of the damping parameter with the void fraction. The data suffered from scattering, therefore the authors proposed a conservative guideline values for the damping. Recently, Moran and Weaver (2013) did elaborative assessment of techniques used to measure the two-phase damping component. They showed that the exponential curve fitting technique provides more consistent values than the widely used half power bandwidth method.

On the other hand, for the unsteady force measurements Inada et al. (1996) evaluated experimentally the unsteady forces parameters in an air-water flow. Their measurements suffered from scattering compared to those obtained by Tanaka and Takahara (1981) for a single phase water flow. The same observation of scattering data is found for the measurements of Hirota et al. (2002) for steam-water mixture. However, recent measurements for the unsteady fluid forces were done for air-water mixture which showed less scattering (Olala & Mureithi, 2015; Sawadogo & Mureithi, 2014).

2.3. Uncertainties in Fluidelastic instability measurements

Scattering of measured direct onset of FEI is observed in single phase flows data. Weaver and Fitzpatrick (1988) have collected such data for the four standard tube array's configurations: normal triangle, parallel (rotated) triangle, normal square, and rotated square. Scattering is observed in each configuration with a deviation from the mean around $\pm 25\%$ for the normal square up to $\pm 50\%$ for the parallel triangular configuration. Therefore, design guidelines are established on a very conservative basis to avoid FEI. Moreover, the direct measurements of fluidelastic forces and the extracted flow added parameters also suffer from scattering, though with a less extent. For instance, the measurements obtained by Tanaka and Takahara (1981) for the normal square

configuration showed scattering at reduced flow velocity higher than 10. This scattering was more noticeable in the phase angle data for the fixed tubes surrounding the oscillating one with a deviation up to $\pm 15^\circ$. Furthermore for two-phase air-water mixture flow, the extracted flow added parameters done by Inada et al. (2002) showed very high scattering. Such uncertainty in the measurements has a significant impact in the accuracy of the obtained threshold of stability obtained by the various FEI models.

2.4. Fluidelastic instability in U-bend region

The construction of a typical steam generator used in the CANDU power generation plant is shown in Fig. 2.4. The water from the power generation loop flows on the shell side around the tube bundle. It enters from the inlet port at the bottom of the steam generator, distributes circumferentially, and flows upward. When it arrives at the U-bend section, a part of it has already boiled and transformed into steam causing the overall density to drop and the flow field to accelerate as shown by Mohany et al. (2012) for the velocity distribution presented in Fig. 2.5. At the U-bend region, the flow velocity is the highest and reaches higher than 5 m/s in an angle close to the normal of tubes' centerlines. Provided that the span between the supports is larger at this section, this makes the U-bend section most vulnerable to the occurrence of fluidelastic instability (Mohany et al., 2009).

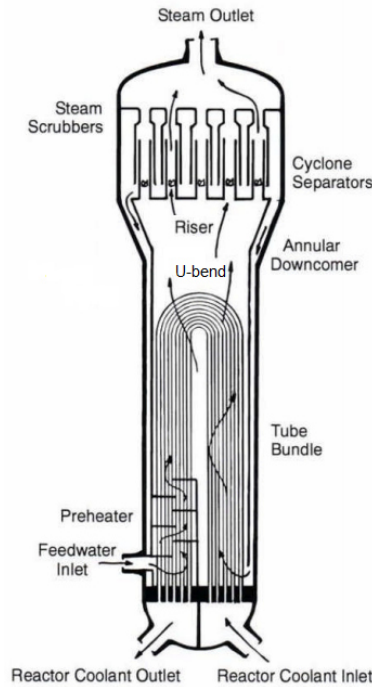


Figure 2.4: Steam generator for the CANDU system (Garland, 2014).

Three vibrational aspects are noted in the U-bend. First, the fluidelastic instability generally occurs in both transverse (perpendicular to tube axis and flow) and in-flow directions (parallel to the flow). Many experimental investigations observed that the instability is dominant in the transverse direction with no change of tubes vibrational response in the in-flow direction, for example see (Feenstra et al., 1995; Hirota et al., 2002; Pettigrew, Taylor, et al., 1989). This leads to focusing on restricting the tubes from oscillating in the transverse direction using flat bars or Anti-Vibration Bars (AVB) placed between the tubes. Weaver and Schnider (Weaver & Schneider, 1983) studied the effect of these bars on prohibiting the occurrence of transverse fluidelastic instability. They concluded that the AVB with small clearances do not only enhance the stability of the tube bundle in transverse direction but also strengthened it in the in-flow direction with no instability observed for a critical velocity three times larger than its counterpart without AVB. However, in a recent incident in 2012, unexpected tube-to-tube and tube-to-AVB high wear amount were observed in the steam generators 2 and 3 of the San Onofre Nuclear Generating Station (SONGS). An incident was discovered by observing higher than normal radioactive leakage and contamination in condenser, and lead to the shutdown and closure of the station in 2013. It was found that in-flow fluidelastic instability was the main root of the problem which was not considered in the design

guidelines at that time. This brought more attention to the study of the in-flow fluidelastic instability.

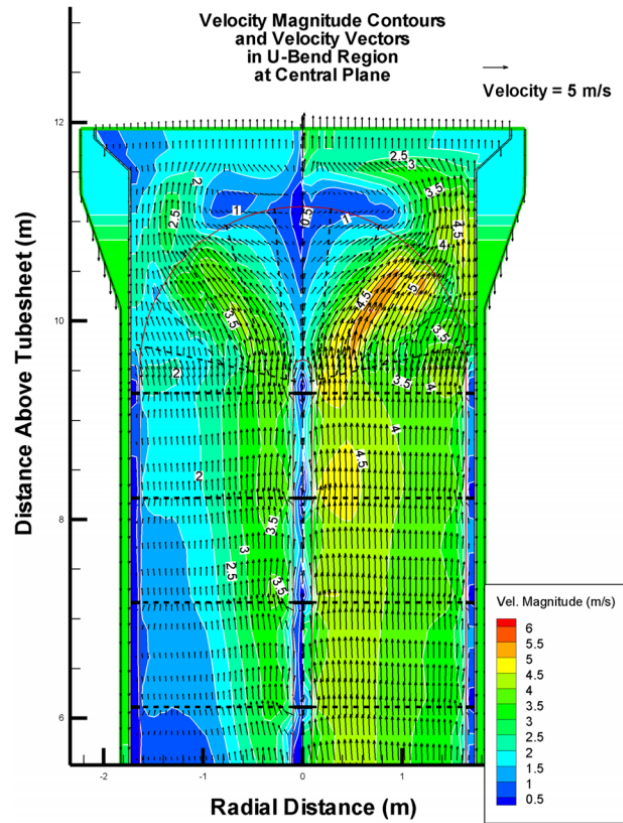


Figure 2.5: Simulated velocity field distribution at the central plane in a typical CANDU steam generator working at 100% load (Mohany et al., 2012).

The second aspect for the U-bend is the flow approach angle. As seen from Fig. 2.5, the flow velocity is not perfectly perpendicular to the tubes at the U-bend, but it approaches the tubes with an angle that varies from a location to another. Such “oblique” flow is not limited in the U-bend plane but also in a plane passes perpendicularly through the tube bundle. (Weaver & Yeung, 1983; Yeung & Weaver, 1983) studied this effect for triangular and square tube bundle arrangement in water tunnel for a kernel of flexible tubes in a rigid tube bundle. They found a contradicting behaviour between the two tube patterns regarding the fluidelastic instability. The square pattern was insensitive to the approach angle, while for triangular arrays it showed very high sensitivity. Most recently, Elhelaly et al. (2020) investigated the approach angle effect for both square and triangular arrays in a wind tunnel. The study was for a single flexible tube in a

rigid array. However, he found that the square array exhibits a dependence on the flow approach angle for the fluidelastic stability threshold.

Thirdly, at the U-bend region inner tubes have shorter arc length than the outer tubes. This makes the inner tubes stiffer than the outer ones, and consequently the natural frequency of the tubes is not uniform or detuned in that region. Rare research work was dedicated for the study of the tubes detuning on fluidelastic instability. Olala and Mureithi (2016) analyzed a kernel bundle of 7 tubes using the quasi-steady model and showed that the in-flow fluidelastic instability is very sensitive to detuning. Their analysis relied on assigning a sample of statistically random values of natural frequencies to the flexible tubes to mimic the detuning effect. While all samples had the same mean frequency value, their variance was different and it was employed as an index for the amount of detuning. Although this approach is well representing to their analysis, it only provides a clear insight to the mean effect of the detuning as the distribution of natural frequencies is randomly distributed among the flexible tubes. This is not the case in the U-bend zone as the tubes' stiffness is varying with a certain pattern; inner tubes are stiffer than outer tubes. As shown in Fig. 2.6 where the Connors constant is plotted versus the tube frequency variance, there is a scattering in the analysis data indicating that also the way of the distribution of the natural frequencies values plays a rule and not only the amount of detuning. On the other hand, the general or the mean trend represented by the linear curve fitting of the data indicates that increasing the detuning amount generally leads to a more stable bundle. This agrees with an analytical analysis provided by Païdoussis et al. (2010) for the coupled two-degrees of freedom motion stiffness controlled instability that the detuning has a stabilizing effect.

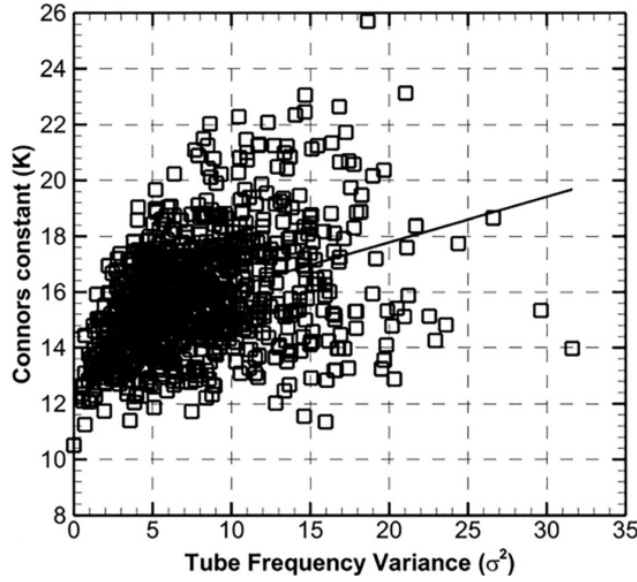


Figure 2.6: Effect of frequency detuning on streamwise stability constant (Olala & Mureithi, 2016).

2.5. Numerical techniques

With the recent rapid development in computer architecture and the computations speed, numerical approaches utilizing Computational Fluid Dynamics (CFD) models become more attractive as a tool for the analysis of engineering designs. In simulating the fluidelastic instability, sparse investigations were performed in directly predicting the stability threshold even for single-phase flows. In such approach the tubes in the computational domain are allowed to move freely according to the forces acting on their surfaces due to the fluid flow. A major problem faces such approach is the high mesh deformation due to the excessive tube's vibration when it encounters the FEI which leads to convergence problems during the simulations. Trying to produce the longest possible simulated time signal, the available studies in the literature usually configure a single tube to be flexible within a rigid tube array. This limits the FEI to occur only due to the damping mechanism in the transverse direction. For example, Shinde et al. (2015) assessed the direct approach against experimental measurements using the large eddy simulation (LES) model in terms of the power spectral density and oscillation frequency for a single flexible tube in a tube bundle. The experiments were performed for water flow and their simulation results were very comparable to the experimental ones. However, their simulations suffered from high demand for computational power and were limited to low normalized reduced velocity at such fluidelastic

instability is controlled by the damping mechanism. Later, de Pedro et al. (2016) relaxed the use of LES model and switched to the Reynolds Average Navier-Stokes $k - \epsilon$ model for air flow simulation across a closely packed tube bundle which facilitated simulating high reduced velocities without a high demand of computational power compared to the LES model. For their studied cases, the numerical results were closely matching the experimental counterpart. Nevertheless, their simulations were still limited to a single flexible tube controlled by the damping mechanism. Alternatively, CFD is more attractive to be used to extract the theoretical model parameters. The extracted parameters are then integrated in the theoretical models and the instability can be predicted efficiently and accurately. In this method, a prescribed harmonic motion with certain amplitude is specified for a tube. This amplitude is small such that the mesh cells do not suffer of high deformation and skewness, thus better convergence and accuracy. Employing this method for single-phase flows, Hassan et al. (2010) extracted the unsteady fluidelastic force parameters for parallel square and triangle tube arrays. The parameters were then integrated in the unsteady flow model and the effect of the Reynolds number and array pitch were investigated. Recently, Elbanhawey et al. (2020) have utilized a similar approach to simulate the tube dynamic response induced by the coolant flow inside a nuclear fuel bundle. Khalifa et al. (2013) and El Bouzidi et al. (2014) employed the same approach to extract the time lag parameter used in the semi-analytical model of Lever and Weaver for the parallel triangle arrays. These attempts showed good agreements with comparable experimental data.

Along with the complexity encountered in the simulation of fluidelastic instability in the single-phase flows, adding another phase will introduce a further difficulty to capture the interaction between the phases themselves in one hand and with the structure on the other hand. As concluded from the experimental investigations done on two-phase flows, the flow regime plays a major rule in defining the fluidelastic instability threshold. A trial was made by Tixier et al. (2015) to predict the onset of fluidelastic instability in a two-phase flow using the porous medium approach. However, their approach was limited to low void fractions and highly over predicted the onset of instability. Another effort was pursued by Selima et al. (2021) by developing a lagrangian-based model. The model was tuned for the bubbly flow and was designed to track the forces and interaction of each bubble with its surroundings. Thus, bubble coalescence, bouncing, and break up were all simulated in the time-domain, and instantaneous prediction of the local air void fraction and flow forces were achieved. Although, the model was based on few simplifications for the

continuous (water) phase, it showed very promising results for the prediction of the onset of fluidelastic instability.

2.6. Summary

From the previous review, it can be concluded that most of the progress achieved to understand the mechanisms behind fluidelastic instability is based on single phase flow although the vast majority of equipment used in the industry deal with two-phase flows. The already developed models in single-phase flows give a good insight to the mechanisms controlling the FEI. Nevertheless, they still rely on experimental measurements for their closure which correspond to the geometry of each tube bundle. For two-phase flows, it is proven from the experiments that the void fraction and the flow regime are important parameters to be considered. Despite the work done to incorporate them into the existing models, scattering in the calculated two-phase related correction parameters is observed. Therefore, designing practices in the industry are still relying on experimental data for providing either the required model parameters or the instability threshold directly for every array geometry and flow condition, especially for the case of two-phase flows encountered in steam generators to provide conservative design guidelines.

Moreover, in steam generators the most prone part of the tube bundle to fluidelastic instability is the U-bend region. The geometrical shape of this region enforces two aspects. First, the flow direction is not perfectly perpendicular to the tube bundle but it approaches with an angle of inclination (*approach angle*). Second, the variation of the span lengths between the inner and outer tubes in the bend enforces a variation in the tubes' stiffness. This is translated as a different vibrational natural frequency of each tube or *frequency detuning*. The flow approach angle has not been thoroughly investigated for two-phase flows. The effect of tubes detuning is only studied for a randomly distributed natural frequencies for a flexible tube kernel. The results from the analysis indicate that the distribution pattern of detuning also has a significant effect, which requires further investigation.

Replicating the same flow conditions which take place in a steam generator to laboratory scale experiments is typically laborious and expensive. In real conditions of steam generators, the flow is typically a steam-water mixture at elevated pressure and temperature. This makes the necessary detailed measurements of the flow parameters in the tube bundle vicinity very challenging.

Therefore, laboratory scale experiments often idealize these flow conditions and replace them by air-water mixture and atmospheric pressure and temperature. Therefore, providing a general method by which such detailed measurements become feasible is crucial for better understanding of the FEI phenomenon.

Chapter 3. Numerical investigation of the cross flow fluidelastic forces of two-phase flow in tube bundle

Complete citation

Sadek, O., Mohany, A., & Hassan, M. (2018). Numerical investigation of the cross flow fluidelastic forces of two-phase flow in tube bundle. *Journal of Fluids and Structures*, 79, 171-186. <https://doi.org/10.1016/j.jfluidstructs.2017.11.009>

Copyright

Published in accordance with the Journal of Fluids and Structures' copyright agreement (Appendix A).

Author's contribution

O. Sadek: Conceptualization, Methodology, Software, Data curation, Writing- Original draft preparation.

A. Mohany: Supervision, Methodology, Writing- Reviewing and Editing, Resources, Funding acquisition.

M. Hassan: Supervision, Methodology, Writing- Reviewing and Editing, Visualization.

Abstract

This paper presents a numerical model to predict the unsteady fluid forces in a parallel triangular array subjected to two-phase flow. The numerical model utilizes the RANS formulation with aid of Spalart-Allmaras turbulence model, while the physics of the two-phase flow are modeled by the mixture model, drift-flux model, and the interfacial area concentration concept. This numerical model was utilized to simulate an air-water flow in tube array with various air void fractions. The predicted fluid force coefficients were compared with the available experimental data. The comparison showed a good agreement in terms of the force magnitude and phase at various reduced flow velocities. The obtained force coefficients were employed in a Hybrid analytical-

CFD model representing a kernel of 7 tubes. The stability was investigated by studying the eigen values of the system as a function of the flow velocity. In addition, the stability thresholds were examined by simulating the same 7 flexible tubes kernel in cross flow using the direct flow/structure coupling. The predicted stability threshold obtained via these two models agrees very well with the experimental counterparts. They represent a lower bound for the stability data. These results are very promising and represent an important step towards an analytical frame work to accurately predict the stability of tube arrays.

Keywords

Fluidelastic Instability, Flow-Induced Vibration, Flow-Structure Coupling, Two-Phase Flow, Numerical Simulations, Tube Bundles

3.1. Introduction

Fluidelastic instability (FEI) is the most important excitation mechanism the can cause severe flow-induced vibration in tube bundles. This mechanism is characterized by a threshold (critical flow velocity) beyond which very large oscillations take place. This form of instability can lead to excessive fatigue stresses, tubes collision, and fretting wear at the supports. Heat exchangers and steam generators are typical industrial devices that are prone to the occurrence of the fluidelastic instability. Such occurrences often lead to tube failure in a very short period of time. Due to the devastating nature of the FEI large number of efforts was directed towards understanding the FEI mechanism. These efforts have resulted in a number of guidelines and theoretical models. These empirical and theoretical models were developed to obtain a reliable estimation for the onset of the instability. The theoretical models can be categorized into four main streams: the quasi-static models of Connor and Blevins (Blevins, 1977; Connors, 1970), the coefficients-based unsteady models (Chen, 1983; Tanaka and Takahara, 1981), the quasi-steady models (Price & Païdoussis, 1983, 1984), and the semi-analytical models of Weaver et al. (Lever and Weaver, 1982; Yetisir and Weaver, 1993). Out of these efforts, the Connor's equation which is based on the quasi-static approach is widely used in the industry because of its simplicity. Industrial guidelines are based on fitting the Connor's equation constants to the experimental data. The semi-analytical model by

Leaver and Weaver (1982) was derived from the first principal of structural and fluid mechanics and does not require many experimentally measured coefficients. Subsequent developments of the model include provisions to handle nonlinearities due to the loose supports (Hassan & Hayder, 2008) and simulating U-bend tube bundle vibrations (Hassan & Mohany, 2012). The unsteady models relate the destabilizing fluid forces to the tube bundle response through a number of fluid force coefficients. This requires the knowledge of these coefficients over a wide range of reduced flow velocities. This approach could be very effective if these experimental data are generated. Direct experimental measurements of the flow forces acting on an oscillating tube were used to obtain these coefficients. The applicability of this approach is limited to only those tube arrays with existing measured force data. This is considered to be the major drawback of this approach.

Due to the complexity of the two-phase flow-induced vibrations, the majority of the investigations were directed towards experimental studies. Experimental investigations utilized steam-water (Axisa et al., 1985; Mitra et al., 2009; Nakamura et al., 1995), refrigerants (Feenstra et al., 2000), or air-water mixture (Pettigrew, Tromp, et al., 1989). While the experiments using the steam-water mixtures closely resemble the actual steam generators such experiments are very expensive and difficult to perform. Experiments using refrigerants such as Fereon-11 are easier to perform. It is argued that the density ratio of the two phases will affect the difference in flow velocity between the phases. Additional factors such as the liquid surface tension, plays an important role in controlling the bubble size. As such, the use of refrigerants represents a practical alternative where the density ratio and surface tension are closer to those of the steam-water mixture than air-water (Mohany et al., 2012). However, the majority of the two-phase flow experiments were performed via air-water mixture at isothermal and atmospheric conditions. This is because air-water mixture experiments are much easier to perform and the data obtained from these experiments are reasonably accurate. These studies provided an understanding of the phenomenon and the factors affecting the stability. For example using the air-water mixture, (Pettigrew et al., 2001) studied the effect of tube array geometry on the onset of instability. They concluded that for all geometries two distinctive zones of fluidelastic instability are present according to the flow regime and hence the air void fraction. They also reported that the total damping ratio is dominated by the air void fraction.

The development of all of the theoretical models focused on the single-phase flow. Much less efforts were directed at investigating the two-phase flow experimentally. This is due to the complexity in modeling the interaction among the phases and with the structure. In addition, the phenomenon depends on many factors such as array geometry and the flow conditions including void fraction, velocity, and density. Not surprisingly, attempts to devise a guideline relied on modifying the simple familiar Connors equation. For example, Pettigrew and Taylor (2004) accounted for the effect of the two-phase flow in the Connor's equation by introducing a variation in the damping parameter as a function of air void fraction. In an attempt to cast the two-phase fluidelastic instability on the framework of the unsteady flow theory, Inada et al. (1996) evaluated experimentally the unsteady force parameters in an air-water flow. However, their measurements suffered from scattering compared to those obtained for a single-phase water flow. Recent measurements for the unsteady fluid forces were presented by Sawadogo and Mureithi (2014) and Olala and Mureithi (2015) for air-water mixture represented a much more correlated data with less scattering behavior.

Computational Fluid Dynamics (CFD) can be utilized to extract the theoretical model parameters. The extracted parameters are then integrated in the theoretical models and the instability can be predicted efficiently and accurately. Utilizing this method, Hassan et al. (2010) extracted the unsteady fluidelastic force parameters for in-line square and rotated triangle arrays. The parameters were then integrated in the unsteady flow model and the effect of the Reynolds number and array pitch were investigated. Recently El Bouzidi et al. (2014) employed the same approach to extract the time lag parameter used in the semi-analytical model of Lever and Weaver for the rotated triangle arrays. These attempts showed good agreements with comparable experimental data. Alternatively, direct numerical Flow/Structure coupled CFD models enjoyed much less success in directly predicting the stability threshold even in single-phase flows. In such approach the tubes in the computational domain are allowed to move freely according to the forces acting on their surfaces due to the fluid flow. Other examples that successfully utilized the CFD approach in simulating flow in tube-bundles include (Anderson et al., 2014; de Pedro et al., 2016; Shinde et al., 2014).

The modeling of multiphase flows has also been developed through time. Though, few approaches are popularly implemented in CFD codes, namely, the Volume of Fluid modelling, the Multifield Eulerian modelling, the mixture model, and the Lagrangian particle tracking approach. The Volume of Fluid modelling aims to resolve the interface between multiple phases at every instant of time which requires meshing elements fine enough to capture the interface accurately. Thus, it is superior in the modelling of stratified and slug flows. On the other hand, the Multifield Eulerian modelling relaxes this requirement and solves the governing equations for each phase field while the interphase coupling is achieved through several sub-models depending on the nature of the phases. This approach is often used to model fluidized beds, and bubble and droplet flows. Alternatively, the mixture model reduces the need for solving the governing equations for each phase. Instead, it solves equations for a continuum represents the mixture of all phases. However, a transport equation for the void fraction of every secondary phase is solved. As such, the interphase coupling is modeled by the slip velocities between each secondary phase and the continuous phase. Therefore, this model requires less computational power than the Multifield Eulerian modelling. The Lagrangian particle tracking approach focuses on tracing the forces and the motion of each secondary phase particle. This demands high computational power in the case of high particle numbers. Thus, it is often used for atomization and spray applications.

In this work, a two-phase flow numerical model based on the mixture model is proposed to predict the fluidelastic unsteady force coefficients and phases acting on an oscillating tube in two-phase air-water flow in parallel triangular tube array. The results are compared with the experimental data obtained by Sawadogo and Mureithi (2014) for tube oscillations in the lift direction. Such knowledge of these forces acting on the oscillating tube and its neighbors facilitates the prediction of the onset of fluidelastic instability for different void fractions.

3.2. Modeling and governing equations

The RANS form of flow governing equations is used with selecting the Spalart-Allmaras turbulence model. It is a one-equation model developed specifically for bounded flow against adverse pressure gradient. The model was implemented previously by Mohany et al. (2014) to model the flow structure around side-by-side tubes and obtained an excellent comparison with the PIV that was done for the same case. In the current work, the model is casted into the formulation

of a two-phase flow. This casting treats the flow parameters as average values of the mixture of the phases, and these averages depend on the proportions of the phases within each finite volume (i.e. volume fractions) in the domain. Thus, the continuity equation for the mixture is formulated as:

$$\frac{\partial}{\partial t}(\rho_m) + \nabla \cdot (\rho_m \mathbf{u}_m) = 0 \quad (3.1)$$

The mixture density ρ_m and the mixture velocity vector \mathbf{u}_m of a finite volume are obtained from the volume fraction a_k , the density ρ_k , and the velocity vector \mathbf{u}_k of each phase k as:

$$\rho_m = \sum_{k=1}^n a_k \rho_k \quad (3.2)$$

$$\overline{\mathbf{u}_m} = \frac{\sum_{k=1}^n a_k \rho_k \mathbf{u}_k}{\rho_m} \quad (3.3)$$

Also, the instantaneous momentum equation for the mixture is obtained from summing the momentum equation for each phase and it reads:

$$\begin{aligned} & \frac{\partial}{\partial t}(\rho_m \mathbf{u}_m) + \nabla \cdot (\rho_m \mathbf{u}_m \mathbf{u}_m) \\ &= \rho_m \vec{g} - \nabla P + \nabla \cdot (\mu_m (\nabla \mathbf{u}_m + \nabla \mathbf{u}_m^T)) + \nabla \cdot \left(\sum_{k=1}^n a_k \rho_k \mathbf{u}_{dr,k} \mathbf{u}_{dr,k} \right) \end{aligned} \quad (3.4)$$

where $\vec{\mathbf{u}}_{dr,k}$ is the drift velocity vector of the phase k relative to the mixture velocity \mathbf{u}_m and is calculated as:

$$\mathbf{u}_{dr,k} = \mathbf{u}_k - \mathbf{u}_m \quad (3.5)$$

The velocities of the phases are related to each other by the slip velocity which is estimated by the algebraic formulation of the drift-flux model. The formulation of the drift-flux model assumes a local force equilibrium between the phases, which requires the knowledge of the phases' particle size.

The ensemble-averaging of the Eq. (3.4) of the mixture leads to the rising of the sub-grid scale Reynolds stress term (\mathbb{T}_{ij}) for the mixture which is modeled by the Spalart-Allmaras turbulence

model (Spalart & Allmaras, 1992). The model is based on solving a single transport equation for the modified kinematic eddy viscosity $\tilde{\nu}_m$. This equation, in the form of the mixture properties, is:

$$\begin{aligned} \frac{\partial}{\partial t}(\rho_m \tilde{\nu}_m) + \nabla \cdot (\rho_m \tilde{\nu}_m \mathbf{u}_m) \\ = \frac{1}{\tilde{\sigma}_v} [\nabla \cdot ((\mu_m + \rho_m) \nabla \tilde{\nu}_m) + C_{b2} \rho_m (\nabla \tilde{\nu}_m)^2] + (G_v - Y_v) \end{aligned} \quad (3.6)$$

The turbulent eddy viscosity μ_t is estimated as

$$\mu_t = \rho_m \tilde{\nu}_m \frac{\left(\frac{\tilde{\nu}_m}{\nu_m}\right)^3}{\left(\frac{\tilde{\nu}_m}{\nu_m}\right)^3 + C_{v1}^3} \quad (3.7)$$

Here, the variables G_v , Y_v , ν_m and μ_m are the turbulence generation, the destruction, the kinematic and the dynamic viscosities of the mixture, respectively. On the other hand, $\tilde{\sigma}_v$, C_{b2} and C_{v1} are the model constants. The turbulent eddy viscosity μ_t is then employed to estimate the Reynolds stresses \mathbb{T}_{ij} using the Boussinesq hypothesis.

$$-\mathbb{T}_{ij} = \mu_t (\nabla \mathbf{u}_m + \nabla \mathbf{u}_m^T) \quad (3.8)$$

The distribution of the volume fraction for the secondary, or dispersed phases p , in the primary, or continuous phase q , is governed through the continuity equation of each phase. In this work, the air bubbles are considered as the dispersed phase in the continuous liquid water phase:

$$\frac{\partial}{\partial t}(a_p \rho_p) + \nabla \cdot (a_p \rho_p \mathbf{u}_m) = \sum_{q=1}^n (\dot{m}_{qp} - \dot{m}_{pq}) - \nabla \cdot \left(\sum_{p=1}^n a_p \rho_p \mathbf{u}_{dr,p} \right) \quad (3.9)$$

The first term in the RHS represents the mass transfer between the phases due to the phase change, which is neglected in the current simulations, while the second term accommodates for the drift between the dispersed phase and mixture velocities.

To close the system of equations governing the problem, the bubble size in the domain is estimated through introducing the interfacial area concentration parameter χ , which represents the total surface area of the dispersed air bubbles per unit volume of the mixture. The Sauter-mean diameter of the bubbles d_{32} is related to the interfacial area concentration as:

$$d_{32} = \frac{6 a_p}{\chi} \quad (3.10)$$

while the distribution of the bubble size in the domain is predicted by solving the transport equation for the interfacial area concentration Eq. 3.11. The right-hand side of this equation takes into account the effects of compressibility of the bubbles and the mass transfer between the phases (both neglected in the current work). The terms S_{RC} , S_{WE} , and S_{TE} represent the bubbles coalescence due to random collision and wake entrainment, and the bubbles breakup due to turbulent eddies, respectively. The model provided by Wu et al. (1998) is used to estimate these terms.

$$\frac{\partial}{\partial t}(\chi \rho_p) + \nabla \cdot (\chi \rho_p \overline{u_p}) = \frac{1}{3} \frac{D\rho_p}{Dt} \chi + \frac{2}{3} \frac{\dot{m}_{qp}}{a_p} + \rho_p (S_{RC} + S_{WE} + S_{TE}) \quad (3.11)$$

The SIMPLE (Semi-Implicit Method for Pressure Linked Equations) algorithm is used to solve the pressure and velocity fields of the flow. The spatial discretization of the domain was done by using the first order upwind scheme. On the other hand, the implicit first order formulation was utilized as a time marching scheme. Such formulation guarantees that the convergence of the solution. Typically, 40 iterations per time step were found to be sufficient to insure accurate calculation of the flow and pressure fields in the domain.

3.3. Unsteady fluid/structure interaction modeling

A coupling between the flow forces and the structural vibration of the tubes is necessary for the prediction of the onset of fluidelastic instability. This is done by two different methods: the hybrid analytical-CFD model (Hassan et al., 2010) and the direct Flow/Structure simulation.

3.3.1. Hybrid Analytical-CFD Model

The general form of the equations that govern this coupling for N flexible tubes can be represented as:

$$[M_s][\ddot{x}_i] + [C_s][\dot{x}_i] + [K_s][x_i] = [F_f] \quad (3.12)$$

The right-hand side of the equation represents the unsteady fluid forces acting on the flexible tubes, while $[M_s]$, $[C_s]$, $[K_s]$, and $[x_i]$ are the structural mass, damping, stiffness, and tubes motion matrices, respectively. The unsteady flow forces acting on a particular tube are dependent not only

on the motion of this tube but also on the motion of the surrounding tubes. Thus, the magnitude of the drag (F_x) and lift (F_y) forces acting on tube i can be expressed as (Chen, 1987):

$$F_{x,i} = -\frac{\pi D^2}{4} \sum_{j=1}^N (\alpha_{ij} \ddot{x}_j + \sigma_{ij} \ddot{y}_j) + \frac{\rho_m U^2}{\omega} \sum_{j=1}^N (\alpha'_{ij} \dot{x}_j + \sigma'_{ij} \dot{y}_j) + \rho_m U^2 \sum_{j=1}^N (\alpha''_{ij} x_j + \sigma''_{ij} y_j) \quad (3.13-a)$$

$$F_{y,i} = -\frac{\pi D^2}{4} \sum_{j=1}^N (\tau_{ij} \ddot{x}_j + \beta_{ij} \ddot{y}_j) + \frac{\rho_m U^2}{\omega} \sum_{j=1}^N (\tau'_{ij} \dot{x}_j + \beta'_{ij} \dot{y}_j) + \rho_m U^2 \sum_{j=1}^N (\tau''_{ij} x_j + \beta''_{ij} y_j) \quad (3.13-b)$$

where α_{ij} , σ_{ij} , τ_{ij} , and β_{ij} are the added-mass coefficients, α'_{ij} , σ'_{ij} , τ'_{ij} , and β'_{ij} are the fluid damping coefficients, α''_{ij} , σ''_{ij} , τ''_{ij} , and β''_{ij} are the fluid stiffness coefficients, while ω is the angular frequency of tube oscillation, and U is the gap velocity which can be calculated from the free stream velocity (U_∞) as:

$$U = \frac{P}{P - D} U_\infty \quad (3.14)$$

When the flow forces are moved to the left-hand side in Eq (3.12) as forms of contribution to the mass, damping, and stiffness matrices, the general form of the coupling equations is transformed into:

$$[M_s + M_f(U_r)][\ddot{x}_i] + [C_s + C_f(U_r)][\dot{x}_i] + [K_s + K_f(U_r)][x_i] = 0 \quad (3.15)$$

The new parameters $[M_f(U_r)]$, $[C_f(U_r)]$, and $[K_f(U_r)]$ represent the added flow mass, damping, and stiffness matrices, respectively. These parameters are functions of the dimensionless reduced velocity ($U_r = 2\pi U/\omega D$). They also require the knowledge of the fluid force coefficients (α_{ij} , σ_{ij} , τ_{ij} , β_{ij} , α'_{ij} , σ'_{ij} , τ'_{ij} , β'_{ij} , α''_{ij} , σ''_{ij} , τ''_{ij} , and β''_{ij}).

3.3.2. Direct Flow/Structure Coupling

The solid tubes in this type of simulation are treated as rigid body and no surface deformation are permitted. Some of the tubes are allowed to oscillate freely (i.e. flexible tubes) in the x-direction according to the acting forces on them. Therefore, each flexible tube can be seen as a single degree of freedom damped oscillator subjected to the unsteady fluid force, as shown in Fig. 3.1. Here, $k_{s,i}$ and $C_{s,i}$ are the structural stiffness and damping parameters of the i^{th} flexible tube. The coupling between the flow and structure fields is established through the exchange of transient flow force F_f and tube deflection between the fluid and structural solvers. The force calculated by the fluid solver is communicated to the structural solver and used to calculate the tube response. The resulting tube response is communicated to the fluid solver and used to induce the fluid mesh deformation. This process is repeated each time step.

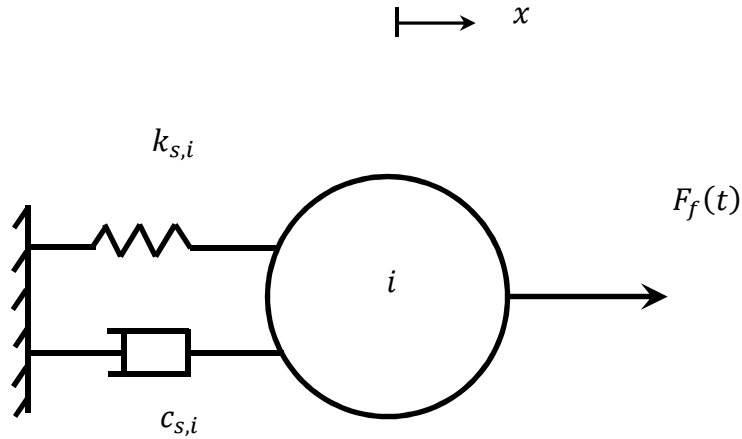


Figure 3.1: Single degree of freedom simple harmonic damped oscillator under unsteady external force.

3.4. Flow Domain Simulation

A 2-D flow domain is used to represent a parallel triangular tube array as shown in Fig. 3.2. The array consists of 13 rows and 3 columns of tubes and an addition two columns of half-tubes placed at the walls. The pitch-to-diameter ratio (P/D) and tube diameters are 1.5 and 38 mm, respectively. The upstream and downstream lengths are 5.5D.

A simulation run is set by specifying the values of the free upstream velocity at the inlet. This allows for controlling the gap reduced velocity. Moreover, the Sauter-mean bubble size diameter is also specified in the slip velocity calculation between the different phases. Then, the simulation

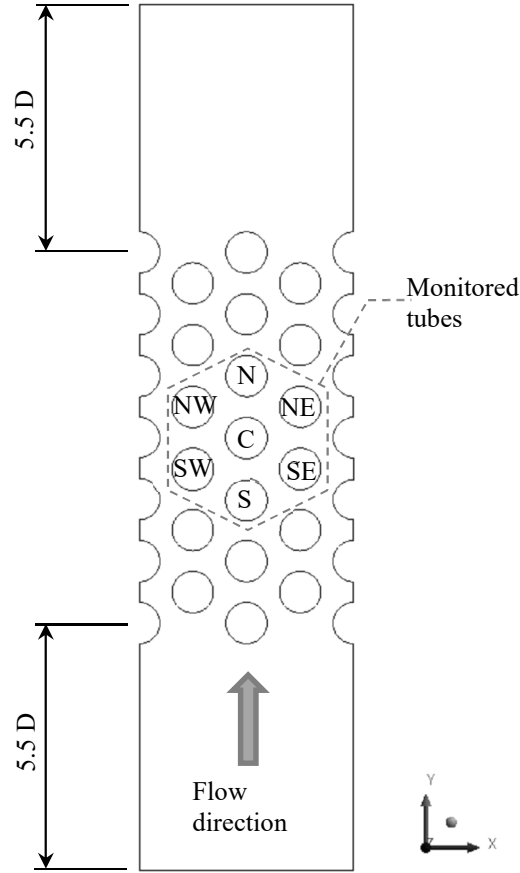


Figure 3.2: 2-D flow domain for a parallel triangular tube array.

is carried on two stages; first a quasi-steady-state solution is obtained while all tubes are kept static. This will provide the initial condition for the second stage of unsteady simulation. For the purpose of calculating the fluid-force coefficients, periodic oscillations of a frequency of 8 Hz was imposed on the central tube (C) in the lift (x-direction). This value is identical to what was used in the experimental work of Sawadogo and Mureithi (2014). As such, direct comparison with their results can be carried out. The mesh cells around the oscillating tube are allowed to deform according to the new position of the tube at each time step, and this is done by redistributing the mesh nodes and smoothing their locations according to the Laplacian diffusion equation:

$$\nabla \cdot (\Gamma \nabla \mathbf{w}) = 0 \quad (3.16)$$

where \mathbf{w} is the mesh's node velocity vector and Γ is a diffusion parameter.

The Arbitrary-Lagrangian-Eulerian (ALE) formulation for the flow governing equation is used to account for the effect of the cell's deformation on the flow field calculation. The deformed or moving cell velocity vector \mathbf{u}_c is calculated through obeying the continuous geometric conservation law, Eq. (3.17). The LHS represents the time change of the cell's volume while the RHS is the corresponding change in cell boundaries.

$$\frac{\partial}{\partial t} \int dV = \int \mathbf{u}_c \cdot \mathbf{n} dS \quad (3.17)$$

The ALE formulation is obtained by replacing the mixture velocity \mathbf{u}_m Eq. (3.1) by the corrected mixture velocity term $(\mathbf{u}_m - \mathbf{u}_c)$. The same correction is also performed on the LHS of Eq. (3.4), therefore it reads as

$$\begin{aligned} & \frac{\partial}{\partial t} (\rho_m (\mathbf{u}_m - \mathbf{u}_c)) + \nabla \cdot (\rho_m (\mathbf{u}_m - \mathbf{u}_c) \mathbf{u}_m) \\ &= \rho_m \mathbf{g} - \nabla P + \nabla \cdot (\mu_m (\nabla \mathbf{u}_m + \nabla \mathbf{u}_m^T)) + \nabla \cdot \left(\sum_{k=1}^n a_k \rho_k \mathbf{u}_{dr,k} \mathbf{u}_{dr,k} \right) \end{aligned} \quad (3.18)$$

During the unsteady simulation, the unsteady forces acting on the oscillating and neighboring tubes are monitored in both lift and drag directions. The time signal of these forces is recorded and the dimensionless lift ($c_{L,i}$) and drag coefficients ($c_{D,i}$) for the i^{th} monitored tube is given by:

$$c_{L,i}(t) = \frac{F_{x,i}(t)}{\frac{1}{2} \rho_H U^2 A} \quad (3.19-a)$$

$$c_{D,i}(t) = \frac{F_{y,i}(t)}{\frac{1}{2} \rho_H U^2 A} \quad (3.19-b)$$

where A is the oscillation amplitude (3 mm), while ρ_H is the homogeneous mixture density at the inlet.

A Fast Fourier Transform (FFT) is performed on the recorded force coefficient signals to decompose them into their corresponding magnitudes as force coefficients (c_f) and phases (ϕ) between the unsteady force and the tube motion at each reduced velocity. These extracted parameters provide a quantitative description of the unsteady forces. The extracted values are

compared with the published experimental results by Sawadogo and Mureithi (2014) for validation, and then they are used to predict the stability threshold by implementing them into Eq. (3.15).

3.5. Results and discussion

3.5.1. Sensitivity analyses

Two sensitivity analyses were performed to balance between the simulation's accuracy and computational power. This was done by determining the optimum cell count and time step resolution as these two parameters were found most influential on the unsteady force coefficients and phases. Three unstructured and quadrilateral meshes were used for the analysis with different cell counts 88,000, 133,000, and 205,000 cells, or M1, M2, and M3. These different meshes correspond to average cell sizes of 2 mm, 1 mm, and 0.75 mm, respectively, in the vicinity of the tubes as well as upstream and downstream zones. Close to the tubes and wall boundaries, the three meshes shared the same mesh refinement. The refinement zone is characterized by a structured cell arrangement with a 10 mm inflation height ($0.26D$) and 14 inflation layers. The height of the adjacent layers to the boundaries was selected to produce $y^+ \leq 1$. Figure 3.3 shows the inflation layers around the tubes and the topology of the mesh in their vicinity.

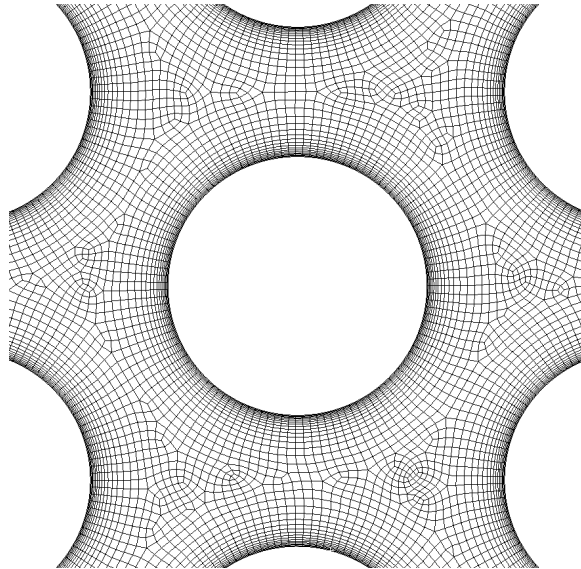


Figure 3.3: Mesh topology and refinement around the tubes.

Figure 3.4 shows the prediction of the lift coefficient obtained using the three meshes as compared with the experimental counterpart at a reduced velocity of 9.5. At this reduced velocity, a significant dependency for the lift coefficient on the cell size was observed. For both 0% air void fraction or pure water and 60% air void fraction, meshes M2 and M3 give a good prediction of the lift coefficient compared to the experimental values. For 0% air void fraction (Fig. 3.4-a), the errors for M2 and M3 meshes are 13% and 4% respectively, while for M1 the error is 470%. The same order of errors is also noted for the 60% air void fraction (Figure 3.4-b) with errors of 300%, 37%, and 29% for meshes M1, M2, and M3 respectively. Thus, there is a quite small difference between the values obtained from M2 and M3. As such, mesh M2 was chosen because it requires less computation time and power.

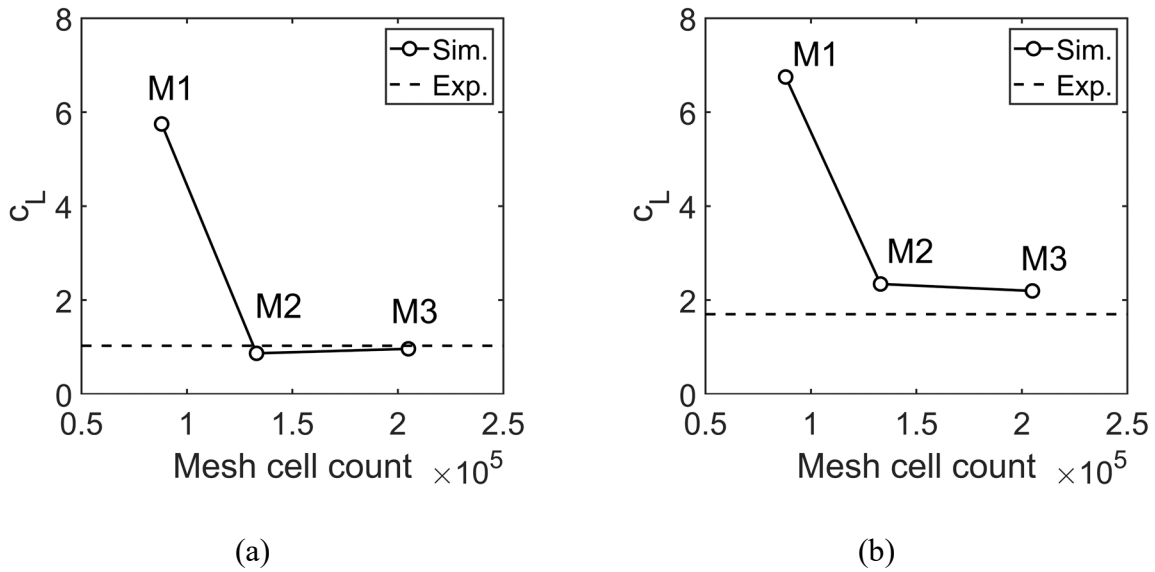


Figure 3.4: Mesh sensitivity at $U_R = 9.5$: (a) 0% air void fraction, (b) 60% air void fraction.

This mesh (M2) was used to find the optimum time step resolution in terms of accuracy and computational time. Time step was varied between 8 ms and 0.1 ms for 0% and 60% air void fractions. This analysis is performed at reduced velocity of 6.6. In Fig. 3.5, generally, the change in the estimated values of the lift coefficient and phase angle between the 1 ms and 0.1 ms time steps is minimal for both single- and two-phase cases. The single-phase flow case (Fig. 3.5-a) shows higher dependence on the time resolution than the two-phase counterpart. This is more

evident in the larger variation of the force phase for the single-phase flow compared to the two-phase flow. Consequently, the 1 ms time step will be utilized as a compromise between accuracy and computational cost. Moreover, when the central tube oscillates with 8 Hz the selected time step generates more than 125 data points per cycle which is seen adequate to predict the unsteady change of the forces with confidence.

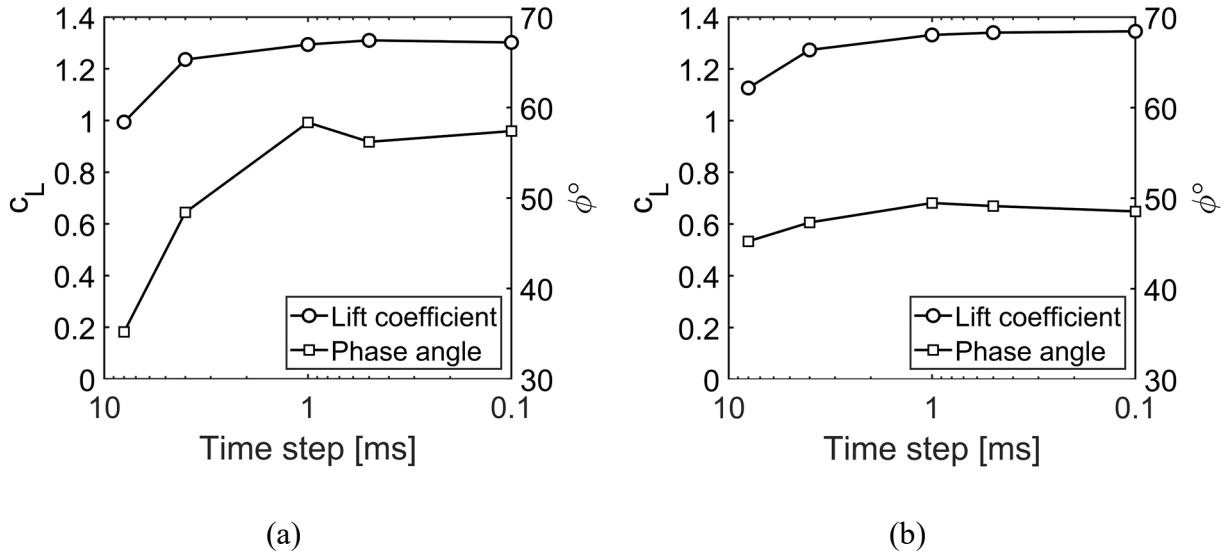


Figure 3.5: Time step sensitivity at $U_R = 6.6$: (a) 0% air void fraction, (b) 60% air void fraction.

A third sensitivity analysis was performed on the bubbles' Sauter-mean diameter specified at the inlet of the domain. The numerical model used allows for the coalescence and breakup of the bubbles in the domain due to bubbles collision and wake entrainment for the first case, and turbulent eddies for the second. Thus, the numerical value of the bubble's diameter is not as important as its effect on the interaction between the air and water phases in the flow. The mean slip between the air and water phases in the vicinity of the tube bundle was used to select the optimum bubble size at the inlet area. Feenstra et al. (2000) developed a universal dimensionless model for the prediction of the mean slip in tube bundles which was used to accurately estimate the volume fraction of the dispersed phase. The model utilizes the dimensionless Capillary and Richardson numbers to model the two phases interaction and gravity effects, and the pitch-to-diameter ratio to describe the bundle geometry. The estimated slip from this model showed a very good agreement with measured value over a wide range of mixtures and flow conditions. The numerical value of the Sauter-mean diameter of the air bubbles at the inlet was varied from 0.01

mm up to 3 mm. The unsteady flow field velocities of the phases were recorded until the solution reached a steady periodic behavior, then the ensemble average of the absolute slip in the domain was calculated over 1000 time-steps. Figure 3.6 shows the distribution of the temporal-averaged slip in the tube bundle. The figure is based on 5 m/s gap velocity and 50% air void fraction with bubbles of a size of 0.1 mm diameter introduced at the inlet. Zones of high slip are at locations where the flow changes its direction to pass in the channels between tubes. For these flow conditions and bundle configurations, the mean slip estimated by Feenstra's model is 3.22. As shown in Fig. 3.7, the calculated mean slip from introducing fine bubbles at the inlet gives a closer agreement to the Feenstra model's slip value. For instance, with 0.01 mm inlet bubble size, the mean slip was found to be 2.437, and for 0.1 mm diameter the mean slip was 2.69. These two values correspond to errors of 24% and 16% respectively. When using larger bubble sizes above 0.1 mm, the error exceeds 100%. These high slip values result from the increase in the lag between the motion of the bubbles and water flows. In a dimensionless form, this is represented by larger values of Stokes number calculated for bubbles. Thus, the 0.1 mm Sauter-mean bubble diameter was enticing to be selected for the rest of the numerical analysis.

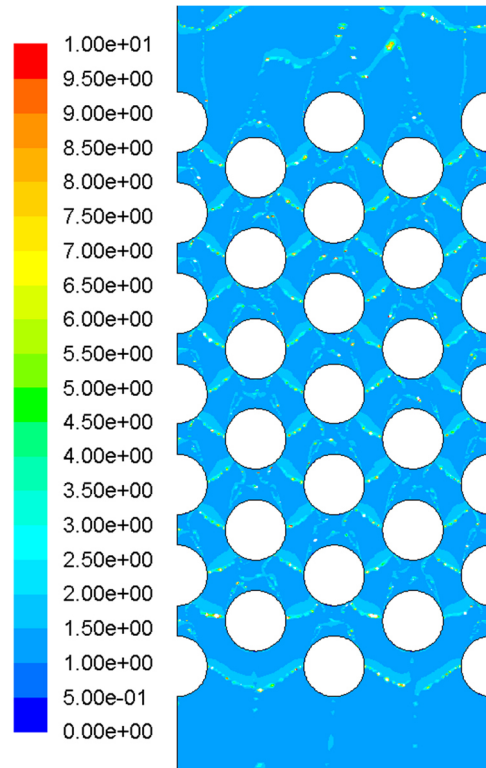


Figure 3.6: Contours of absolute slip in the vicinity of tube bundle.

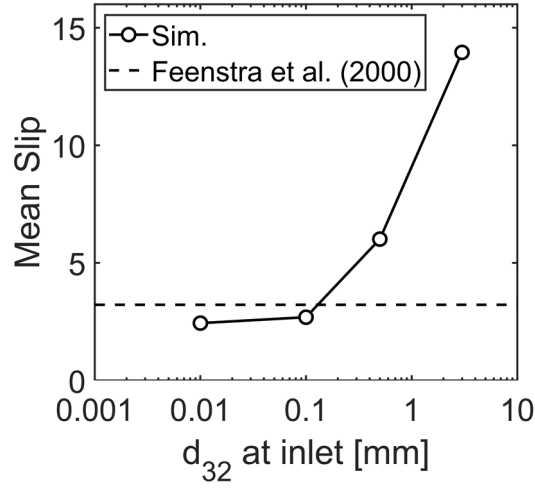


Figure 3.7: Mean slip variation with the bubble Sauter-mean diameter at inlet.

3.5.2. Data validation

Firstly, a detailed comparison for the flow structure between the simulated flow and the experimental obtained by Pettigrew et al. (2005) was carried out at the same conditions used for the slip check. The 0.1 mm Sauter-mean diameter value was tested. Figure 3.8-a compares the air void fraction distribution at four different sections of the flow channel. Generally, there is a good agreement quantitatively between the simulation and the experimental data. The air void fraction levels in both cases are around 45% for the four sections. However, for the simulation case, the distribution is more flat and uniform in the flow channel than the experimental counterpart. This is a reasonable agreement and the model seems to capture the distribution of air void fraction in the gap between cylinders. When the flow changes its direction around due to the curvature of the flow path in the channel, some phase segregation takes place. As such higher air phase concentration tends to exist in the inner of the turn as it has less inertia than water phase which concentrates on the outer side. This behavior is evident in the experimental measurement and it is captured well by the model close to the walls of the cylinders. Iwaki et al. (2005) used a non-intrusive PIV system to measure the air bubbles distribution in an inline and staggered tube bundles. Their measurements and observation showed that for flows with velocities high enough to overcome the effect of buoyancy, the air bubbles become trapped in the wake of the tubes and higher air void fraction is measured in this region. In Fig. 3.8-b, the distribution air bubbles velocity magnitude through the flow channel between the tubes was investigated and compared to the

experimental values. Through the four sections where the investigation was carried on, there is a very good agreement in both magnitudes and trends which gives more confidence in the selected inlet bubbles' size.

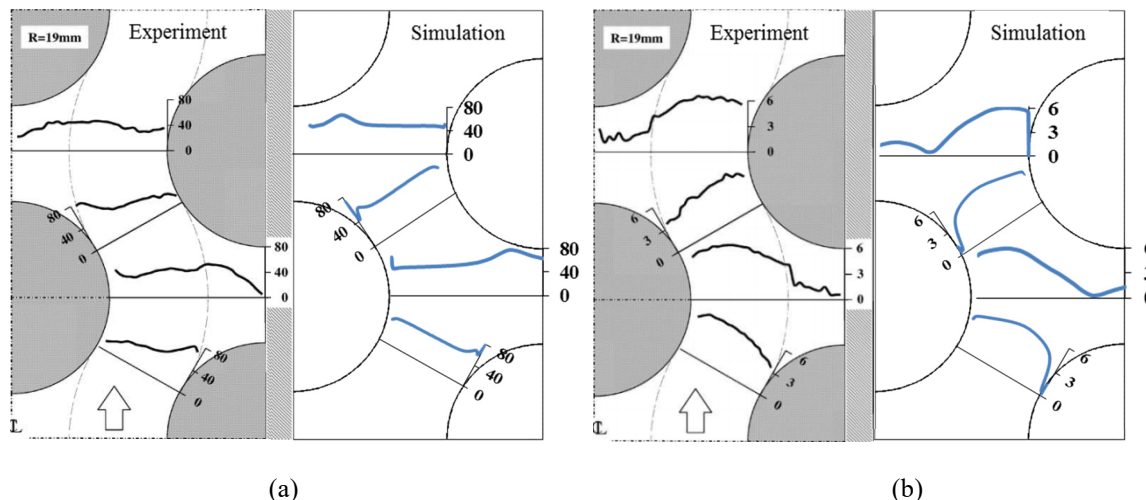


Figure 3.8: Comparison between experimental measurements of (Pettigrew et al., 2005) and simulation results for 50% air void fraction and $U=5$ m/s for the temporal average of: (a) air void fraction, (b) air bubble velocity [m/s].

The aforementioned sensitivity and comparisons with experimental results have given a degree of confidence in the developed model. The model was then utilized to simulate the unsteady flow forces acting on the moving tube bundle with a water flow. The results were compared with the corresponding experimental measurements provided by Sawadogo and Mureithi (2014) as shown in Fig. 3.9. The variations of the unsteady force's lift coefficient and phase angle with the gap reduced flow velocity are illustrated in Fig. 3.9. The comparison demonstrated the ability of the model to predict the unsteady fluid forces as evident from the excellent agreement between the simulated and experimental lift coefficients. In Fig. 3.9-b the agreement is only noticed in the low range of gap reduced velocity up to 5. In this range the flow forces slightly lag the motion of the tube. For reduced velocity above 5, the experimentally measured force's phase angle becomes negative which means that the flow forces lag tube motion. On the other hand, the magnitude of the simulated phase angles is in good agreement with the experimental counterparts but in the opposite direction. The predicted fluid force phase leads the motion of the tube (positive phase angle). The stability of a single flexible tube in a tube bundle is controlled by the energy exchange between the flexible tube's motion and the resulting flow forces. Such an exchange establishes a

feedback loop and tube becomes unstable if the total damping becomes negative. This condition exists if the fluid forces lead the tube motion which strengthens the energy feedback loop. In their experimental measurements for the unsteady forces in an inline square tube arrangement, Tanaka and Takahara (1981) showed a leading flow lift force acting on a moving tube in the lift direction for air flow.

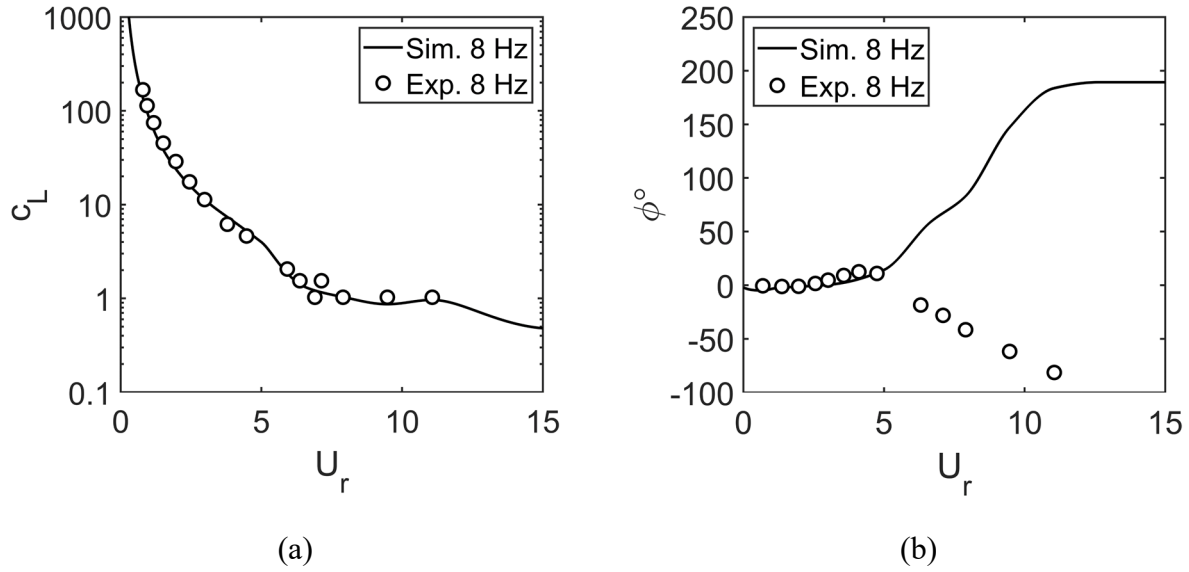


Figure 3.9: Lift force coefficient and phase acting on tube C when it oscillates in x-dir compared to the experimental data of (Sawadogo & Mureithi, 2014). For 0% air void fraction: (a) lift force, (b) phase angle.

3.6. Unsteady forces in two-phase flow

Figure 3.10 represents a comparison between the experimental and simulation unsteady forces acting on the moving tube (c) and obtained at various air void fractions which cover a wide range of mixtures, namely 15%, 60%, 80%, and 95% air void fractions. Sawadogo and Mureithi (Sawadogo & Mureithi, 2014) presented an excellent set of experimental data covering a range of air void fraction from 40% to 90%. They found that the data of the different air fractions collapses well and they presented a single line fit to all air void fractions. This fit line is used as the representation for the experimental data in current study. The simulated lift coefficients and phases also indicate that they are quite dependent on the reduced flow velocity parameter only and the air void fraction has no effect. There is also a good agreement between both the simulation and experimental results for the force coefficient phases. Such an agreement in the force values and

independency of the air content in the mixture emphasize that the model is capable of presenting the flow/structure interaction mechanism.

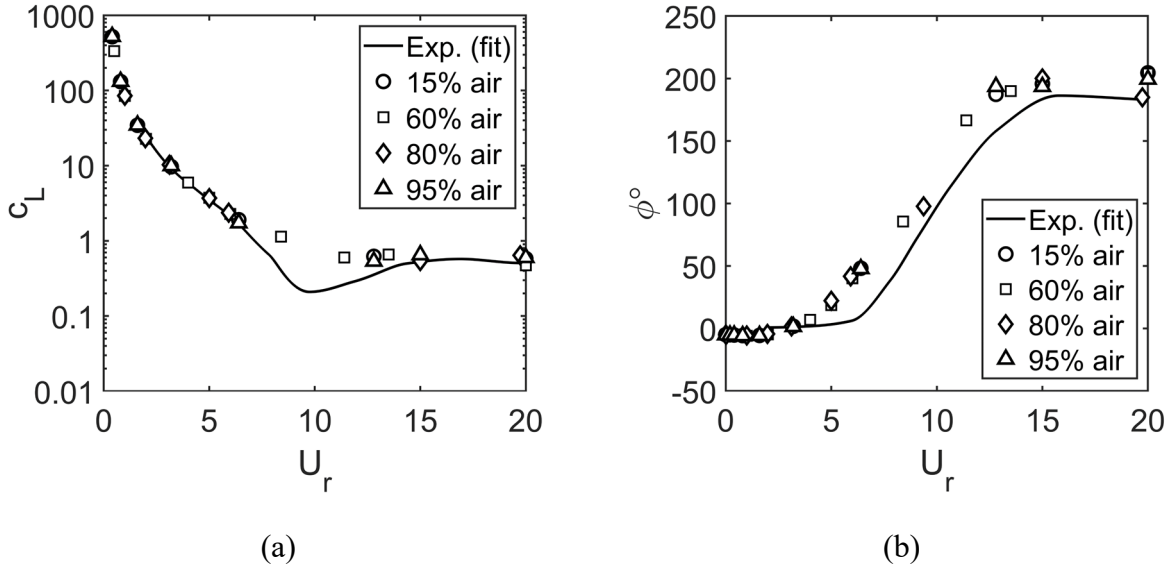


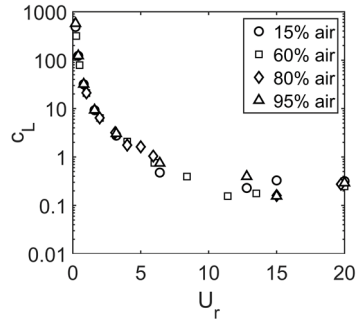
Figure 3.10: Experimental and simulated lift force coefficient magnitude and phases at different air void fractions for tube c: (a) lift coefficient, (b) phase angle.

Comparisons for the force coefficients on other neighboring tubes were not possible because of the lack of experimental data. Figure 3.11 depicts the lift coefficients and their corresponding phases at different air void fractions. The tubes presented in the figure are tubes N (a and b), S (c and d), NE (e and f), and SE (g and h). These designations such as N, S, NE, SE, etc. are illustrated in Fig. 3.2. The other two tubes NW and SW are not presented as the forces acting on them are nearly identical to those on tubes NE and SE, respectively. The aforementioned data collapsing feature is still evident, most prominently for the lift coefficients. However, some of the phase angles become void-fraction dependent at higher reduced flow velocities ($U_r > 6.5$). An example of such dependence is shown in the results for the phase angle of tube N (plot b).

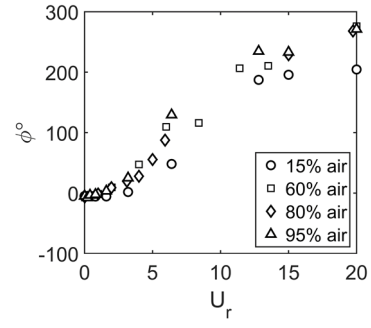
3.7. Stability Threshold Prediction

3.7.1. Hybrid Analytical-CFD Model

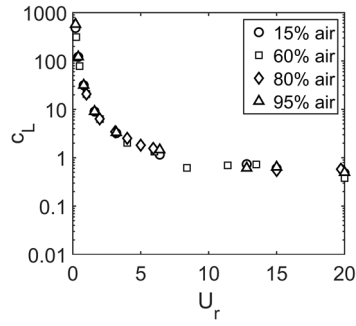
The stability threshold is obtained using the unsteady force for the full range of air void fractions (from 0% to 100%). Curve fits of the above data represented in Figs. 3.10 and 3.11 were utilized



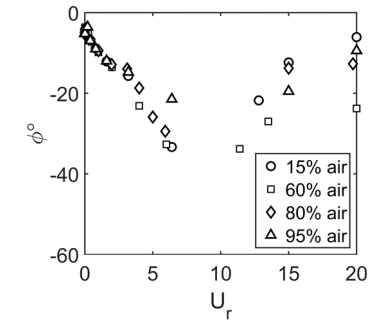
(a)



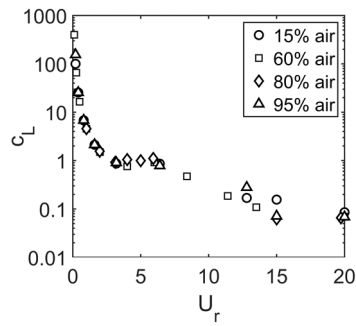
(b)



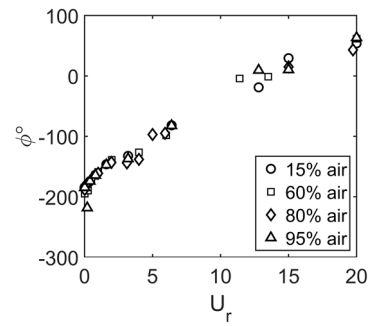
(c)



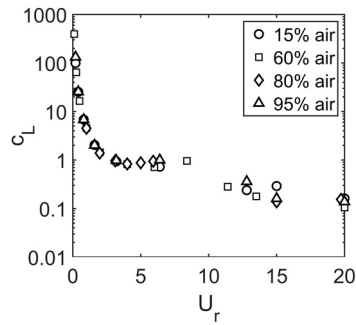
(d)



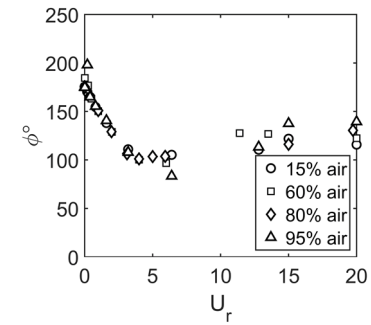
(e)



(f)



(g)



(h)

Figure 3.11: Simulated lift force coefficients magnitude and phases at different air void fractions: (a and b) N tube, (c and d) S tube, (e and f) NE tube, (g and h) SE tube.

in the stability prediction. This excludes the 0% air void fraction (pure water) case. For single-phase water flow, numerical simulations were run separately and force coefficients obtained are used for its threshold calculation. For all cases, a cluster of 7 tubes was used to simulate a flexible tube bundle allowed to oscillate only in the lift direction. Each tube is 38 mm in diameter. The tubes natural frequency was set to 8 Hz. The mass damping parameter was varied in the range of 0.01 to 1000 for the water case, while from 0.03 to 3 for the two-phase flow case. Each mass damping parameter was obtained by adjusting the density of the fluid as it practically represents the change from single phase water to a single-phase air, while for the pure water case, the mass of the tube was made variable.

For each reduced velocity, an initial mass damping parameter was set. The reduced flow velocity was used to obtain the force coefficient values. The force coefficients are then used to estimate the added mass, stiffness, and damping 7x7 matrices. Then, an eigenvalue analysis was performed on the system equation (Eq. (3.15)). The process is repeated by incrementing the reduced velocity and the stability threshold is obtained when the real part of the complex eigenvalue changes its sign. The mass-damping parameter used in presenting the simulations is based on the in-vacuu damping logarithmic decrement $\delta = 0.012$.

The predicted stability threshold for single-phase water flow is compared with the experimental data for the same geometry and air flow reported by Weaver and Fitzpatrick (1988), as depicted in Fig. 3.12. The prediction agrees very well with the experiments. Two changes in the threshold curve slope are found at mass damping parameters of 0.5 and 3. These correspond to reduced velocities of 5 and 10.5, respectively, and they are due to the changes of the slope of the phase curve for the central tube as can be seen in Fig. 3.9. For the two-phase flow cases, the stability threshold is produced in Fig. 3.13 and compared to the experimental data of Pettigrew (1989) for air-water flow. The generated instability threshold agrees to a reasonable degree with experiments. The prediction is particularly excellent when the void fraction is very low or very high, i.e. approximately single-phase flow. Moreover, in the middle range of air void fraction, the prediction is still good with conservative estimation of the threshold compared to the experimental counterpart.

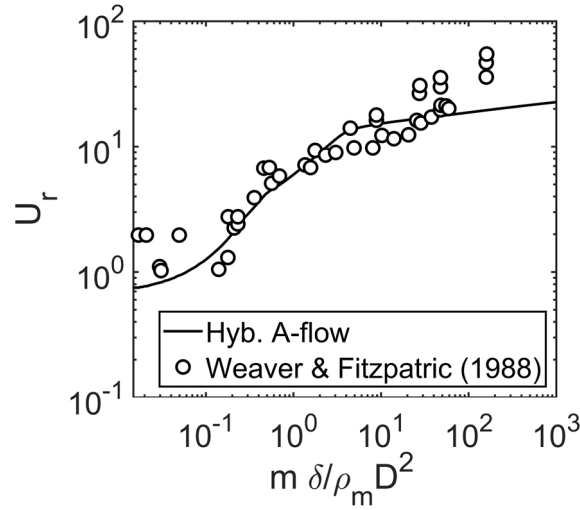


Figure 3.12: Stability map comparison between the simulation and experiments for 0% air void fraction.

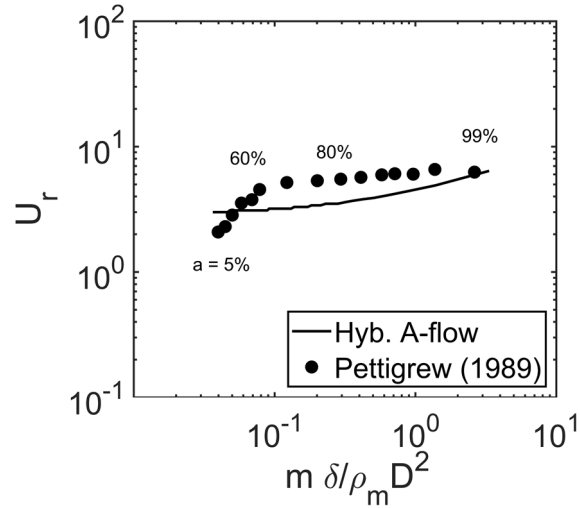


Figure 3.13: Stability threshold map obtained from the two-phase flow unsteady forces simulations vs. experimental data from Pettigrew (1989) for air–water flow.

3.7.2. Direct Flow/Structure Simulation

Another attempt was carried out to directly couple the motion of the tubes and the flow unsteady forces. This was achieved by solving the fluid equations which yields the velocity and pressure field within the tube bundle. Then the pressure is integrated around every cylinder leading to the estimation of the fluid forces at every time step. The resulting fluid forces are used in the tube dynamic model, Fig. 3.1, and tube response is calculated. The new set of tube response is then used to update the tube position within the computation fluid dynamics calculations. This process

is repeated every time step. At the beginning of the simulation, the central tube was given an initial displacement of 3 mm, and the time-evolution pattern of the displacement for the 7 tubes in the kernel is monitored. The tubes were considered unstable when the vibration amplitude of any tube is growing resulting in a negative damping. A sample of this monitored data is shown in Fig. 3.14. The signal of the tube C is presented for a direct flow/structure coupling simulation for 60% air void fraction and reduced velocity of 2.8. The tube response demonstrates amplitude modulations which are indicative of strong inter-tube coupling as opposed to the pure damping-controlled mechanism of the single tube case. Relative modal patterns at instability were observed with neighbouring tubes being approximately 180 degrees out-of-phase or directly in-phase. The effective damping was determined by fitting an exponential curve to the envelope of the modulation peaks.

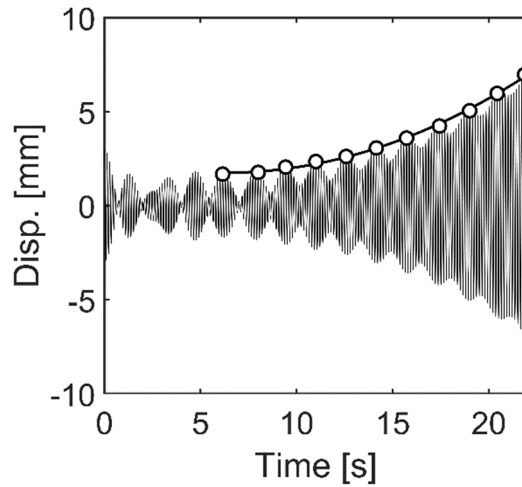


Figure 3.14: Time response of tube C and for 60% air void fraction at $U_r = 2.8$.

The simulations for direct flow/structure coupling were performed at six air void fractions, namely, 15%, 40%, 60%, 80%, 95%, and 99%. At each air fraction, the density of the flow is calculated to set the mass-damping parameter's value. Then the reduced velocity is incremented from a low stable value up to the value which causes the instability. The instability threshold obtained with this technique is in good agreement with Hybrid Analytical-CFD model's prediction; however, it gives a slightly better agreement with the experimental data at low air void fractions less than 15%, Figure 3.15. In general, this enhancement of the instability threshold prediction can be attributed to less number of assumptions embedded in the Flow/Structure coupling to predict the instability

threshold compared to the unsteady model. For example, the assumption of the linear superposition of the fluidelastic forces acting on a particular cylinder due to the motion of the neighbouring cylinders.

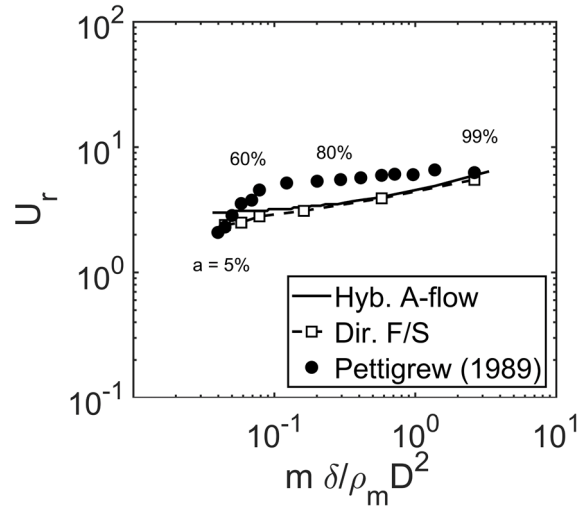


Figure 3.15: Stability threshold map obtained from the two-phase flow unsteady forces simulations and Direct Flow/Structure coupling vs. experimental data from (Pettigrew, Tromp, et al., 1989) for air-water flow.

3.8. Conclusions

A numerical two-phase flow model was developed to simulate the flow inside tube bundles. The model is based on the simple mixture and drift-flux models along with a one-equation Spalart-Allmaras turbulence model. Sensitivity analyses were done over the size of the mesh elements and the time step used for the simulations to obtain optimum values for these parameters. It was found that the air bubble size has a major effect on the interaction between the flow phases. Therefore, the model was developed to allow for the air bubbles breakup and coalescence within the flow domain by introducing the interfacial area concentration concept. Predictions of the developed model agrees well with the dimensionless Feenstra model for mean slip (Feenstra et al., 2000), and to the experimental data provided by (Pettigrew et al., 2005) for void fraction and air velocity distribution for a similar tube bundle.

The developed model was utilized to simulate the unsteady forces acting on an oscillating tube in the lift direction for a parallel triangular tube array at various air void fractions. The simulation results were compared with the experimental data provided by (Sawadogo & Mureithi, 2014). The

comparison showed a good agreement in terms of the unsteady force coefficient and phase with the experimental data for the whole range of studied void fractions. The simulated unsteady forces were utilized to obtain the stability threshold map for a kernel of 7 tubes flexible in the lift direction, which showed a good agreement with the experimental results.

Direct flow/structure coupling simulations were carried out as another approach to predict the onset of the fluidelastic instability at an air fraction ranged from 15% to 99%. The simulation showed a stability threshold that is similar to that obtained from the unsteady force model. While at low void fractions of 15%, it had a better agreement with the experimental data. The developed model seems to capture the main essence of the two-phase fluidelastic instability. Further development and study of this numerical model is required to tackle more realistic two-phase flows which incorporate the effects of phase change and mass transfer between the phases on the threshold instability.

Chapter 4. Numerical simulation of streamwise fluidelastic instability of tube bundles subjected to two-phase cross flow

Complete citation

Sadek, O., Mohany, A., & Hassan, M. (2020). Numerical simulation of streamwise fluidelastic instability of tube bundles subjected to two-phase cross flow. *Journal of Fluids and Structures*, 92, 102816. <https://doi.org/10.1016/j.jfluidstructs.2019.102816>

Copyright

Published in accordance with the Journal of Fluids and Structures' copyright agreement (Appendix A).

Author's contribution

O. Sadek: Conceptualization, Methodology, Software, Data curation, Writing- Original draft preparation.

A. Mohany: Supervision, Methodology, Writing- Reviewing and Editing, Resources, Funding acquisition.

M. Hassan: Supervision, Methodology, Writing- Reviewing and Editing, Visualization.

Abstract

This work aims to develop and validate a numerical model to simulate the flow-structure interaction in tube bundles subjected to two-phase flow. The model utilizes a mixture multiphase module in which a drift flux formulation is used to account for the slip between the phases. Two methods of numerical flow-structure interaction are used to predict the onset of fluidelastic instability (FEI) in the streamwise direction for a two-phase air-water flow mixture in parallel triangular tube bundles. These models are the hybrid analytical-flow field model and the direct numerical flow/structure coupling model. This work investigates the effects of void fractions in the range of 20% to 80% and several pitch-to-diameter ratios (P/D) in the range of 1.3 to 1.7. The

results of the fluidelastic forces and the stability threshold are validated against the experimental data available in the literature and show an excellent agreement. The streamwise FEI threshold shows a significant dependency on the pitch-to-diameter ratio while the void fraction exhibits a lesser effect. Generally, the stability threshold increases as the pitch-to-diameter ratio increases. The model that was developed paves the way for devising of more reliable prediction tools for FEI in steam generators.

Keywords

Fluidelastic instability, Two-phase flow, Numerical modeling, Flow-structure interaction, Tube bundles, Steam generators.

4.1. Introduction

The integrity of tube bundles is an important aspect in the design and operation of steam generators. This integrity can be compromised due to several mechanical issues among which flow-induced vibration is a major factor. Fluidelastic instability (FEI) has been considered to be one of the most devastating phenomena to the structural integrity of steam generators. This phenomenon was first observed by Roberts (1962b) in a row of circular cylinders. It was attributed to the jet switching of the flow between the cylinders and was postulated that the phenomenon is due to a self-excited mechanism. Later, Connors (1970) investigated a single row of cylinders, and this work resulted in a relationship similar to that of Roberts (1962b). This relationship relates the onset of instability to the mass and damping characteristics of the array. While the relationship was first proposed by Roberts (1962b), it is widely known as the Connors equation. Due to its simplicity, the equation was the subject of intensive work in order to fit it to the existing experimental data and use it as a conservative guideline. More comprehensive analyses and models for FEI have been developed, which give more insight into the physics of the phenomenon. These include the quasi-steady model (Price & Paidoussis, 1983), the unsteady model (Tanaka & Takahara, 1981), and the semi-analytical flow channel model (Lever & Weaver, 1982; Yetisir & Weaver, 1993).

In the last two decades, numerical models based on the computational fluid dynamics (CFD) technique have been utilized to study FEI, such as the work of de Pedro et al. (2016), de Pedro and Meskell (2018), Hassan et al. (2010), Khalifa et al. (2013), Burns et al. (2014) and El-Bouzidi and Hassan (2015). These studies demonstrated how these models can be employed to extract important information that can be utilized in analytical techniques to predict FEI.

The majority of the experimental investigations have shown that arrays of tubes under FEI were observed to oscillate predominantly in the transverse direction. This direction is perpendicular to the axis and the flow vector of the tubes, although at high enough flow velocities, oscillations in the flow direction (streamwise) were also observed. It is generally accepted that if FEI does not occur in the transverse direction, streamwise FEI will not occur. For decades, most of the research work in this area has therefore focused on the transverse FEI for both single and two-phase flows (Weaver & Koroyannakis, 1983; Weaver & Schneider, 1983). In one of the earlier studies conducted on U-bend tube bundles, Weaver and Schneider (1983) showed that it is possible for instability to occur in the streamwise direction. In this study, two flow directions were investigated: a flow in the plane of the U-bend, and a flow perpendicular to the plane of the U-bend. FEI instability occurred in the same direction (the direction with the lowest natural frequency) irrespective of the flow direction. This was the first indication of the occurrence of streamwise FEI. The occurrence of such a phenomenon was later confirmed by Weaver and Koroyannakis (1983), who conducted experiments on straight tubes in a water tunnel. Again, it was found that irrespective of the flow direction, FEI would occur in the direction with the lowest natural frequency (transverse or streamwise). Almost two decades later, the work on streamwise FEI was revived by a series of investigations (Hassan & Mohany, 2012, 2016; Janzen et al., 2005; Mohany et al., 2012; Mureithi et al., 2005). The interest in the streamwise FEI was intensified after many tubes failed in the SONGS (San Onfre Nuclear Generation Station) replacement steam generator. Mureithi et al. (2005) investigated the effect of the preferential stiffness of the tubes on the onset of the FEI. Their work showed clearly that streamwise FEI could occur. In a series of papers, Nakamura et al. (Nakamura et al., 2016; Nakamura et al., 2011, 2014; Nakamura & Tsujita, 2017) demonstrated that FEI can occur in all types of tube arrays except for the inline tube array. The importance of the stiffness mechanism in the lead-up to the streamwise FEI was also demonstrated. Moreover, they showed that the pitch-to-diameter ratio has an effect on the stability threshold. In addition, Olala and Mureithi (2015) performed detailed measurements for the

unsteady fluidelastic forces acting on a moving tube in two-phase flow. They utilized the measured forces to study the streamwise stability of tube arrays in a two-phase air-water flow using a quasi-steady framework. Similarly, Olala and Mureithi (2016) showed the importance of the stiffness mechanism in an air-water two-phase flow. Their predicted critical velocities agreed reasonably well with the experimental results of Violette et al. (2006).

Analytical and numerical investigations regarding the streamwise FEI were lacking due to the complex nature of the phenomenon. One of the earlier attempts to model streamwise FEI was carried out by Hassan and Weaver (2015). A simple unsteady streamwise FEI model was utilized to study the effects of support clearance and preload on the FEI of loosely supported tubes. The results demonstrated the strong effect of the tube/support interaction on both transverse and streamwise FEI. The results obtained from this study explained some of the observations regarding recent tube array failures (SONGS). Later, Hassan and Weaver (2017a, 2018, 2016, 2017b) developed a theoretical model based on the flow cell model of Lever and Weaver (1982). The model demonstrated its ability to predict both transverse and streamwise FEI and was verified against experimental data.

The above review points to the importance of considering streamwise FEI as one of the major causes of tube failures in recently installed units and the continuing efforts both experimentally and analytically to understand and characterize the phenomenon. The analytical and numerical efforts are still lacking and confined primarily to single phase flow. More efforts are required to model this phenomenon in order to replicate the conditions in real nuclear steam generators; therefore, this work focuses on developing a numerical model which is capable of simulating the streamwise FEI in two-phase flows. The modelling is carried out utilizing CFD/structural techniques. Simulating streamwise FEI using this approach has not been attempted previously, and as demonstrated in this work, it presents a viable technique that can be used in predicting two-phase streamwise FEI in tube arrays.

4.2. System modelling

The numerical model used in this work consists of two sub-models. The first sub-model simulates the flow field while the second sub-model simulates the structural flexibility. The flow field sub-model is intended to solve for the flow field and simulates the flow forces on each surface in the domain. The prediction of the stability threshold in the tube arrays is carried out using two techniques: a hybrid analytical model and direct flow/structure coupling.

4.2.1. Flow field model

Fluidelastic instability is a different phenomenon from turbulent buffeting, in which the destabilizing fluid forces occur as a direct result of the tube motion. Unlike turbulence, it is not sufficient to simulate/measure the fluid forces on a static tube. Therefore, characterizing fluidelastic force must be done either experimentally or numerically by moving a tube and measuring/predicting the resulting force due to this motion. The natural fluid forces due to the static structure geometry are not of interest. In this work, the fluid forces due to the prescribed tube motion are of interest. In other words, only the forces that occur at the frequency of the oscillating cylinder are of concern. It is reasonable to assume that, deep in the array, the upstream turbulence will not have a significant effect on either the motion-dependent fluid forces or on the resulting instability. As a result, all of the fluidelastic instability models which have been developed, including the quasi-static model (Blevins, 1977; Connors, 1970), the quasi-steady model (Price & Païdoussis, 1983), the semi-analytical model of Lever and Weaver (1982), and the unsteady models (Chen, 1987; Tanaka & Takahara, 1981) did not consider the turbulence to have a significant effect on the fluidelastic instability. Turbulence modelling was therefore not included in all of these models. As such, the precise account of the turbulence excitation is not of great importance. A reasonable model of the turbulence should therefore suffice when modelling fluidelastic phenomena. An approach such as the large eddy simulation (LES) is considered to be an accurate technique for modelling turbulence but it is one of the most computationally burdensome. A less computationally expensive alternative is the detached eddy simulation (DES). The RANS approach has been utilized in many practical applications, which include fluid-structure interaction problems in tube arrays (Hassan et al., 2010; Mohany et al., 2014). This approach has shown great potential for modelling FEI force with reasonable accuracy.

In the flow field sub-model, the Reynolds Averaged Navier-Stokes equations (RANS) were used and supplemented with a turbulence model to form the basic governing equations for the flow field. Several turbulence models were tested including Spalart-Allmaras (1992b), Standard K- Ω , Menter's shear stress transport (SST), and the Reynold's stress model. The numerical treatment for the two-phase flow utilized a drift flux formulation. The fundamental concept of the drift-flux model is the formulation of two separate phases as a mixture phase. As such, the fluid properties are represented by the properties of the mixture while accounting for the effect of the coupling of each phase on the conservation equations. Consequently, constitutive assumptions must be made, leading to the simplification of some two-phase flow characteristics. The coupling of the phases is expressed by using drift-flux parameters to consider the effects of interfacial shear and flow regime transitions on the conservation equations. The model is known to be more suitable for cases of high homogeneity of the phase flows and is not adequate for highly segregated two-phase flows, such as in cyclone applications. While some of the two-phase characteristics may not be modelled properly, the drift flux model has exhibited success in modelling two-phase flow in tube arrays. In a previous investigation, Sadek et al. (2018) demonstrated the success in adopting this model to predict the stability of tube arrays subjected to two-phase flow.

The averaged properties of the flow mixture were used to solve the continuity and the RANS equations as follows:

$$\frac{\partial}{\partial t}(\rho_m) + \nabla \cdot (\rho_m \mathbf{u}_m) = 0 \quad (4.1-a)$$

$$\begin{aligned} & \frac{\partial}{\partial t}(\rho_m \mathbf{u}_m) + (\mathbf{u}_m \cdot \nabla)(\rho_m \mathbf{u}_m) \\ &= \rho_m \mathbf{g} - \nabla P + \nabla \cdot (\mu_m (\nabla \mathbf{u}_m + (\nabla \mathbf{u}_m)^T)) + \nabla \cdot \left(\sum_{k=1}^n a_k \rho_k \mathbf{u}_{dr,k} \mathbf{u}_{dr,k} \right) \end{aligned} \quad (4.1-b)$$

where the subscript m refers to the mixture, and ρ_m , μ_m and \mathbf{u}_m are the local mixture density, the dynamic viscosity, and the velocity vector respectively.

This treatment does require a transport equation to be solved for the local void fraction of the air phase, a , to facilitate the calculation of the local inter-phase forces, as shown in Eq. (4.2). In this form, the transport equation neglects the phase change as well as the exchange of material between the air and the water phases, yet it accounts for the drift between them.

$$\frac{\partial}{\partial t} (a \rho_{air}) + \nabla \cdot (a \rho_{air} \mathbf{u}_m) = \nabla \cdot (a \rho_{air} \mathbf{u}_{dr,air}) \quad (4.2)$$

The velocity $\mathbf{u}_{dr,air}$ is the local drift flux velocity and it is defined as the difference between the local air velocity and the mixture velocity at the same location. This velocity is estimated using the algebraic drift-flux relations. Originally these relationships were developed for narrow pipes; later they were expanded to cover larger pipes and channels, as well as various flow patterns (Schlegel et al., 2010).

Bubbles usually have a certain size distribution, which can be expressed in the form of a distribution curve. Frequently, this data is utilized in the form of a single length scale. Several length scale values have been used for expressing the average value of the size of the bubbles, including simple arithmetic, geometric, and harmonic means. The Sauter mean diameter (SMD) is one of the widely used length scale expressions. The SMD represents an estimation of the interfacial area per unit volume. The Sauter mean diameter (d_{32}) is defined as (Sauter, 1926):

$$d_{32} = \frac{\int_{d_{min}}^{d_{max}} d^3 P(d) dd}{\int_{d_{min}}^{d_{max}} d^2 P(d) dd} \quad (4.3)$$

where d_{min} , d_{max} , and $P(d)$ are the minimum, the maximum, and the frequency distribution curve of the diameter of the bubbles, respectively.

The Sauter mean diameter (d_{32}) of the bubbles is also related to the interfacial area concentration, χ , and the void fraction as follows:

A transport equation is therefore solved for χ [Eq. (4.5)], which considers the breakup and the coalescence of air bubbles through introducing the turbulent eddies source term (S_{TE}), the sink terms due to random collisions (S_{RC}), and the wake entrainment (S_{WE}). These terms are derived assuming perfect spherical bubbles:

$$\frac{\partial}{\partial t} (\chi \rho_{air}) + \nabla \cdot (\chi \rho_{air} \mathbf{u}_{air}) = \frac{1}{3} \frac{D\rho_{air}}{Dt} \chi + \rho_{air} (S_{TE} + S_{RC} + S_{WE}) \quad (4.5)$$

$$S_{TE} = \frac{1}{18} C_{TE} \mathbf{u}_{air} \left(\frac{\chi^2}{a} \right) e^{-\frac{We_{cr}}{We}} \sqrt{1 - \frac{We_{cr}}{We}}, \quad We > We_{cr} \quad (4.6)$$

$$S_{RC} = -\frac{1}{3\pi} C_{RC} \mathbf{u}_{air} \chi^2 \left(\frac{1}{a_{max}^{\frac{1}{3}} (a_{max}^{\frac{1}{3}} - a^{\frac{1}{3}})} \right) \left(1 - \exp \left(-C \frac{a_{max}^{\frac{1}{3}} a^{\frac{1}{3}}}{a_{max}^{\frac{1}{3}} - a^{\frac{1}{3}}} \right) \right) \quad (4.7-a)$$

$$S_{WE} = -\frac{1}{3\pi} C_{WE} \mathbf{u}_{air} \chi^2 \quad (4.7-b)$$

where C_{TE} , C_{RC} , C_{WE} and C are the coefficients estimated experimentally, We and We_{cr} are the local Weber number and the critical Weber number, respectively, at which the bubble becomes unstable and can be broken, and a_{max} is the dense packing limit of the void fraction. The values of these constants are presented by Wu et al. (1998) and Ishii and Kim (2001) for bubbly flow in round pipes.

The structural flexibility sub-model simplifies each flexible tube (i) to a single degree of freedom mass-damper-spring system, which is allowed to vibrate in the streamwise direction only. The general equation for the motion of the tube displacement (y_i) for such system is represented as:

$$m_{s,i} \ddot{y}_i + c_{s,i} \dot{y}_i + k_{s,i} y_i = F_i(y_i, \dot{y}_i, \ddot{y}_i, U_\infty, t) \quad (4.8)$$

where the subscripts s and f denote the structure and the flow, respectively, and m , c , and k are the mass, the damping, and the stiffness constants.

The simulation of the transient fluid force term, F_i , and its variations during the oscillation of the flexible tube, i , is a very crucial step for an accurate prediction of the stability threshold. Generally, the flow force depends on the instantaneous displacement of the flexible tube as well as its dynamic history.

4.2.2. Hybrid analytical-flow field model

This model is based on the FEI unsteady model proposed by Chen (Chen, 1987). The model decomposes the dynamic flow forces acting on a vibrating tube into the inertial, the damping, and the stiffness flow forces. For the case of N neighboring flexible tubes, the motion of the j^{th} tube contributes to the total dynamic force acting on Tube i as well as the motion of Tube j itself. When the motion is restricted to being only in the streamwise direction, the model is reduced to:

$$F_{f,y,i} = -\frac{\pi \rho_m D^2}{4} \sum_{j=1}^N \beta_{ij} \ddot{y}_j + \frac{\rho_m U^2}{\omega} \sum_{j=1}^N \beta'_{ij} \dot{y}_j + \rho_m U^2 \sum_{j=1}^N \beta''_{ij} y_j \quad (4.9)$$

The terms β_{ij} , β'_{ij} , and β''_{ij} represent the added flow mass, the damping and the stiffness influence coefficients of Tube i due to the motion of tube j . The velocity, U , is the gap velocity of the flow between the tubes and can be determined through a knowledge of the tube bundle geometry and the pitch-to-diameter ratio P/D as shown below:

$$U = \frac{P/D}{P/D - 1} U_{\infty} \quad (4.10)$$

The flow added terms can be estimated from direct measurements. These measurements are usually performed by exciting a tube by a predefined harmonic motion, $y_o \sin(\omega t)$, and measuring the induced forces on each tube of interest. The induced force is represented by a normalized force coefficient c_{fy} , and a phase angle ϕ referenced to the motion of the excited tube:

$$\beta'_{ij} = \frac{1}{2} c_{fy,ij} \sin(\phi_{ij}) \quad (4.11-a)$$

$$\beta''_{ij} = \frac{1}{2} c_{fy,ij} \cos(\phi_{ij}) - \frac{\pi^3}{U_r^2} \beta_{ij} \quad (4.11-b)$$

$$c_{fy,ij} = \frac{|F_{fy,ij}|}{\frac{1}{2} \rho_m U^2 y_o} \quad (4.12)$$

where U_r is the dimensionless reduced velocity defined as $2\pi U/\omega D$, and the added mass parameter β_{ij} is calculated from the quiescent flow state. These coefficients are required for an estimation of the fluid forces. The flow computational model was utilized to extract these force coefficients. More details will be given about this model in Section 4.2.5. The implementation of Eq. (4.9) into Eq. (4.8) leads to a homogeneous set of differential equations which represent the coupled motion of the system in following general form:

$$[M]\{\ddot{y}_i\} + [C]\{\dot{y}_i\} + [K]\{y_i\} = \{0\} \quad (4.13)$$

where $[M]$, $[D]$, and $[K]$ are the overall mass, damping, and stiffness matrices that include both the structural and the added fluid force coefficients for the tube kernel. The eigenvalue problem associated with the above system can be established by rewriting the above equation in the state space form as shown in Eq. (4.14-a) or its equivalent form in Eq. (4.14-b):

$$\begin{Bmatrix} \dot{y}_i \\ \ddot{y}_i \end{Bmatrix} = \begin{bmatrix} [0] & [I] \\ -[M]^{-1}[K] & -[M]^{-1}[C] \end{bmatrix} \begin{Bmatrix} y_i \\ \dot{y}_i \end{Bmatrix} \quad (4.14-a)$$

$$\{\dot{q}\} = [A]\{q\} \quad (4.14-b)$$

where $\{q\}$ and $[A]$ are the state vector and the state dynamic matrix, respectively. The eigenvalues of the state are complex. The stability threshold is determined as the condition at which the real part of the eigenvalue vanishes. The state matrix $[A]$ is a function of the reduced flow velocity, which makes $[A]$ a function of the natural frequency of the tube bundle. This results in a nonlinear eigenvalue problem. An iterative procedure was adopted to solve the above eigenvalue problem in which the system matrices are updated after each iteration for each reduced velocity increment. The solution is terminated when the real part of any of the eigen-values changes sign from negative to positive.

4.2.3. Direct flow/structure coupling model

In this coupling approach, the instantaneous motion response of the flexible tubes is calculated at every instant of the time domain. This is achieved by integrating the pressure field around each flexible tube to obtain the net flow force in the streamwise direction, as shown in Eq. (4.15).

$$F_{f,y,i}(t) = \frac{D}{2} \int_0^{2\pi} P_{f,i}(\theta, t) \sin(\theta) d\theta \quad (4.15)$$

Then, with the knowledge of the displacement and the velocity of each tube as well as the external structural forces acting on them, the new instantaneous position is calculated and updated. The instability of the system can be observed from the displacement time signal. An initial excitation is given to the tube at the start of simulation. If the displacement signal grows with time during the simulation, the system is deemed unstable. Similarly, if the displacement decays with time, then the system is considered stable. The exact onset of instability occurs when the amplitude of the displacement signal does not vary with time.

4.2.4. Dynamic mesh treatment

In both of the previously mentioned coupling approaches, the motion of the flexible tubes represents moving surfaces. This requires an additional treatment for the deformed mesh zones

around the moving surfaces. First, the nodes defining the mesh cells adjacent to the moving tubes are allowed to displace from their original location such that they obey a Laplacian diffusion model governed by:

$$\nabla \cdot (\Gamma \nabla \mathbf{w}) = 0 \quad (4.16)$$

Second, the arbitrary Lagrangian-Eulerian (ALE) formulation is implemented to account for the force that the moving surface exerts on the fluid during its motion and the relative velocity between the moving cell and the flow. A geometry conservation principle is applied to assure the continuity of the mesh domain as follows:

$$\frac{\partial}{\partial t} \int dV = \oint \mathbf{u}_c \cdot \hat{\mathbf{n}} dS \quad (4.17)$$

The change in the total volume with time has to correspond to a change in the boundaries of the cells, which is represented by the cell velocity vector \mathbf{u}_c . After that, the cell velocity vector is implemented in Eq. (4.1-a) and Eq. (4.1-b) to correct for the mixture velocity passing the moving cell.

4.2.5. Flow domain and setup

A 2-D domain representing the flow inside a parallel triangular tube bundle was utilized. Although a 3-D domain would be more realistic, a 2-D domain is a reasonable choice considering that the flow is highly organized in the spanwise direction during the FEI. This is usually the case for a flow-coupled phenomena and it has been validated by Romberg and Popp (1999) at the onset of FEI.

A general overview of the flow domain is represented in Fig. 4.1. It consists of 19 tubes arranged in three columns and 14 half tubes on both sides of the tube bundle to mimic the corrugated flow channels within the whole bundle. This minimizes the effect of the straight walls. The tube diameter was fixed at 38 mm while three pitch-to-diameter ratios were considered in this work (1.3, 1.5, and 1.7). The inlet and the outlet boundaries were located at the bottom and the top of the domain; the air-water mixture therefore flowed in an upward direction against gravity. The compressibility of the air phase was neglected as the change in the volume of the air bubbles due to the hydrostatic head difference along the domain height would not exceed 7%. The air-water mixture velocity and the void fraction were set to be uniformly distributed at the inlet boundary and they were allowed to freely redistribute inside the domain. The outlet boundary condition was

set as an entrainment. Upstream and downstream sections were incorporated into the domain to allow the flow to develop before reaching the tube bundle and to minimize any numerical effect of the boundary condition on the flow inside the tube bundle. A length of $5.5 D$ was found to be sufficient for this purpose. As well, five equally spaced baffle plates were incorporated in the downstream section to prevent the formation of vortices behind the last row. During any simulation, the pressure distribution was monitored around the seven full tubes designated as C, N, NE, NW, S, SE, and SW, which formed a cluster in the middle of the array. Then, the instantaneous net drag forces in the streamwise direction were calculated.

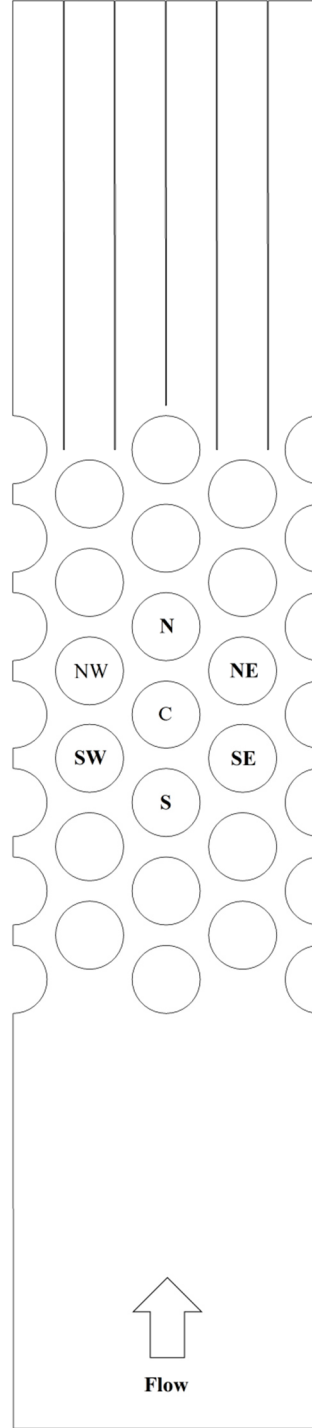


Figure 4.1: Flow domain.

The tube mass, the logarithmic decrement δ , and the natural frequency of the tube were fixed throughout this work to 3.33 kg/m, 0.177, and 14 Hz, respectively. These values were selected to be consistent with the conditions of the experimental stability data provided by Violette et al.

(2006). To evaluate the threshold of instability at different conditions for the flow field sub-model, three main parameters were controlled: the inlet void fraction of the mixture, the reduced flow velocity, and the pitch-to-diameter ratio. In all the simulations, the bubble size diameter at the inlet was set to a value of 0.1 mm, as discussed in (Sadek et al., 2018). For each simulation, a steady-state solution of the flow field was obtained first, then used as an initial start for the unsteady simulation.

In order to predict the fluid force coefficients required for the hybrid analytical-flow field model, fluid flow simulations were conducted with only one tube that was forced to vibrate periodically. Tube C is given a sinusoidal displacement motion (referred to afterward as “motion”) with an amplitude of $8\% D$. Three groups of simulations were conducted, each of which had a single forced frequency of 8 Hz, 12 Hz, or 16 Hz. Simultaneously, the resultant dynamic forces acting in the streamwise direction due to this motion on the surrounding tubes were monitored. Fast Fourier transform (FFT) of the resulting fluid forces was utilized to obtain their amplitudes and phase angles relative to the motion of tube C. Then, this data was employed in Eq. (4.11), (4.12) and (4.13) to obtain the stability threshold for a kernel consisting of 7 tubes (tubes C, N, NE, NW, S, SE, and SW). In comparison, for the direct flow/structure coupling model, an initial perturbation was given to one tube at the beginning of the unsteady simulation. This was done by displacing tube C upward from its original position by a distance of $8\% D$. A steady-state solution was then obtained for this position as an initial condition for the unsteady simulation. During the unsteady simulation phase, the kernel consisting of the seven monitored tubes was allowed to oscillate freely only in the streamwise direction around the neutral position. All other tubes were fixed, and their displacement signals were monitored for the stability check. This procedure was repeated at various flow velocities for each void fraction to obtain a complete stability map.

An unstructured mesh was used in the analysis, as shown in Fig. 4.2. A previous study (Sadek et al., 2018) showed that an element size of 1 mm was sufficient to capture the fluid dynamic forces acting on the tubes. In the boundary layers, 14 structured prism layers were implemented to resolve the flow gradient in this zone. These mesh attributes were chosen according to a mesh sensitivity analysis presented by (Sadek et al., 2018). In total, the current mesh element counts were 164 000, 148 000, and 141 000 for the domains representing pitch-to-diameter ratios of 1.7, 1.5, and 1.3, respectively.

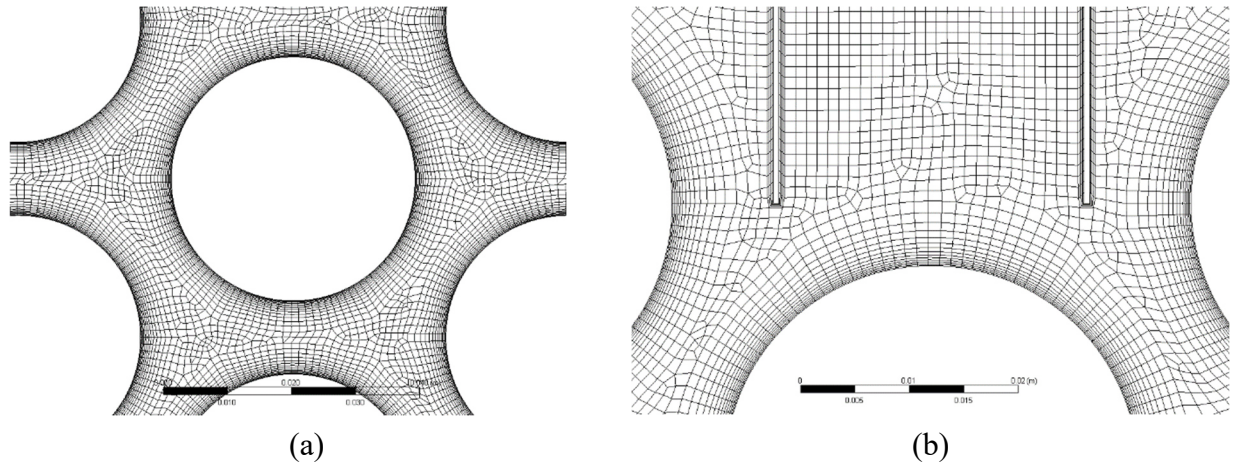


Figure 4.2: Unstructured mesh pattern for $P/D = 1.3$ domain: a) in the vicinity of tube array, b) between the tubes and the baffle plates.

4.3. Results and discussion

A sensitivity analysis was performed, comparing the developed model to the selected turbulence closure model. Figure 4.3 shows the effect of various turbulence models on the simulated fluidelastic forces acting on tubes C, N, NW, SW, and S. Four RANS turbulence models were investigated, namely: $k-\omega$, Menter's SST model, Spalart-Almaras S-A, and the Reynolds stress model. These models are widely used in the literature to model bounded flow over cylindrical structures; therefore, they were selected to investigate the accuracy of predicting fluidelastic instability forces. The $k-\omega$ is a two-equation model for the turbulence kinetic energy (k) and the specific rate of dissipation (ω). This model is best suited for shear flows with an adverse pressure gradient; however it is not adequate for free shear flow. To improve this drawback, the $k-\omega$ model was combined with the $k-\epsilon$, which is adequate for free shear flows. This was accomplished through transition functions so that the $k-\omega$ formulation was used near the wall and then switched to the $k-\epsilon$ away from the wall. The Spalart-Almaras model is a transport equation model for eddy viscosity. It was developed specifically for wall-bounded flows and can account for boundary layers that experience an adverse pressure gradient. It is used for flows over aerofoils and in turbomachinery; however, it is not adequate for use in free shear flows. All the previously discussed models were based on the Boussinesq hypothesis, which is applicable for isotropic eddy viscosity conditions in which the turbulence stress is dominated by one component of the shear stresses. They can therefore be applied for boundary layer, jet, and mixing layer flows. In comparison, the Reynolds

stress model does not implement this approach. It models each element in the Reynolds stress tensor separately. It is therefore suitable for anisotropic turbulence conditions, in which the flow experiences a high degree of swirl and rotation.

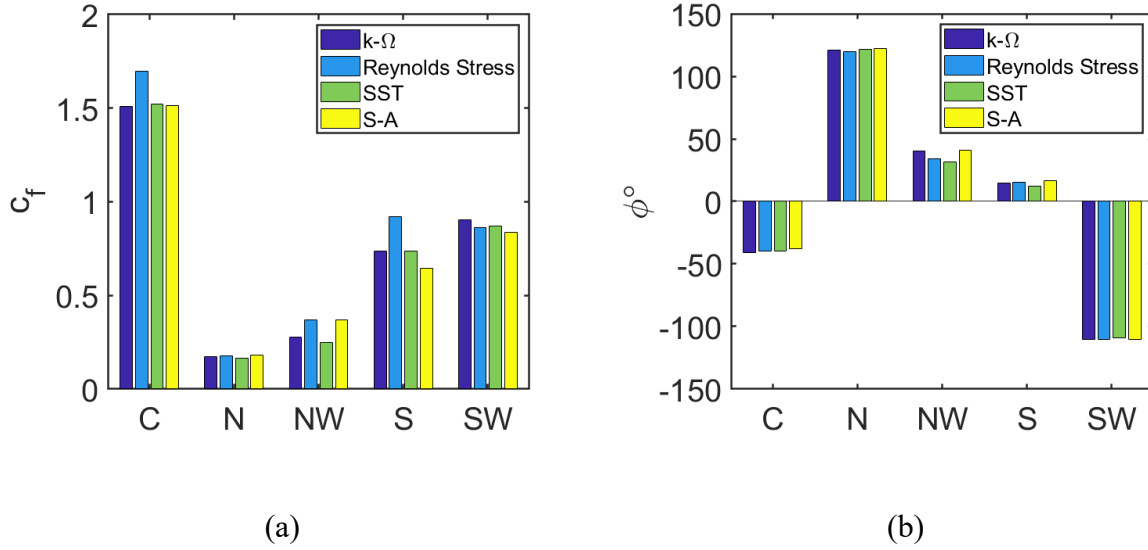


Figure 4.3: Effect of the turbulence model on the simulated fluidelastic forces relative to the motion of tube C. $P/D = 1.3$, $\alpha = 80\%$, $Ur = 10$: a) Force coefficient, b) phase angle.

A comparison was performed for $P/D = 1.3$, in which the tube bundle is closely packed and the flow channels between the tubes are narrow; therefore, very high velocity gradients exist along the cross-section of the channels. A flow condition of $Ur = 10$ and an 80% void fraction were selected, while the oscillation frequency of tube C was set to 8 Hz. Both the fluidelastic force magnitudes and the phases pertaining to the monitored tubes C, N, NW, SW, and S were used for the comparison. Tubes NE and SE were included due to the symmetry of the fluid forces. The comparison of the predicted fluid forces showed only small differences among the four models, although the Reynolds stress model may have led to a slightly higher force magnitude. This can be seen for tubes C and S; however, the simulated phase angles of the fluidelastic forces were not affected by the choice of the turbulence model. In general, the choice of the turbulence model did not significantly affect the fluidelastic forces. This conclusion supports the earlier findings by Palomar and Meskell (2018) and Hassan et al. (2010).

The validation of the developed model was conducted against the experimental data reported by Olala and Mureithi (2015). In their experiments, an actuator was used to induce a predefined motion to the central tube inside a parallel triangular tube array of a pitch-to-diameter ratio and a

tube diameter of 1.5 and 38 mm, respectively. In the current work, the same dimensions were used to facilitate a comparison. In their setup, the central tube was forced to oscillate sinusoidally in the streamwise direction with frequencies of 8, 9, 10, 11, 12, 14, and 16 Hz, and the fluidelastic forces acting on the moving and the surrounding tubes were measured for a water flow with a 60% void fraction. From these measurements, the magnitude and the phase angle of each force were obtained. In the current simulations, three different frequencies (8, 12, and 16 Hz) were utilized, which covered the frequency range of the available experimental data. Figure 4.4 shows a comparison between the numerical prediction and its experimental counterpart for tubes C and SW. The oscillation frequency did not seem to have an effect on the magnitudes of the force coefficients. Similarly, changing the frequency had little effect on the phase angle for the center tube (Fig. 4.4-b); however, a larger effect was observed for the forcing frequency in the case of the phase angle for tube SW (Fig. 4.4-d). The effect was larger as the reduced flow velocity was increased. A maximum variation in the simulated phase was observed to be within 9° of the different frequencies. When compared to the experimental values, a good agreement could be observed between the simulations and the experiments. The effect of oscillation frequency was more pronounced in the experiments than in the simulation. Olala and Mureithi (2015) reported that this effect was insignificant within the oscillation frequency range between 8 Hz and 12 Hz, as well as in the void fraction range from 0% to 80%. These were the same ranges covered by the current study. Outside these ranges there was a clear change in the phase angle trends due to the oscillation frequencies. The current simulation seems to replicate the mean of the experimental values as a function of the reduced velocity, which captures the typical variation trends of the force data with respect to the reduced velocity. This is typically observed for all force parameters. As such, implementing a single value of frequency oscillation for the developed CFD model is a reasonable representation for the fluidelastic behavior at other frequency values. The assumption here is that the fluid force coefficients were only a function of the reduced flow velocity (U/fD), which could be produced by a combination of flow velocity and frequency. This selection should not be confused with the natural frequency of the tubes defined in the structural sub-model as 14 Hz; therefore, a value of 8 Hz was selected for all the results presented in this work. This is advantageous, as simulations at higher values of reduced velocity will then require less computational resources compared to those at higher oscillation frequencies.

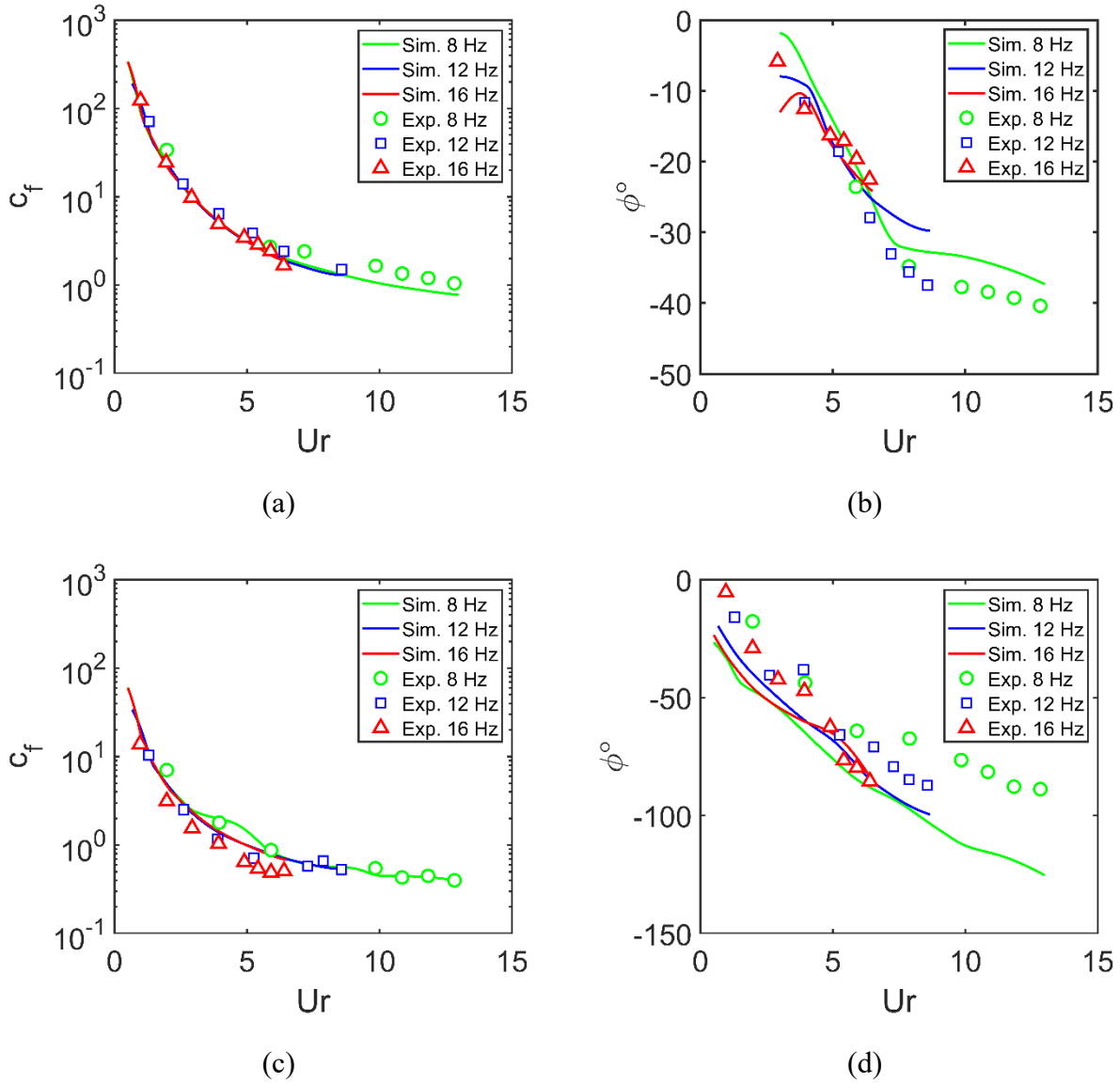


Figure 4.4: Effect of oscillation frequency on the dynamic fluidelastic forces. $P/D = 1.5$, $\alpha = 60\%$. Experimental data were extracted from (Olala & Mureithi, 2015): a,b) tube C, c,d) tube SW.

Simulations were also conducted to study the effect of void fraction on the fluidelastic forces acting on the tubes using the developed model, as shown in Fig. 4.5. The data presented are for the predicted fluidelastic forces, force coefficients and phase angles, acting on the tubes C and SW at void fractions of 20%, 40%, 60%, and 80%. Experimental data extracted from Olala and Mureithi (Olala & Mureithi, 2015) at a 60% void fraction are presented for comparison. Here, the range of reduced flow velocities was extended to 40, which exceeds the onset of streamwise FEI observed experimentally by Violette et al. (Violette et al., 2006) at a 95% void fraction for the same

geometry. It is evident that the void fraction does not have a significant effect on either the normalized force coefficient or the phase angle for a low reduced flow velocity. As well, this behavior was found in the results of the N, NE, and S tubes.

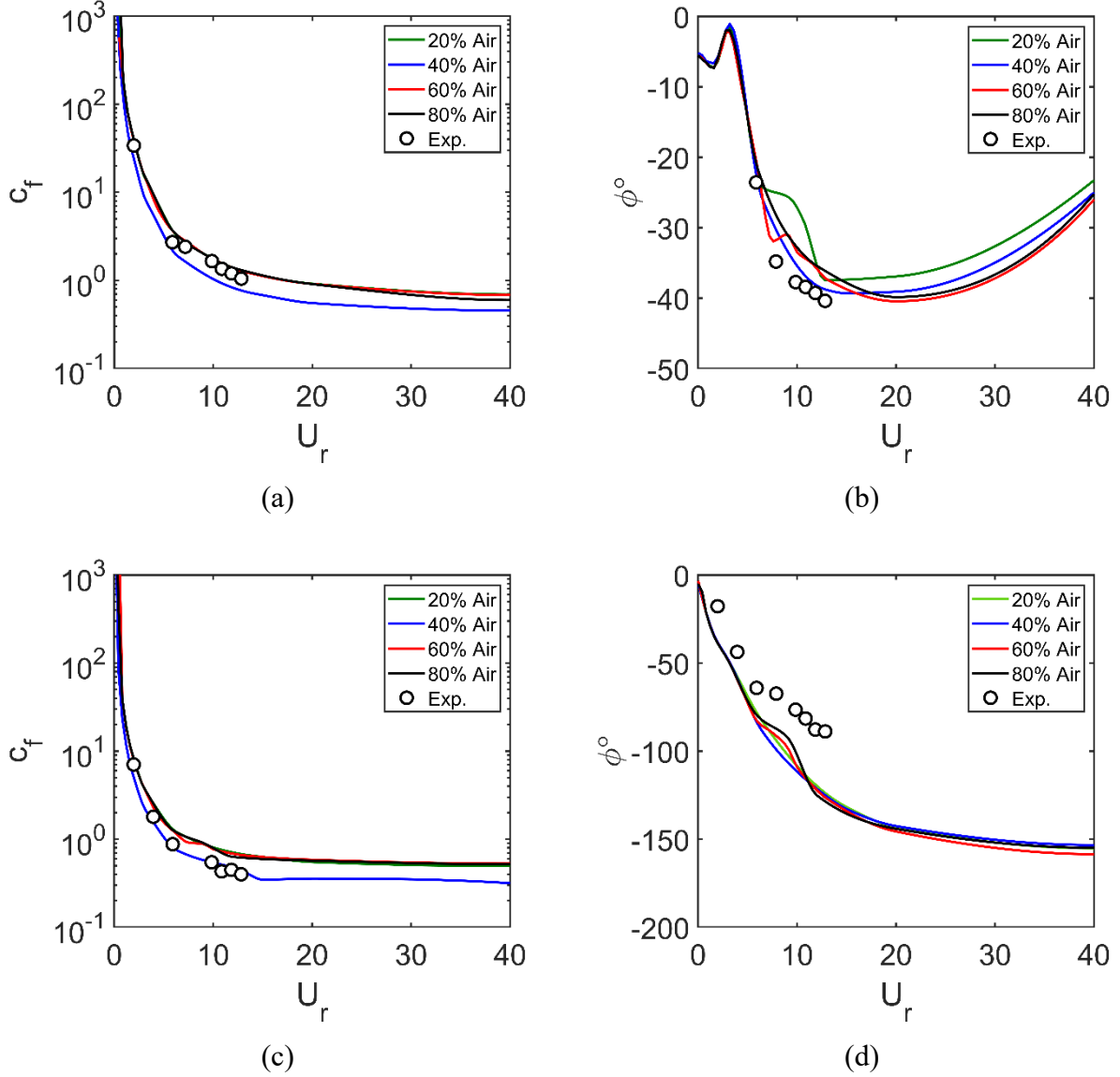


Figure 4.5: Effect of the void fraction of the fluidelastic forces and its phase from the tube motion. $P/D = 1.5$, $\alpha = 60\%$. Experimental data were extracted from (Olala & Mureithi, 2015): a,b) tube C, c,d) tube SW.

It is worth noting that there was a variation in the phase angle at a 20% and a 60% void fraction (Fig. 4.5) that occurred at a U_r value around 10. As mentioned earlier, baffle plates were introduced downstream of the last tube row to minimize the effect of the vortices. At this reduced velocity, however, some flow periodicities were observed inside the bundle, which appeared to be

anomalous. This was not understood and was observed experimentally. Such vorticities interfered with the fluidelastic force signal, causing a disturbance in the measured phase angle. The magnitude of these periodicities was, however, relatively small compared to the FEI force signal.

The above results validate the numerical model using a pitch-to-diameter ratio of 1.5. To study the effect of the pitch to diameter ratio on the streamwise stability threshold, additional simulations were conducted to cover other pitch-to-diameter ratios representing a more compact bundle of $P/D = 1.3$ and a wider one of $P/D = 1.7$. Figures 4.6 and 4.7 provide the resultant FEI forces in the streamwise direction acting on a kernel of tubes for pitch-to-diameter ratios of 1.7 and 1.3, respectively. Due to the symmetry, the presented data are for the left half of the kernel denoted by tubes C, N, NW, SW, and S. FEI forces on the NE and SE tubes were not presented as they were identical to that of NW and SW, respectively. Moreover, the effect of the void fraction was simulated as well to investigate the deviation from the bubbly regime in the flow channels at different spacing of the tubes.

The direct inspection of forces is not a very comprehensive way to analyze the force coefficients and phase angle dependencies on reduced velocity since the streamwise FEI is a stiffness-controlled phenomenon. An inspection of each force individually will therefore not provide a reliable indicator for streamwise FEI, but the interactions between all motion-induced fluidelastic forces are what affects the instability threshold. The latter can be analyzed by inspecting the eigenvalues for the system matrix in Eq. (4.13), which is presented later in this section; however, two aspects can be inspected directly to provide useful indications. First, the sign of the phase angle at the central tube indicated the nature of the instability. Figure 4.6-b shows a negative value for the phase angle, indicating that the fluidelastic force lags behind the motion of the tube. This means that the streamwise FEI predicted through the current data cannot be a damping-controlled mechanism. Such results are in agreement with the findings of Nakamura et al. (2014). The second is the differences between the trends in the force magnitudes and the phase angles with respect to the reduced velocity at different pitch-to-diameter ratios, which is discussed in detail in Fig. 4.8.

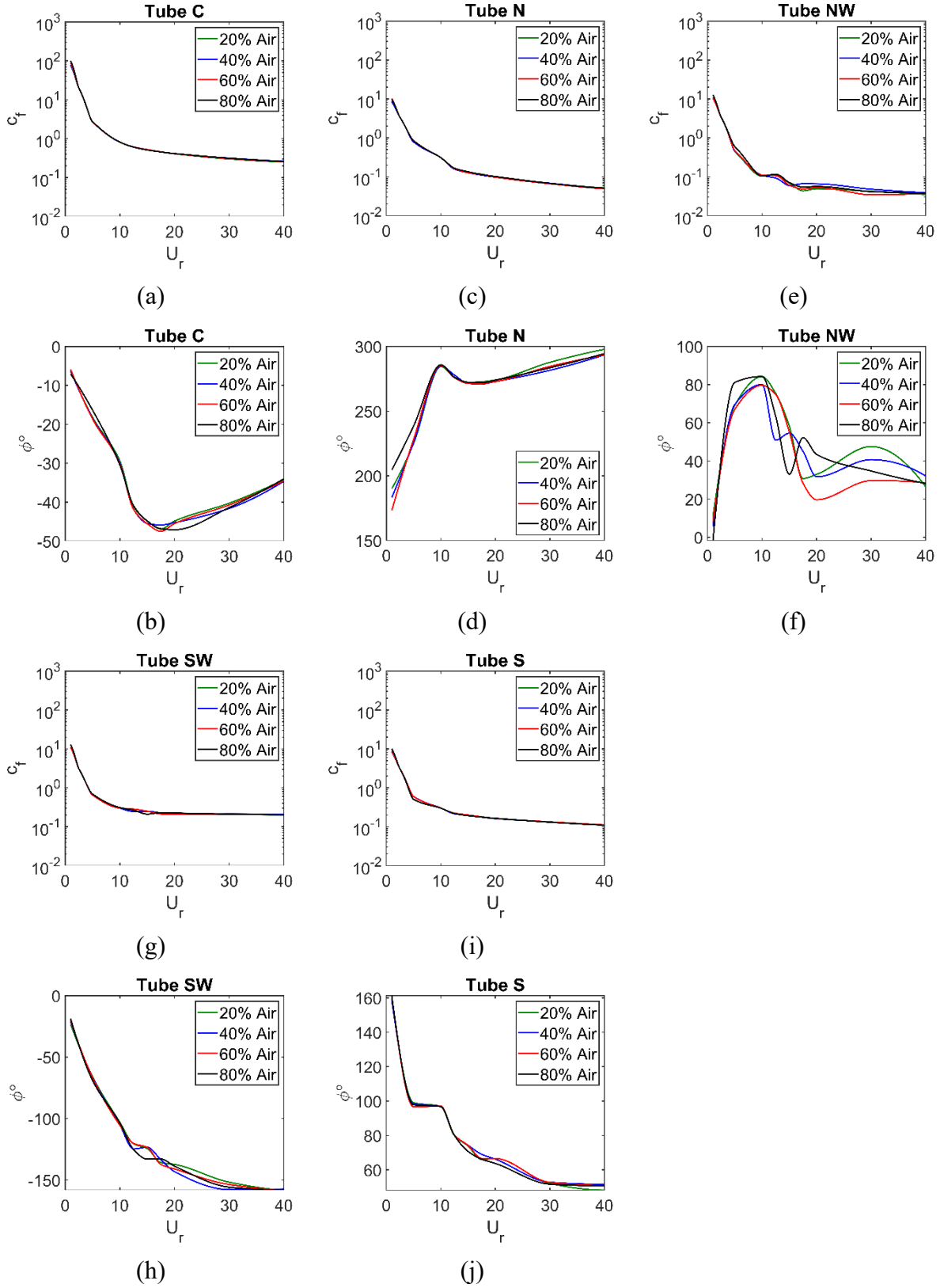


Figure 4.6: Fluidelastic forces and phase angles on Tube C at different void fractions. $P/D=1.7$: a, b) tube C; c, d) tube N; e, f) tube NW; g, h) tube SW; i, j) tube S.

Figure 4.6 shows the predicted force coefficients for the $P/D = 1.7$ geometry. The effect of void fraction is still very minimal for both the force coefficients and the phase angles for all the tubes. Only two tubes, N and NW, which are on the downstream side of the kernel, show some dependency on the void fraction for the phase angles. For tube N, this dependency occurs at low reduced flow velocities (< 10). For reduced flow velocities higher than 15, some variations exist in the results of the various void fractions for the NW and NE tubes (Fig. 4.6-f). The same dependency on void fraction was also observed for $P/D = 1.3$ for the same NW and NE tubes in Fig. 4.7 at a reduced velocity of around 17.

The effect of pitch-to-diameter ratio is illustrated more clearly in Fig. 4.8. Fluidelastic force coefficients and phases were compared for tubes C and SW for three pitch-to-diameter ratios of 1.7, 1.5, and 1.3. A void fraction of 60% was selected to present the basic trend of the results. It is worth noting that the calculation of the fluidelastic force coefficients required normalization by the amplitude of the imposed sinusoidal motion [Eq. (4.12)]. However, this amplitude should be varied according to the pitch-to-diameter ratio to maintain the same blockage ratio of the gap when the tube oscillates (i.e. the ratio between oscillation amplitude and the tube-to-tube gap). For all the studied P/D values, this ratio was maintained at 15.8%. By inspecting the magnitudes of the force coefficients in Fig. 4.8-a and Fig. 4.8-b, it was noted that decreasing the pitch-to-diameter ratio resulted in an increase in the fluid force coefficient. This was observed for tubes C and SW, as well as the other tubes, which indicates a weaker fluidelastic coupling between the tubes at a large pitch-to-diameter ratio due to the larger spaces between the tubes in the bundle. However, as the spacing between tubes gets smaller, the FEI coupling force coefficients tend to reach an asymptotic value as in the cases of $P/D = 1.3$ and 1.5. Furthermore, the phase angle of tube SW (and SE) in Fig. 4.8-d is insensitive to the pitch-to-diameter ratio. This was also true for tube S. In comparison, for the other tubes (C, N, NE, and NW) there are differences in the phase angle values with respect to the pitch-to-diameter ratio. For tube C, a steep reduction in the phase angle was observed for $P/D = 1.3$ until a minimum value of -42° at $U_r = 10$; then the phase decreased steadily with a further increase in the reduced velocity. The same trend was also observed for $P/D = 1.7$ but the minimum phase angle occurred at higher reduced velocity of 17.5 at a value of -48° . This had an effect on the fluid stiffness. Considering Eq. (4.11-b) and examining the fluid added stiffnesses introduced at tubes N and NW ($\beta''_{N,C}$ and $\beta''_{NW,C}$), it can be seen that they were smaller in the $P/D = 1.7$ than in $P/D = 1.3$.

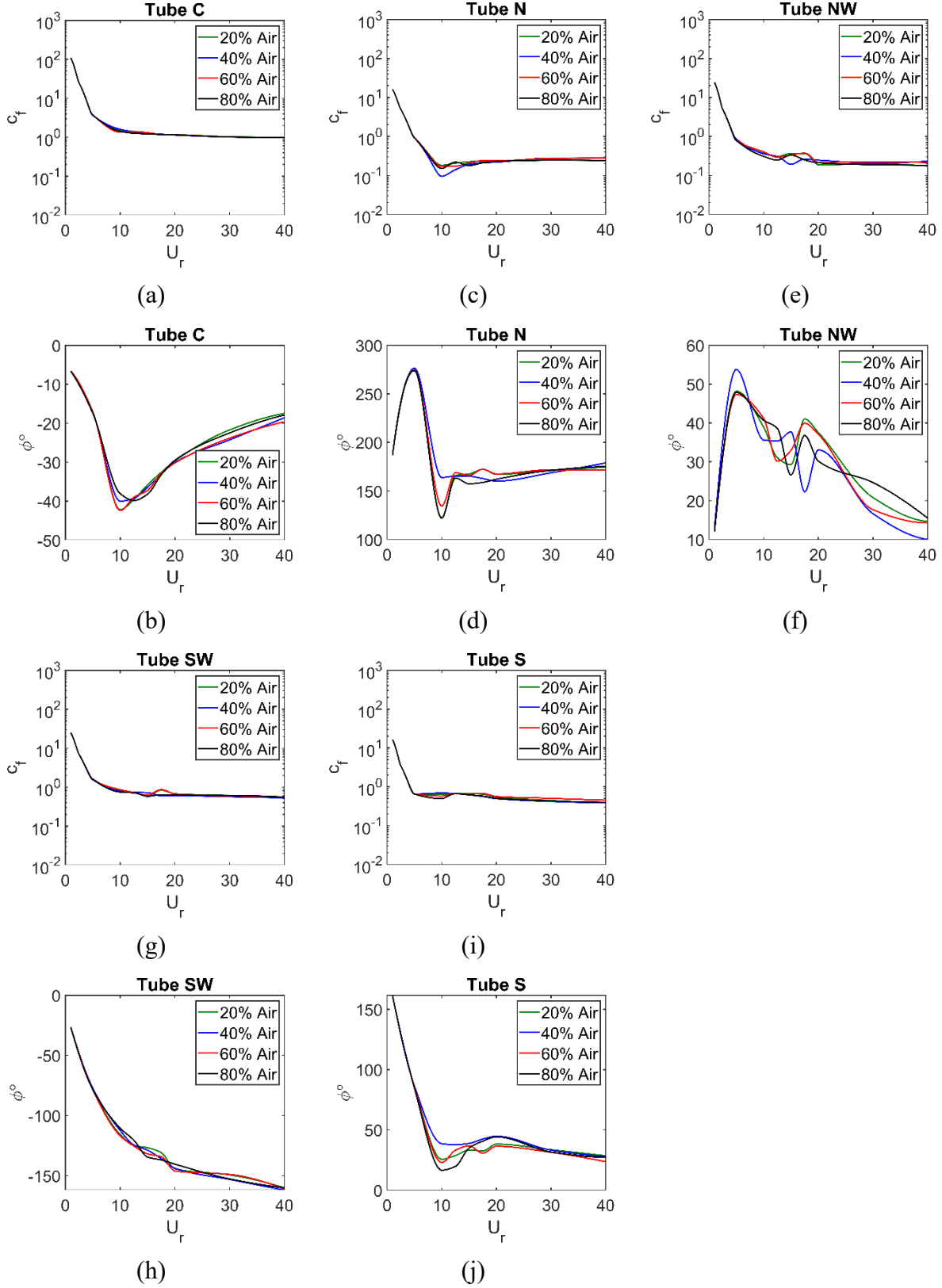


Figure 4.7: Fluidelastic forces and phase angles on Tube C at different void fractions. $P/D=1.3$: a, b) tube C; c, d) tube N; e, f) tube NW; g, h) tube SW; i, j) tube S.

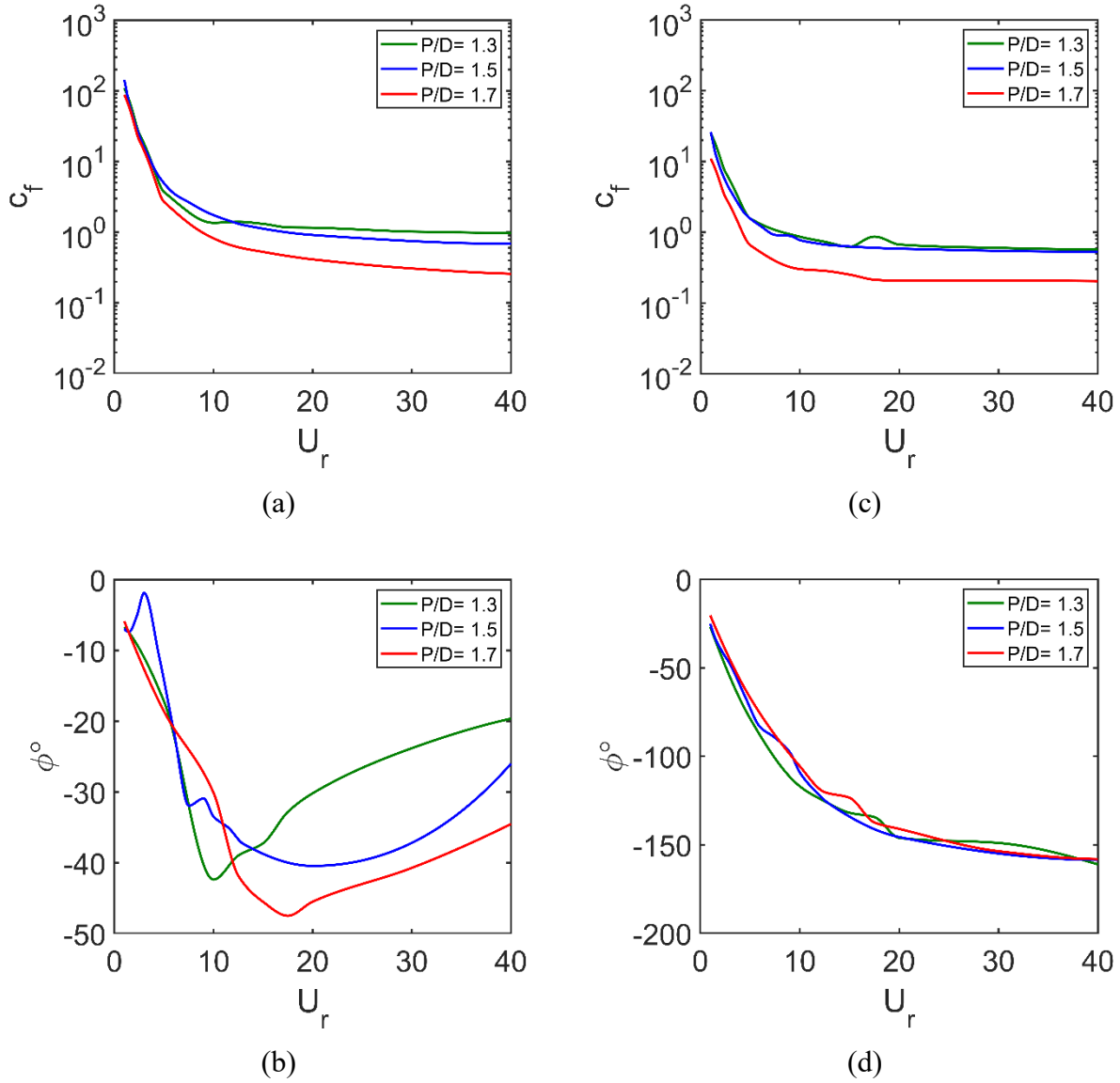


Figure 4.8: Effect of P/D ratio on fluidelastic force magnitude and phase angle at 60% air: a,b) tube C; c,d) tube SW.

Although the general effect of reducing the pitch-to-diameter is to increase the FEI stiffness coupling, it is rather complex and not solely due to one parameter of the FEI force. For a reduction in the pitch-to-diameter ratio from 1.7 to 1.5, the main contributor to strengthening the stiffness coupling mechanism was the increase of the coupling force magnitudes between the tubes. When the pitch-to-diameter ratio was reduced further to 1.3, the contribution of the phase angle became dominant in the strengthening process.

Flow structure inside of tube bundles with different spacing ratios is presented in Fig. 4.9 to shed some light on the flow behavior causing the different phase angle trends. Figure 4.9 illustrates the velocity field during one cycle of the oscillation of tube C at four instants of the cycle corresponding to the normalized times T^* (time/period) of 0, 0.25, 0.5, and 0.75, in which the flow reduced velocity was fixed at $U_r = 10$. Flow streamlines are overlaid on the figure to emphasize the location of the flow channel around tube C. For the $P/D = 1.3$ (Fig. 4.9-a, -b, -c, and -d) it is clear that the narrow spacing between the tubes gives a good definition of the flow channels, with a minimal flow leaving the flow channels and circulating in the tubes' wake. For the other pitch-to-diameter ratios (Fig. 4.9-e, -f, -g, -h for $P/D = 1.5$ and Fig. 4.9-i, -j, -k, -l for $P/D = 1.7$), it is clear that the flow channels become less defined around the oscillating tubes with more intermittent flow passing through the wake of the tube to the neighboring flow channel. This is very evident in Fig. 4.9-i when a portion of the flow switches from the right channel to the left channel upstream of tube C as tube C is moving upward, and in Fig. 4.9-k when another portion of the flow is passing from the left channel to the right channel upstream of tube C when it moves downward.

The streamwise FEI stability threshold predictions in terms of the mass-damping parameters were obtained from both hybrid analytical-flow field and direct flow/structure coupling models and are presented in Fig. 4.9 and Fig. 4.10. Also presented in these figures are the experimental data provided by Violette et al. (2006) for a flexible kernel in a parallel triangular tube array with a pitch-to-diameter ratio of 1.5. From Fig. 4.9, the predicted stability map for $P/D = 1.5$ with both models agrees well with the corresponding experimentally measured stability threshold. In contrast, as seen in Fig. 4.10, the effect of the pitch-to-diameter ratio on the critical flow velocity is more pronounced. The stability threshold obtained by the hybrid model shows that increasing the P/D ratio results in an increase in the stability threshold. A similar effect for the P/D ratio has been reported in the literature for single phase flows (Hassan & Weaver, 2017a; Nakamura et al., 2014). Moreover, the results obtained by the direct flow/structure coupling model confirmed the same P/D effect on the stability threshold and agreed well with the predictions obtained by the hybrid model. The difference in the predictions of the two models becomes smaller as the mass-damping parameter or the void fraction increases. The predictions of the direct flow/structure coupling model are consistently higher than those of the hybrid model.

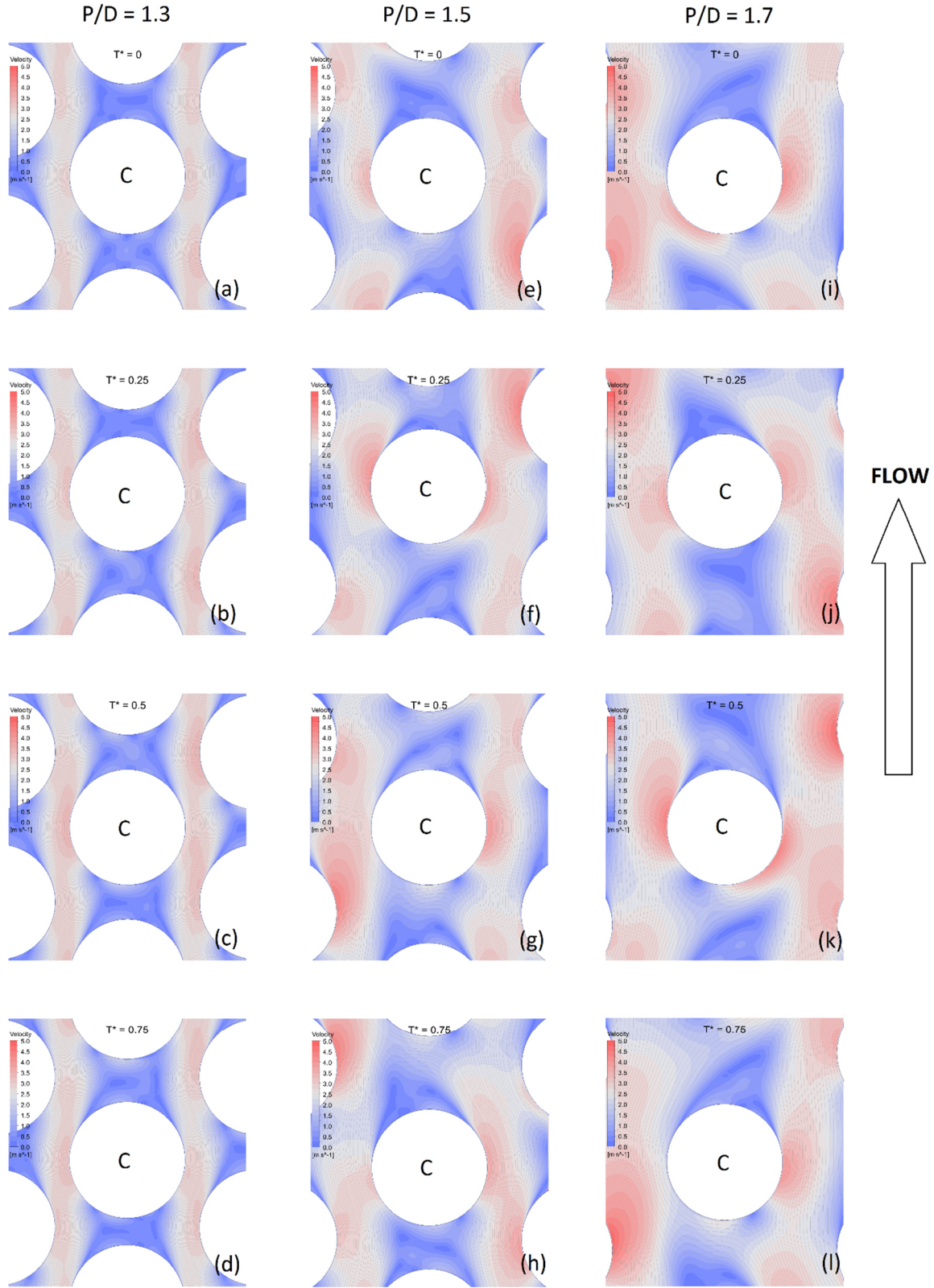


Figure 4.9: Velocity and streamlines of flow in tube bundles with $P/D = 1.3$ (a, b, c, d), 1.5 (e, f, g, h), and 1.7 (i, j, k, l) at different instants in the cycle. $\alpha = 80\%$, $U_r = 10$.

As mentioned earlier, the fluid force coefficient and phase information are utilized in the hybrid model. The greatest variations in the force coefficients are observed at low reduced velocities ($U_r < 10$). At flow velocities greater than 10, fluid force coefficients are constant. For the purpose of simulating tube dynamics, the elements of the system matrices were determined by curve fitting these coefficients. This fluid force calculation procedure may have contributed to the difference in the predictions.

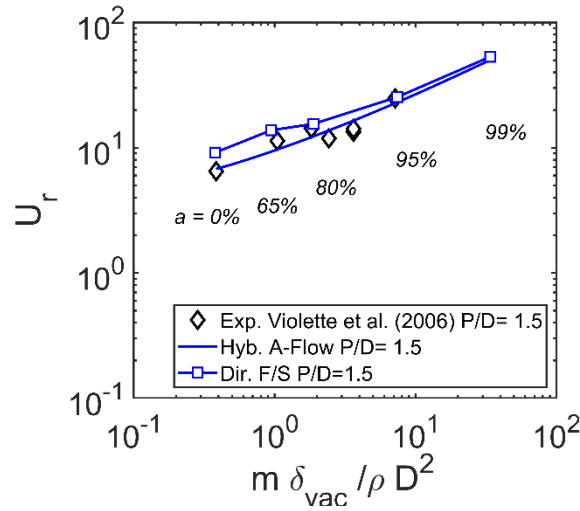


Figure 4.10: Streamwise stability map and validation with experimental data for $P/D = 1.5$.

A sample of the displacement time trace obtained for the motion of the flexible tubes is provided in Fig. 4.12. These time traces are obtained from the direct flow/structure coupling model at the onset of instability for the $P/D = 1.5$ array and at 80% void fraction. In these simulations, tube C was given an initial displacement and the response of all the tubes were recorded. All tubes showed an unstable response with an increase in the amplitude over time. The growth in the amplitude was more pronounced in the middle column formed by tubes N, C, and S. At the onset of instability, all the tubes vibrated together at the same frequency forming a distinctive mode shape.

The mode shape and the time lag between the motions of the seven tubes in the kernel were also investigated at the onset of instability for an 80% void fraction. By taking the motion of tube C as a reference, the phase angles during one cycle of the motion of each tube were extracted. This was done through inspecting the eigenvector that corresponded to the unstable eigenvalue for the coupling matrix in Eq. (4.14-b) for the hybrid analytical-flow field model.

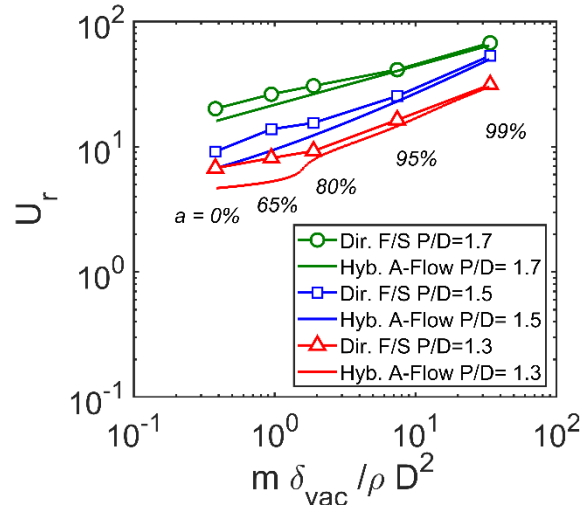


Figure 4.11: Streamwise stability map and the effect of pitch-to-diameter ratio.

For the direct flow/structure model, the time signals shown in Fig. 4.12 for the motion of each tube were processed via FFT, and the motion phase angles were obtained. Table 4.1 summarizes the comparison between the phase angles obtained from these two coupling models and their experimental counterpart, which was provided by Violette et al. (2006). The hybrid analytical-flow field model was able to capture the same mode shape with a sufficient level of accuracy with a maximum error of 20% for the SW tube while the error in the prediction for all the other tubes fell within a 10% margin. As well, the direct flow/structure model predicted the values within a maximum error of 15% for the S tube. In contrast, predictions of the phase angles for tubes SW and SE showed a better accuracy with this model compared to the hybrid model.

Table 4.1: Phase angle of the kernel mode shape. Experiments from Violette et al. (Violette et al., 2006), $\alpha = 80\%$, at the onset of instability.

	C	N	NW	SW	S	SE	NE
Experimental (Violette et al., 2006)	Reference	107°	-128°	114°	-90°	128°	-140°
Hybrid	Reference	97.6°	-131°	137.9°	-96.7°	138.5°	-133°
Direct F/S	Reference	118.3°	-134.9°	122.3°	-104.3°	120.4°	-133.8°

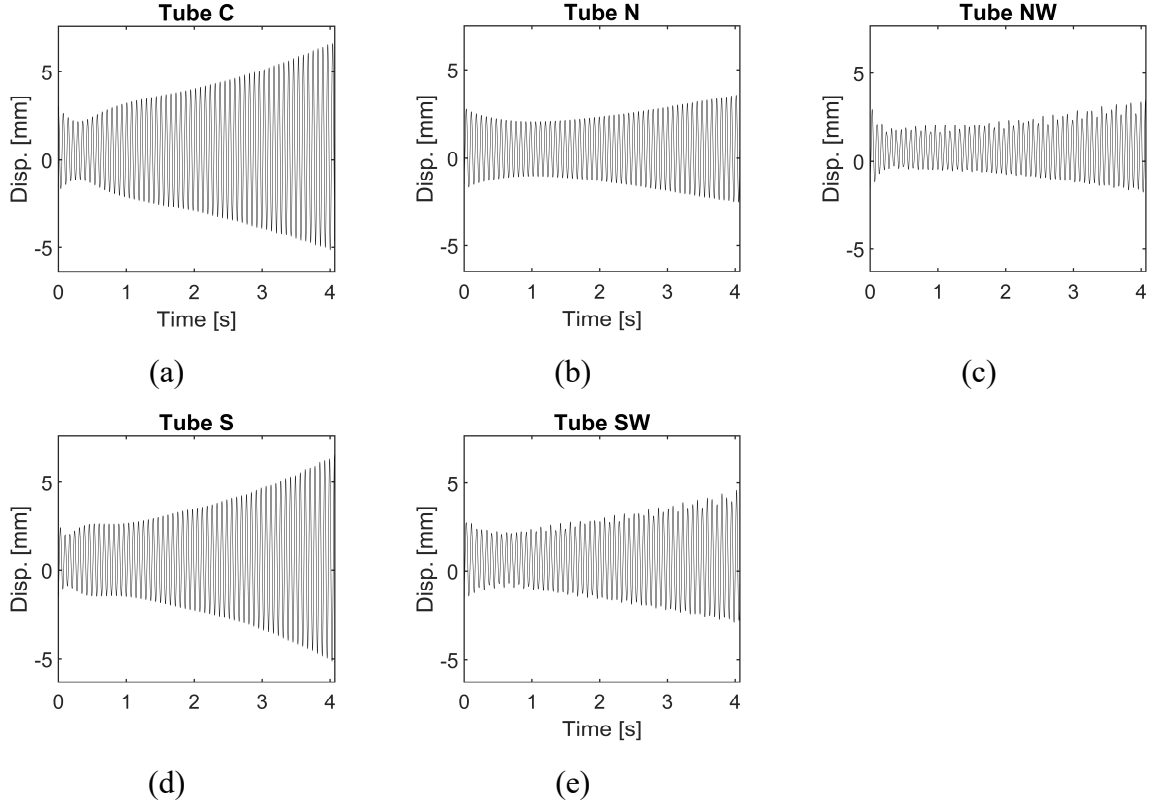


Figure 4.12: Time signals for tubes C, N, NW, SW, and S obtained from the direct flow/structure coupling model at a streamwise FEI. $P/D = 1.5$, $\alpha = 80\%$.

4.4. Conclusion

This work presented a numerical model to simulate the streamwise FEI in parallel triangular tube bundles. The validity of the model was examined for its ability to simulate the streamwise FEI for a pitch-to-diameter ratio of 1.5 by first comparing the simulated FEI forces with the available experimentally measured forces in the literature (Olala & Mureithi, 2015). The second validation step was carried out by examining the predicted stability threshold against the experimental stability data adopted from Violette et al. (2006) at different void fractions. Finally, the predicted mode shape for the oscillating tubes at the onset of instability and an 80% void fraction was compared with the experimental counterpart from Violette et al. (2006). For all aforementioned steps, the model showed a consistent agreement with experimental data, which provided confidence that the developed model is able to capture the major physical aspects of streamwise FEI.

The effect of changing the pitch-to-diameter ratio on the onset of streamwise FEI was investigated by considering three pitch-to-diameter values of 1.3, 1.5, and 1.7. It was found that an increase in the spacing between the tubes led to an increase in the stability threshold. However, the mechanism behind this is complex as a combination of variations in the force coefficient magnitude and the phase angles are responsible for the effect of the pitch-to-diameter ratio.

Chapter 5. The prediction of fluidelastic forces in triangular tube bundles subjected to a two-phase flow: The effect of the flow approach angle

Complete citation

Sadek, O., Mohany, A., & Hassan, M. (2021). The prediction of fluidelastic forces in triangular tube bundles subjected to a two-phase flow: The effect of the flow approach angle. Submitted to the *Journal of Fluids and Structures*.

Author's contribution

O. Sadek: Conceptualization, Methodology, Software, Data curation, Writing- Original draft preparation.

A. Mohany: Supervision, Methodology, Writing- Reviewing and Editing, Resources, Funding acquisition.

M. Hassan: Supervision, Methodology, Writing- Reviewing and Editing, Visualization.

Abstract

The U-bend region in a typical steam generator is characterized by two-phase flow conditions and susceptible to damage due to fluidelastic instability excitation. To prevent such a destructive fluid-structure mechanism, numerous experimental and numerical works have been done to investigate, understand, and devise techniques to mitigate it. The effect of the flow approach angle on fluidelastic instability remains one of the topics which has not been fully resolved. This work aims to utilize flow numerical modeling techniques to gain an understanding of such an effect in a two-phase air-water flow. Various flow approach angles ranging from normal to parallel triangular arrays were investigated for various void fractions ranging from water to air flows. The results obtained revealed that the effect of a homogeneous air void fraction is very critical at very high values (99% and above). Moreover, at any intermediate flow approach angle between a normal and a parallel triangular array, the flow inside the array carries features of both normal and parallel

triangular flow patterns. Based on this, a new FEI force-approach angle, semi analytical model is proposed to calculate the fluidelastic forces at any flow approach angle. The data obtained from this model were validated against information extracted from flow simulations and showed a good agreement.

Keywords:

Fluidelastic instability, two-phase flow, approach angle, U-bend, fluidelastic force.

5.1. Introduction

Fluidelastic instability (FEI) is a devastating mechanism which can severely affect the integrity of steam generators. It often causes catastrophic damage in a short time span. This has led to an extensive effort to study this mechanism, to develop predictive models for the onset of stability, and to refine design guidelines to mitigate its occurrence. Generally, four classes of models have been developed for such predictions: the quasi-static model (Connors, 1970), the quasi-steady model (Price & Païdoussis, 1983, 1984), the unsteady models (Chen, 1983; Tanaka & Takahara, 1981), and the semi-analytical model (Lever & Weaver, 1982; Yetisir & Weaver, 1993).

Some of these models have been successfully implemented to predict both transverse and streamwise instabilities. The first points to the tube oscillation in a direction perpendicular to the flow direction while the latter refers to oscillations in a direction parallel to the flow. For an axisymmetric tube, the loss of stability occurs first in the transverse direction. As such, transverse FEI has been investigated extensively for the standard tube array geometries, namely normal and parallel triangular arrays, and normal and rotated square arrays. Several empirical guidelines have been established to predict the stability threshold. Weaver and Fitzpatrick (1988) presented a design guideline that included the effect of the array geometry, so that given the mass-damping parameter and array type, one could predict the stability threshold. In a triangular array, when the flow is perpendicular to one of the sides of the triangle, the array is called a normal triangle array. In contrast, when the flow is parallel to one of the sides of the triangle, the array is called a parallel triangular array. However, in heat exchangers, the flow direction does not often match one of these standard configurations and it often approaches the array at an angle (Weaver & Yeung, 1983).

This raises a fundamental question about the effect of the approach angle on the FEI mechanism. Current guidelines do not include this effect. A few experimental works in the literature have attempted to address this problem; however, none of these attempts has considered two-phase flow conditions. In a series of published works, Weaver and Yeung (1983, 1983) investigated the effect of the flow approach angle on FEI for square and triangular arrays in a water tunnel. These studies were carried out by rotating the tube array relative to the flow direction. This change in the approach angle caused an abrupt drop in the stability threshold when the array was rotated 8° from the normal triangular orientation. However, the transition was generally gradual for the square tube array. Recently, Elhelaly et al. (2020) have investigated the flow approach angle effect for a loosely-supported single flexible tube in square and triangular arrays in a wind tunnel. On the whole, these findings were in agreement with those of Weaver and Yeung (1983, 1983), however; it was difficult to define the critical velocities at some orientations.

Numerous valuable experimental studies have investigated the FEI threshold for two-phase flows (Axisa et al., 1985; Feenstra et al., 1995, 2003; Janzen et al., 2005; Mohany et al., 2012; Pettigrew et al., 1989; Pettigrew et al., 2002; Zhang et al., 2007). In these studies, air-water, liquid-vapor Freon, and water-steam were utilized as the two-phase mixtures, which resulted in a series of threshold instability maps for two-phase flows. Nevertheless, such experiments can be very complex and costly to operate. Therefore, with recent advances in computational techniques for fluid and structural mechanics, the numerical approach has become very attractive. In the past decade many studies have utilized this approach for both single and two-phase flows. Several studies utilized coupled computational fluid dynamics (CFD)/structural codes to directly simulate the flow-induced vibration of tube arrays (de Pedro et al., 2016; Hassan & Mohany, 2012, 2016). A more pragmatic approach involved using CFD to extract the necessary parameters for any of the well-established FEI models to predict the threshold of instability (Anderson et al., 2014; de Pedro & Meskell, 2018; El Bouzidi & Hassan, 2015; Hassan et al., 2010). The predictions were often in good agreement with the experimental results and focused on the FEI threshold for standard arrays. However, no numerical investigations have looked into the effect of the flow approach angle of the FEI threshold despite the versatility of CFD, which can provide more insight and information into understanding this effect.

This work aims to model the flow inside a triangular tube array to investigate how the flow approach angle affects the FEI stability threshold. The focus is on two-phase air-water mixture flow conditions.

5.2. Model Description

The model utilized here is based on the work presented and validated by Sadek et al. (Sadek et al., 2018, 2020) for the parallel triangular tube array. In the current work, the model has been extended to include a normal triangular array and three other intermediate arrays with flow approach angles of 7.5° , 15° , and 25° measured from the normal triangular orientation (the flow is normal to the base of the triangle). To avoid confusion in visualizing the angles of the flow approach, the orientation angle of a triangular array will be used. As shown in Fig. 5.1, the normal triangular array has a 30° orientation angle while the parallel triangular array has a 60° orientation angle. Table 5.1 summarizes the conversion from one angle definition to the other.

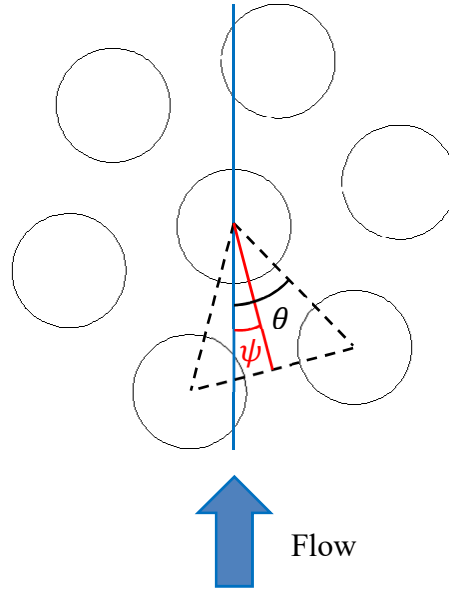


Figure 5.1: Depiction of the approach angle (ψ) and the orientation angle (θ) of the flow.

Table 5.1: Conversion between the approach angle and the orientation angle of the flow.

Approach angle (ψ)	0°	7.5°	15°	25°	30°
Orientation angle (θ)	30°	37.5°	45°	55°	60°

Several two-dimensional flow domains were developed in the current work for transverse and streamwise FEI. Each domain represents an orientation angle from the array. Full sets of fluid forces, phase angles, and flow channel calculations are presented for 30° (normal triangle), 37.5° , 45° , 55° , and 60° (parallel triangle). The arrays are composed of a number of tubes that are 38-mm in diameter (D) and are arranged in a triangular layout of a 1.5 pitch-to-diameter ratio (P/D). All domains contain these sections: upstream, array, and downstream. The length of the upstream section is $5.5 D$ and extends from the inlet boundary at the bottom of domain until the leading stagnation point of the bottom-most tube. In the array section, the number of tubes depends on the orientation angle, as seen in Fig. 5.2. The width of the domain is varied to fit the orientation angle of each array and fully contain the kernel that is being monitored. The downstream section also has a length of $5.5 D$ and is composed of channels made from baffle plates that reduce the flow periodicity downstream of the tubes. These plates were useful in obtaining a clearer time-signal of the lift and the drag forces (de Pedro et al., 2016; de Pedro & Meskell, 2018; Sadek et al., 2020).

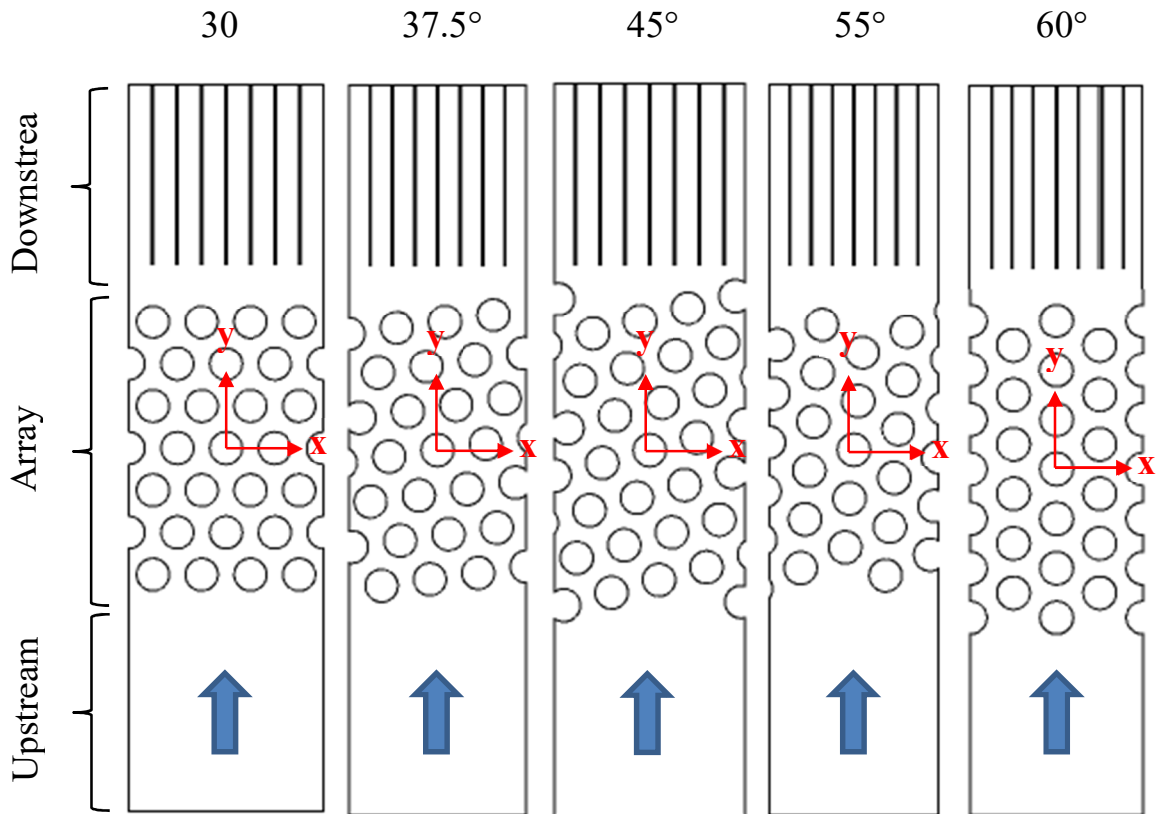


Figure 5.2: CFD domains for the orientation angles of different tube arrays.

Unstructured quadrilateral meshing elements were implemented in the domains that were being studied. The length of the average mesh element was 1 mm. Fourteen prism layers were incorporated at the solid surfaces. Reynolds-averaged Navier-Stokes equations (RANS) were utilized to solve for the fluid dynamics. The Spalart-Allmaras (1992b) turbulence model was selected for the terms of the Reynolds stresses in RANS. Moreover, a mixture model was adopted to model the two-phase nature of the flow. In such a model, the volume-based weighted average mixture velocity field that represents the velocity field and the RANS equations becomes:

$$\frac{\partial}{\partial t}(\rho_m) + \nabla \cdot (\rho_m \mathbf{u}_m) = 0 \quad (5.1)$$

$$\begin{aligned} & \frac{\partial}{\partial t}(\rho_m \mathbf{u}_m) + (\mathbf{u}_m \cdot \nabla)(\rho_m \mathbf{u}_m) \\ &= \rho_m \mathbf{g} - \nabla P + \nabla \cdot (\mu_m (\nabla \mathbf{u}_m + (\nabla \mathbf{u}_m)^T)) + \nabla \cdot \left(\sum_{k=1}^n a_k \rho_k \mathbf{u}_{dr,k} \mathbf{u}_{dr,k} \right) \end{aligned} \quad (5.2)$$

where \mathbf{u}_m , $\mathbf{u}_{dr,k}$, \mathbf{g} , P , and a_k are the mixture velocity, the drift flux velocity of phase k (the difference between the phase k velocity and the mixture velocity), the gravity, the static pressure, and the volumetric void fraction of phase k , respectively. ρ_m and μ_m are the average density and the dynamic viscosity of the mixture. The velocity and density of the mixture are related to the void fraction such that:

$$\rho_m = \sum_{k=1}^n a_k \rho_k \quad (5.3)$$

$$\mathbf{u}_m = \frac{\sum_{k=1}^n a_k \rho_k \mathbf{u}_k}{\rho_m} \quad (5.4)$$

In the original development of the mixture model, Ishii and Zuber (1979) proposed Eq. (5.5) for the dynamic viscosity:

$$\mu_m = \mu_c \left(1 - \frac{a_p}{a_{p,max}} \right)^{-2.5 a_{p,max} \frac{\mu_p + 0.4 \mu_c}{\mu_p + \mu_c}} \quad (5.5)$$

where subscripts m , p and c refer to the mixture, the particulate (dispersed) and the continuous phases, respectively. $a_{p,max}$ is the maximum packing factor of the particulate phase, and in the case of fluids, it is equal to unity. This form is valid if one of the fluid phases can be distinguished by droplets or bubbles; however, at intermediate void fractions, this ability is limited when the flow is intermittent. This work uses a definition of the volume-based weighted average for calculating the dynamic viscosity of the mixture. This is analogous to the density of the mixture.

$$\mu_m = \sum_{k=1}^n a_k \mu_k \quad (5.6)$$

To achieve a closed system of two-phase flow modeling equations, another two transport differential equations are solved for the void fraction and the interfacial area concentration parameters. This is used to predict the distribution of the air-water phases inside the domain. These equations were used exclusively for the air phase since the focus of this study is a binary water-air mixture.

A detailed description of the fluid model, the mesh, and the sensitivity analyses are found in Sadek et al., (2018, 2020) (as described in chapters 3 and 4). The sensitivity analyses were based on the parallel triangular orientation.

5.2.1. Instability analysis

The interaction between the flow and the structure of the tubes is presented in the form of flow influence effects. These are introduced as added mass, damping and stiffness parameters; thus, the flow effect becomes analogous to classical mechanical vibration elements, as shown in Fig. 5.3.

For an N -DOF system, the fluid forces can be expressed as:

$$\{F_i\} = [M_a]\{\ddot{z}_i\} + [C_a]\{\dot{z}_i\} + [K_a]\{z_i\} \quad (5.7)$$

where $\{F_i\}$ is a $2N$ vector that contains N transverse and N streamwise forces. $[M_a]$, $[C_a]$ and $[K_a]$ are the flow added mass, damping, and stiffness matrices, respectively. $\{\ddot{z}_i\}$, $\{\dot{z}_i\}$, and $\{z_i\}$ are the $2N$ vectors, which contain the tube acceleration, the velocity, and the displacement in the transverse and streamwise directions, respectively. The fluid added mass, damping, and stiffness can be represented as follows:

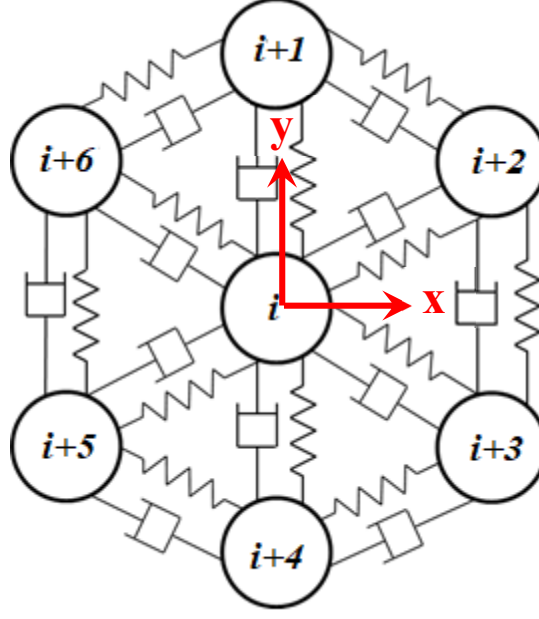


Figure 5.3: Analogy of fluid added mass, damping, and stiffness elements to a classical mechanical vibration system.

$$M_{a,ij} = -\frac{\pi\rho_m D^2}{4} \alpha''_{ij} \quad (5.8-a)$$

$$C_{a,ij} = \frac{\rho_m U_g^2}{\omega} \alpha'_{ij} \quad (5.8-b)$$

$$K_{a,ij} = \rho_m U_g^2 \alpha_{ij} \quad (5.8-c)$$

where α''_{ij} , α'_{ij} , α_{ij} are the added-mass coefficients, the added fluid damping coefficients, and the added fluid stiffness coefficients, respectively, while ω is the angular frequency of the tube oscillation. These coefficients are identical to those proposed by Chen (1987) and are extracted from the numerical flow dynamic simulations. The flow's mean velocity in the gap (channel) within the tube bundle U_g is defined as:

$$U_g = U_\infty \frac{P/D}{P/D - 1} \quad (5.9)$$

If a tube j is given a prescribed harmonic motion at a frequency f and amplitude A , a harmonic dynamic force results and will act on tube i at the same frequency with an amplitude F_{ij} and a

phase angle ϕ_{ij} , i.e. a time lead/lag difference. The amplitude is often presented in its non-dimensional force coefficient $c_{f,ij}$ as presented in Eq. (5.10):

$$c_{f,ij} = \frac{F_{ij}}{\frac{1}{2} \rho_m U_g^2 A} \quad (5.10)$$

The flow-added coefficients in Eqs. (5.8a), (5.8b), and (5.8c) are related to such dynamic forces as:

$$\alpha_{ij} = \frac{1}{2} c_{f,ij} \cos(\phi_{ij}) \Big|_{U_r=0} \quad (5.11-a)$$

$$\alpha'_{ij} = \frac{1}{2} c_{f,ij} \sin(\phi_{ij}) \quad (5.11-b)$$

$$\alpha''_{ij} = \frac{1}{2} c_{f,ij} \cos(\phi_{ij}) - \frac{\pi^3}{U_r^2} \alpha_{ij} \quad (5.11-c)$$

Moreover, the flow gap velocity is also reduced to its non-dimensional reduced velocity U_r as in Eq. (5.12). In general, the flow dynamic forces are functions of the reduced velocity U_r . Therefore, all added damping and stiffness parameters are functions of U_r except the added mass parameters, which are obtained at a quiescent flow ($U_r = 0$).

$$U_r = \frac{U_g}{f D} \quad (5.12)$$

The general governing system of equations for the flow-structure interaction can be summarized in matrix form as in Eq. (5.13), in which w_i is a generalized displacement vector. $[M_s]$, $[C_s]$, and $[K_s]$ are the structural mass, damping, and stiffness matrices, respectively. Eq. (5.13) can be transformed into Eq. (5.14) by allocating all the terms to the LHS to obtain the overall mass $[M]$, damping $[C]$, and stiffness $[K]$ matrices.

$$[M_s]\{\ddot{z}_i\} + [C_s]\{\dot{z}_i\} + [K_s]\{z_i\} = \{F_i\} = [M_a]\{\ddot{z}_i\} + [C_a]\{\dot{z}_i\} + [K_a]\{z_i\} \quad (5.13)$$

$$[M]\{\ddot{z}_i\} + [C]\{\dot{z}_i\} + [K]\{z_i\} = \{0\} \quad (5.14)$$

These equations can be rewritten in the state space form as shown in Eq. (5.15), which represents an eigenvalue problem or its equivalent in Eq. (5.16).

$$\begin{Bmatrix} \dot{z}_i \\ \ddot{z}_i \end{Bmatrix} = \begin{bmatrix} [0] & [I] \\ -[M]^{-1}[K] & -[M]^{-1}[C] \end{bmatrix} \begin{Bmatrix} z_i \\ \dot{z}_i \end{Bmatrix} \quad (5.15)$$

$$\{\dot{q}\} = [A]\{q\} \quad (5.16)$$

The eigenvalues of the state matrix $[A]$ are complex and are a function of the reduced velocity U_r . The system is considered stable when the real parts of all the eigenvalues are negative. However, if one eigenvalue has a positive real part, the system is considered unstable, and this eigenvalue and its corresponding eigenvector determine the mode of vibration.

5.3. Results

5.3.1. Flow forces

Flow forces acting on each tube in the 7-tube kernel were calculated by integrating the pressure around each tube then decomposing the resultant force into the transverse (*x-dir*) and streamwise (*y-dir*) components. The central tube, C, was forced to oscillate sinusoidally with a constant amplitude A of $0.08 D$ and a frequency of 8 Hz in each of these directions. Furthermore, Fast Fourier Transformation (FFT) was performed to extract the dynamic forces acting on all kernel's tubes due to the forced oscillation of tube C at the frequency of such oscillation. This process was repeated for various flow approach angles, reduced flow velocities, and air void fractions. These forces were presented in terms of the normalized force coefficient c_f and a phase angle ϕ . A positive value of the phase angle means that the fluid force leads to the displacement motion of Tube C.

Figure 5.4 shows the effect of the reduced flow velocity and the air void fraction on the fluid forces acting on Tube C. The forces presented are at the global *x-dir* for the 45° orientation angle configuration. It was found that the air void fraction in the range of 0% (water flow) to 80% has little effect on the predicted fluid forces. However, significant differences were found in the

prediction at a 100% air void fraction when compared with the other air void fraction predictions (0% to 80%). This difference is significant to the phase angle prediction (Fig. 5.3-b). The difference is less pronounced in the prediction of the fluid force coefficient, especially at lower ($U_r < 5$) and higher ($U_r > 20$) reduced flow velocities. In experimental studies, this has often been attributed to the change in the two-phase flow regime (Pettigrew, Tromp, et al., 1989). Based on homogenous flow properties, flow phase velocities, and experimental observations, Pettigrew et al., (1989) reported that the flow was mostly homogeneous and remained in the bubbly regime up to 80%~90% of the air void fraction. At higher void fractions, the flow became intermittent and was characterized by periods of water floods and bursts of air.

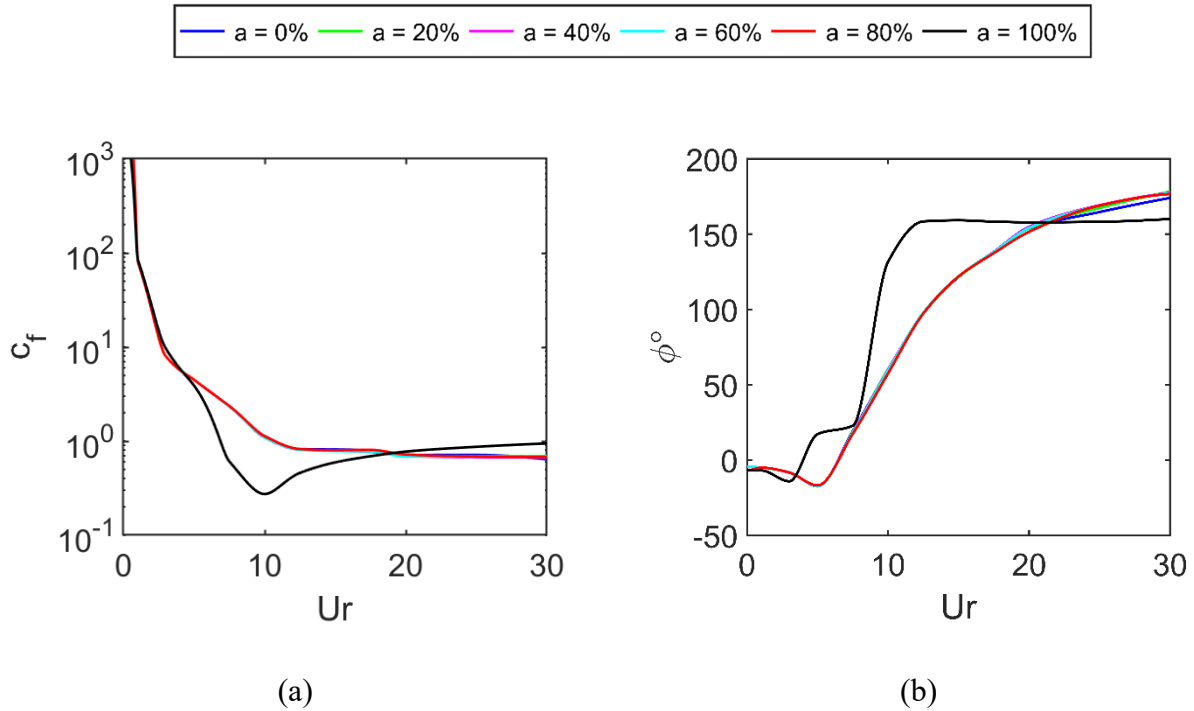


Figure 5.4: The effect of the air void fraction on the fluidelastic forces, F_{xx} acting on Tube C at a 45° orientation (the forces are in the x-dir when Tube C oscillates in the x-dir): a) the force coefficient magnitude, and b) the phase angle.

Hassan et al. (2010) found that the prediction of the fluidelastic force amplitude was less sensitive to variations in the Reynolds number. However, they found that the Reynolds number has a significant influence on the phase angle, which resulted in a change in the predicted stability threshold. Figure 5.5 shows the variation in the average Reynolds number at $U_g = 1 \text{ m/s}$ with a

change in the air void fraction. The Reynolds number was calculated using the properties of the homogeneous mixture at the inlet boundary as a representation for the average temporal and spatial void fraction value in flow domain. Here, the tube's diameter D is the characteristic length. It is worth noting that the air void fraction is set to be uniform at the inlet boundary. The flow is allowed to develop freely in the flow domain depending on the flow conditions and the geometrical constraints of the domain. The calculated number decreases slightly from 42,000 to 40,000 as the air void fraction increases in the range of 0% to 80%. For void fractions higher than 80%, the Reynolds number drops sharply to almost 5% of its average value in the range of a 0% to 80% air void fraction.

Further simulations were conducted at a 95%, 99%, 99.5% and 99.8% air void fraction at a 45° orientation to capture the change in the fluidelastic forces at a higher void fraction with a lower Reynolds number, as shown in Fig. 5.6. The fluidelastic forces on all the monitored tubes showed that at very high air void fractions (99%), the rate of change was very high. For instance, the predicted forces and phases for Tube E are shown in Fig. 5.6. In Fig. 5.6-a, the magnitude of the force coefficient drops by nearly half of its value within the last 1% of the the air void fraction (from 99% to 100%). In Fig. 5.6-b, it can be seen that the phase angle increases by 40° within the same range. This demonstrates the pronounced effect of the Reynolds number on the change in the fluidelastic forces at different air void fractions.

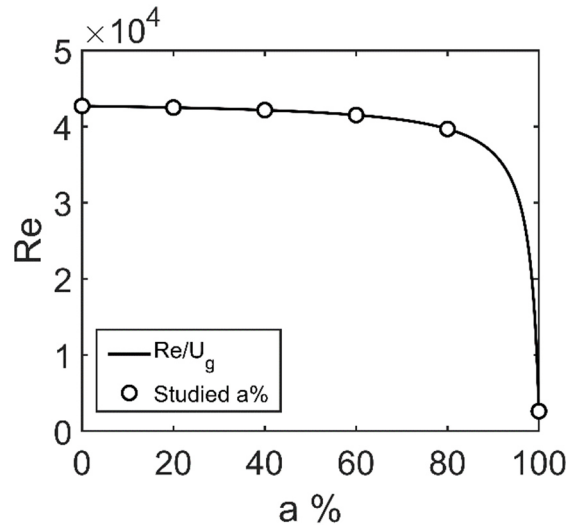


Figure 5.5: Variations in simulated Reynolds numbers at a unity gap velocity of $U_g = 1 \text{ m/s}$ against the air void fraction.

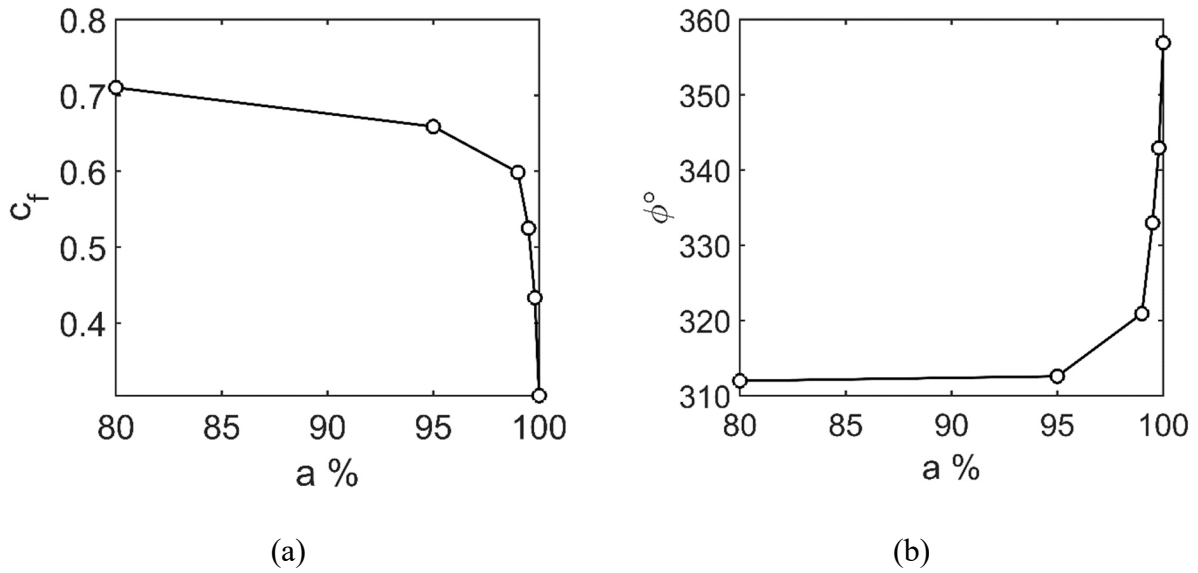


Figure 5.6: Variations in the fluidelastic force F_{xx} at high air void fraction values, a 45° orientation, and a $U_r = 15$, for Tube E: a) force coefficient magnitude, and b) phase angle.

In steam generators, the U-bend region is susceptible to severe vibration due to fluidelastic instability and therefore, anti-vibration bars are integrated into this region. This region is also characterized by a high gas void fraction at the hot leg portion of the U-bend (Ferng & Chang, 2008). From the results presented above, a very high gradient of the predicted forces is obtained in the higher range of the void fractions. As such, the uncertainty in the prediction of the void fraction can lead to large error in the stability threshold prediction, which is highly undesirable.

A larger set of results demonstrates the effect of the orientation of the array on the fluidelastic force, as shown in Figs. 5.7 and 5.8. Both figures show the magnitude coefficient c_f and the phase angle ϕ of the fluidelastic force acting on Tube C as a function of the reduced velocity (U_r) and the air void fraction. In Fig. 5.7, the transverse forces due to the oscillation of Tube C in the x -dir are shown. In comparison, Fig. 5.8 shows the streamwise forces due to the oscillation of Tube C in the y -dir. Since the fluidelastic forces were insensitive to an air content in the flow of up to 80%, only one trendline will be used to represent this void fraction range.

In Fig. 5.7, the variation in the force coefficients seems to be less sensitive to the reduced velocity than the corresponding phase angles. Generally, a force coefficient is very large at a low reduced velocity; it then reaches a plateau variation after a $U_r > 10$. This behavior was observed in the literature (Hassan et al., 2010; Sadek et al., 2018). In comparison, the phase angle trend increases and reaches a plateau as $U_r \approx 18$ for a 55° orientation (Fig. 5.7-h). For 30° and 37.5° orientations

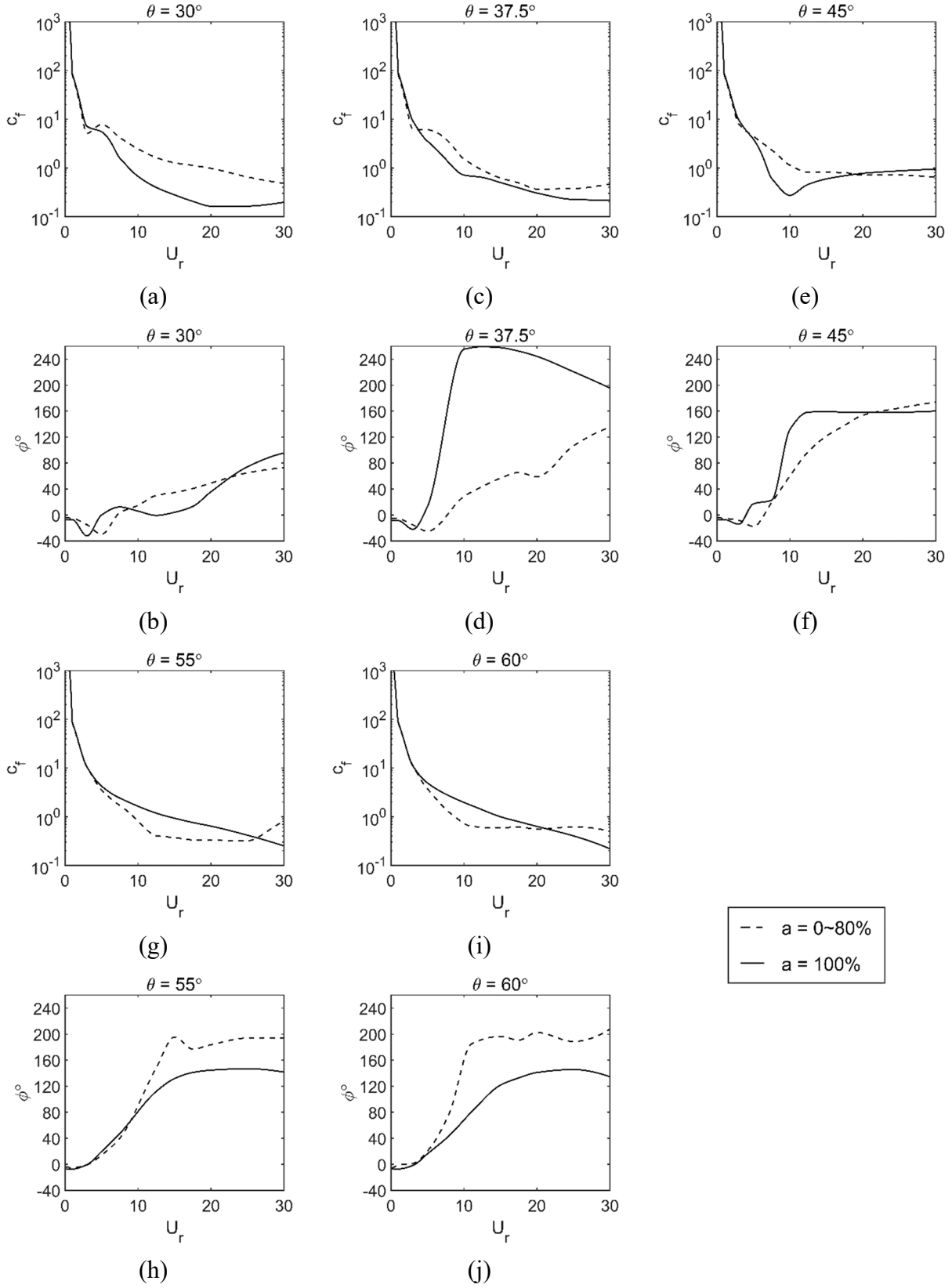


Figure 5.7: Fluidelastic forces F_{xx} acting on Tube C for different orientation angles. The forces are in the x-dir when Tube C oscillates in the x-dir.

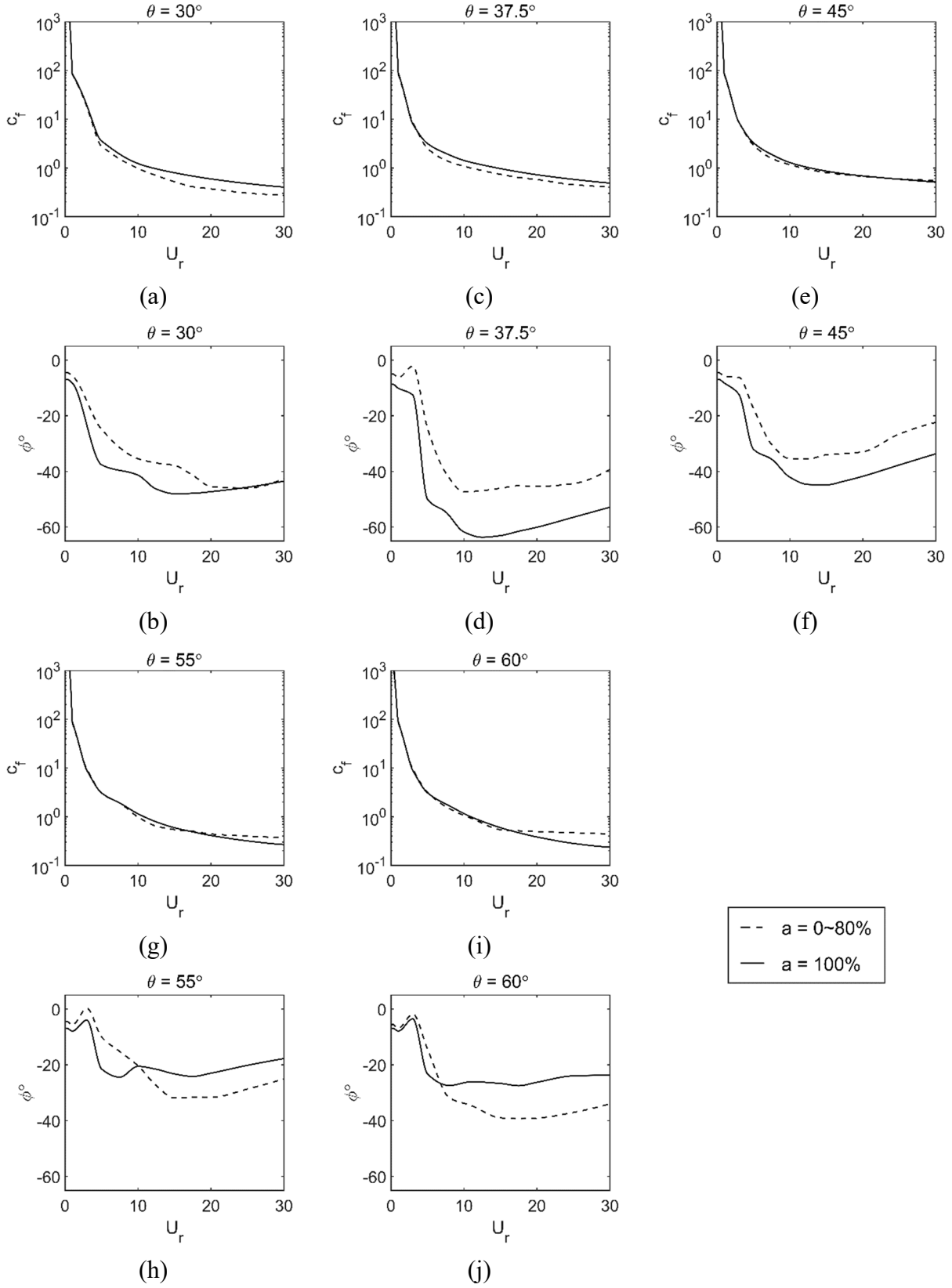


Figure 5.8: Fluidelastic forces F_{yy} acting on Tube C for different orientation angles. Forces are in the y-dir when Tube C oscillates in the y-dir.

(Figs. 5.7-b and 5.7-d respectively) a similar plateau was not observed in the reduced velocity range, and the rate of change was not as high as that for a 55° orientation.

Another observation regarding the phase angle for normal triangular arrays (30° orientation) is that it decreases in value below 0° as it switches from lead to lag forces. This occurs until it reaches a minimum at $U_r \approx 5$ for a 0% to 80% air void fraction, while it exists at a lower U_r for 100% air as shown in Fig. 5.7-b. This trend shows a gradual decay as the tube array rotates toward the parallel triangular orientation, and completely disappears for 55° and 60° orientations, as shown in Figs. 5.7-h and 5.7-j, respectively. This suggests a gradual transition of the flow pattern from the one in a normal triangle array to the one in a parallel triangle array. This will be further analyzed and discussed in the next section.

For forces in the y -dir, shown in Fig. 5.8, the force coefficient and the phase angle variations with U_r are generally similar among the orientation angles of all the arrays. Beyond $U_r = 10$, all force coefficients become asymptotic to a value of ~ 0.3 regardless of the orientation angle of the array. The phase angle between the fluidelastic forces and the tube motion at a quiescent flow (i.e. $U_r = 0$) is about -4.5° for all orientations and decreases slightly up to $U_r \cong 4$. After that, a sharp decrease takes place until $U_r = 10$, after which a slight recovery in the phase angle value begins. This is the typical phase angle variation with a reduced flow velocity that is observed for all orientation angles. However, some differences exist between the different orientations for the lower limit of the phase angle, although, they are still in the $-30^\circ \sim -50^\circ$ range.

From Figs. 5.7 and 5.8, the air void fraction effect in the range from 80% to 100% is very significant on the transverse force in the x -dir. This may lead to a change in the FEI stability threshold for some orientations. For example, if only the damping-controlled mechanism is considered (i.e. a single flexible tube in transverse direction), a positive phase angle value means that the fluidelastic force is leading the tube motion. This results in a positive energy feedback between the flow and the structure and may initiate FEI if the structural damping is not high enough to dissipate this energy. For orientations of 30° , 37.5° , and 45° the phase angle value of the flow force becomes positive for an air flow at a lower reduced velocity than that for an air-water mixture. This occurs up to a 99% air void fraction if the detailed force variation in Fig. 5.6 is considered. This is an indication of a switch in the air flow that occurs at almost half the reduced velocity value of an air-water mixture at orientations of 30° and 37.5° . For an orientation of 55° ,

the sign switch occurred at the same reduced velocity regardless of the air void fraction. In comparison, for the streamwise direction only the stiffness-controlled mechanism is responsible for FEI. Therefore, any change in the streamwise phase angle of the tube due to the void fraction will affect the stability threshold either adversely or favorably.

5.3.2. Flow visualization

Experimental flow visualizations conducted by Weaver and Abd-Rabbo (1985) and Scott (1987) showed that the flow inside the tube array has a distinct flow pattern which is dependent on the array type and in some cases, the pitch-to-diameter ratio. As discussed in the previous section, the flow pattern between the tubes greatly affects the fluidelastic forces. Therefore, a visualization of the flow channels at various orientation angles becomes important to understand the relation between the flow approach angle or the orientation of the array, and the onset of fluidelastic instability. Since this work utilizes a two-dimensional domain, the rotation of the domain is always along an axis parallel to the tubes' axes. Therefore, the flow direction is always perpendicular to the tubes, and the spanwise flow structures are coherent. Figure 5.9 represents this visualization by extracting the flow streamlines for the five orientation angles that were investigated. The streamlines were calculated based on the velocity field of the time-averaged mixture between the stationary tubes. Flow periodicity and vortex zones are filtered out since time-averaging provides a better picture. These flow patterns are extracted at $U_r = 3$ and a 0% air void fraction (i.e. water flow).

Figures 5.9-a and 5.9-e show the flow patterns in a normal and a parallel triangular array, respectively. In a normal triangular array, the flow is distinguished by having fluid flow through the two channels which form between adjacent tubes (colored in blue). The two channels are well separated along clear, straight line boundaries. Each of the two channels is in contact with the central tube and attaches to the other through the downstream tubes at a 90° angle. This angle is measured from the horizontal x -axis. The two channels then pass through the gap between the two downstream tubes. In comparison, the flow pattern within the parallel triangular tube array is recognized by its single, wavy flow channel shape between adjacent tubes (colored in red). As such, only one flow channel is observed in the space between the tubes. When inspecting other orientation angles (37.5° and 45°), the flow streamlines show a combination of normal and parallel

flow patterns. However, the 55° orientation behaves as a pure parallel triangular array. To quantify this variation, a hexagonal cell with the same orientation as the array is considered. The width of the cell is equal to the pitch of the array. The percentage of the parallel flow pattern is then defined by the ratio of the mass flow rate, which follows the parallel pattern to the total mass flow rate that crosses the hexagonal cell, as shown in Fig. 5.10-a.

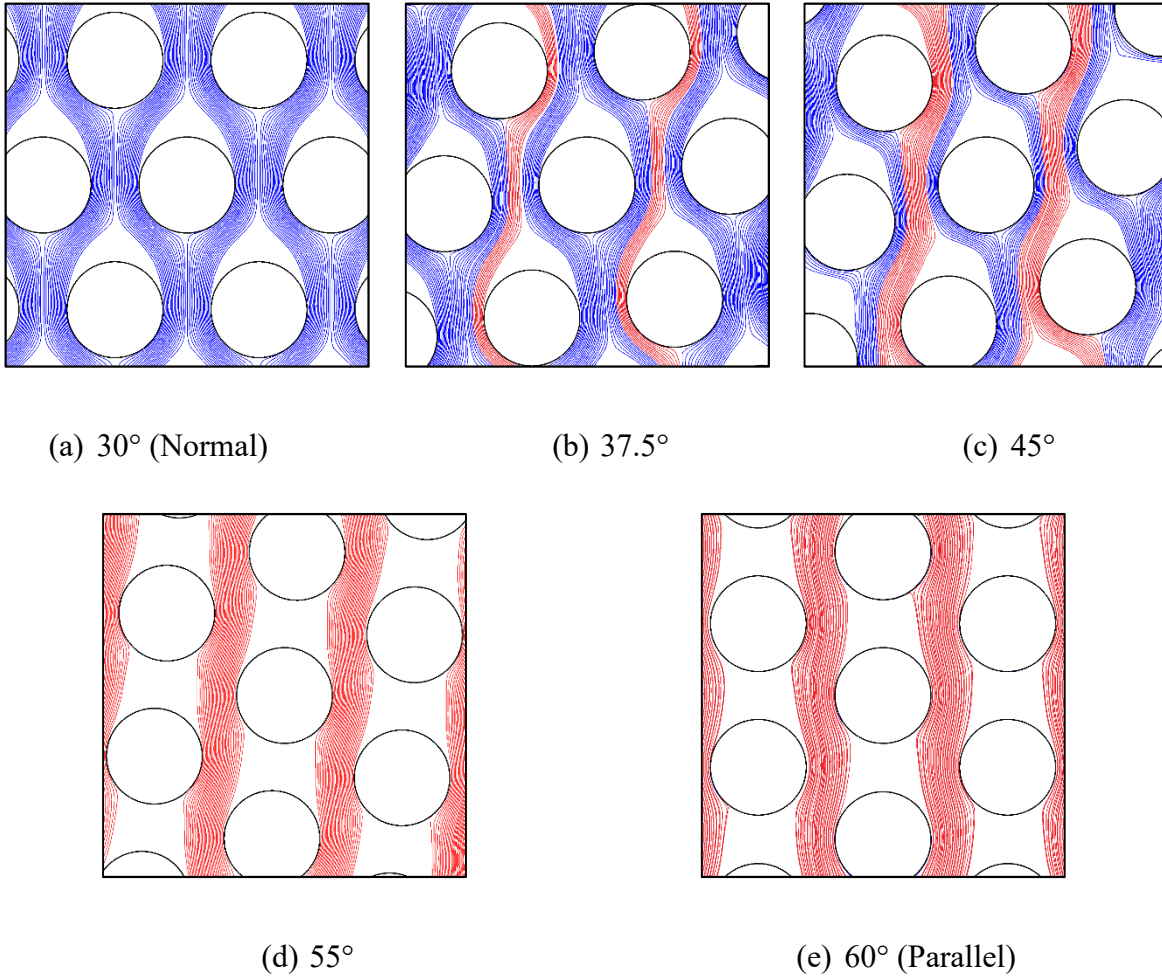


Figure 5.9: Average water flow streamlines for 30° , 37.5° , 45° , 55° and 60° orientation angles at $U_r = 3$. Blue indicates a normal triangular array-like flow pattern, while red is a parallel triangular array-like flow pattern.

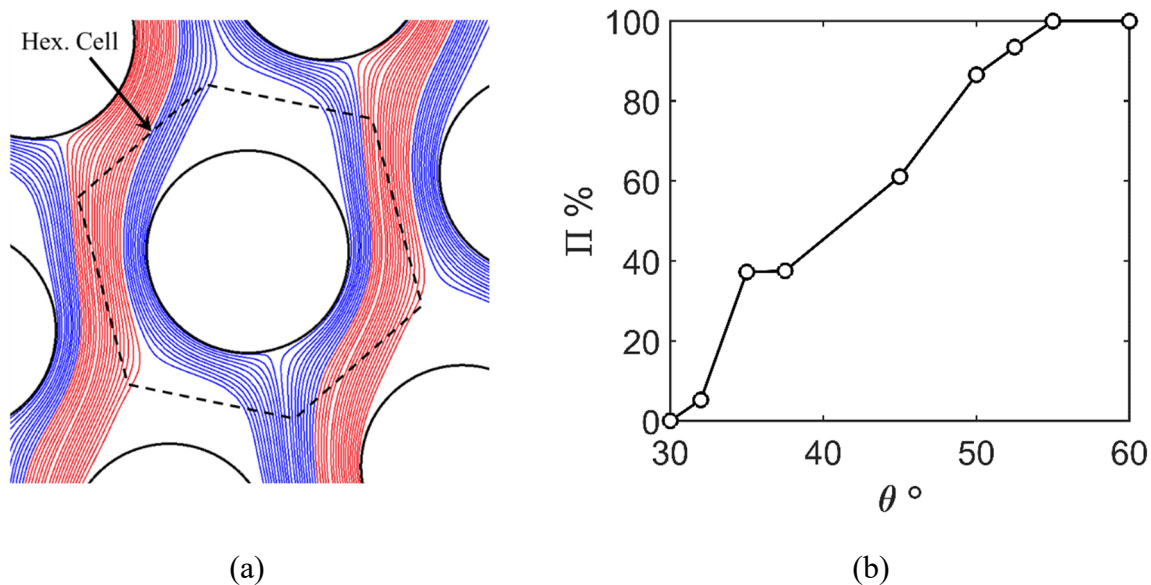


Figure 5.10: Percentage of parallel triangular flow: a) Hexagonal cell boundary, and b) variation of parallel flow with orientation angle.

Figure 5.10-b summarizes the variation in the parallel flow ratio (Π) as a percentage of the total flow with respect to the orientation angle of the array. This flow pattern analysis was performed on additional orientation angles of 32°, 35°, 50°, and 52.5° to provide a detailed examination of the variation in the parallel flow ratio with respect to the orientation angle. The variation is quasi-linear in the range of the 37.5° to 50° orientation angles. The data in Fig. 5.10-b were presented for a reduced velocity of three. The same analysis was conducted at higher reduced velocities up to 30. It was found that the flow velocity has a marginal effect on the calculated pattern percentage. Therefore, within the range of a reduced velocity between 0 – 30 ($U_g = 0 - 9.12$ m/s), the flow pattern percentage is considered to be only a function of orientation angle.

5.3.3. FEI force - Approach angle in a semi analytical model

The discussion earlier leads to the conclusion that FEI forces for any orientation angle or flow approach angle inherit some features from their counterparts in both standard normal and parallel arrays. This is due to the flow pattern within the tubes in these arrays which strongly resembles the normal and parallel triangular flow pattern. Therefore, it is proposed that FEI forces at any orientation can be expressed as a weighted superposition of the FEI forces of normal and parallel

triangular arrays. It should be noted that this flow pattern calculation is based on the time-averaged flow; other effects, such as flow vorticity, are ignored. Therefore, any fluidelastic force component mn at any orientation θ is:

$$\mathbf{F}_{\theta,mn} = \Pi \mathbf{F}_{60^\circ,mn} + (1 - \Pi) \mathbf{F}_{30^\circ,mn} \quad (5.17)$$

where mn is a set of two directions that belong to the m -direction of the force when a tube is oscillating in n -direction. As an example, these sets of directions can be xx , xy , yx , and yy for the global coordinates x - y . Π is the parallel flow fraction as calculated from the hexagonal cell criterion. Equation (5.17) can be rewritten in a non-dimensional form similar to that of Eq. (5.10) as shown in Eq. (5.18-a). \mathbf{C} is a complex variable which contains both information regarding the FEI force coefficient magnitude and the phase angle as shown in Eq. (5.18-b):

$$\mathbf{C}_{\theta,mn} = \Pi \mathbf{C}_{60^\circ,mn} + (1 - \Pi) \mathbf{C}_{30^\circ,mn} \quad (5.18-a)$$

$$\mathbf{C} = c_f \angle \phi \quad (5.18-b)$$

Equation (5.17-a) has the restriction that in order to calculate the fluidelastic force component mn , only the corresponding fluidelastic components mn for the standard normal and parallel triangular arrays shall be used. For instance, if the component $\mathbf{C}_{45^\circ,xx}$ is to be calculated, a knowledge of the corresponding $\mathbf{C}_{30^\circ,xx}$ and $\mathbf{C}_{60^\circ,xx}$ is required. In standard normal and parallel triangular arrays, these forces are always measured in the transverse direction when a single tube is oscillating in the x -dir. When rotating the bundle by angle γ , the transverse direction is no longer aligned with the global x coordinate, as shown in Fig. 5.11-a. Instead, it becomes aligned with the x' local coordinate.

To express the forces in terms of the global coordinates x and y , a linearization was done for the fluidelastic force. By assuming that the central tube is oscillating in its local coordinate direction x' with a small amplitude X' , its trajectory can be projected into the x and y directions (Fig. 5.11-c). Moreover, the induced fluidelastic force vector $\mathbf{F}_{x'x'}$ can be assumed to be a summation of the vectors $\mathbf{F}_{x'x}$ and $\mathbf{F}_{x'y}$, as shown in Fig. 5.11-b. These vectors represent the force in the x' direction when the tube oscillates in the x and y directions, respectively. Therefore:

$$\mathbf{F}_{x'x'} = \mathbf{F}_{x'x} + \mathbf{F}_{x'y} \quad (5.19-a)$$

$$X' = \frac{X}{\cos(\gamma)} \quad , \quad Y' = \frac{Y}{\sin(\gamma)} \quad (5.19-b)$$

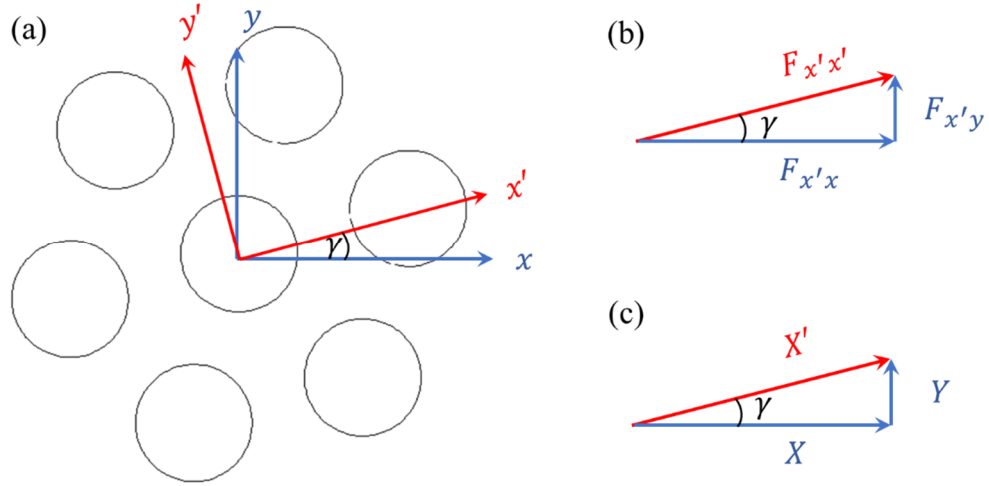


Figure 5.11: Transformation of coordinates: a) global and local coordinates, b) force vectors, and c) oscillation amplitudes.

When divided by $\frac{1}{2}\rho_m U_g^2 X'$, Eq. (18a) yields its non-dimensional form. Now by using Eq. (5.19-b), the force coefficients can be rewritten in terms of the rotation angle γ as:

$$C_{x'x'} = C_{x'x} \cos(\gamma) + C_{x'y} \sin(\gamma) \quad (5.20)$$

where the force coefficients $C_{x'x'}$, $C_{x'x}$, and $C_{x'y}$ include the magnitude and phase angle information as presented in Eq. (5.18-b). Here, only the direction of oscillation was transformed into the coordinates x and y and therefore the monitored force direction was transformed as well. To achieve this, the rotation of the transformation of the axes is utilized and the force coefficient $C_{x'x'}$ can be expressed in terms of the rotation angle γ as:

$$C_{x'x'} = [C_{xx} \cos(\gamma) + C_{yx} \sin(\gamma)] \cos(\gamma) + [C_{xy} \cos(\gamma) + C_{yy} \sin(\gamma)] \sin(\gamma) \quad (5.21)$$

Similarly, the general transformation matrix for all fluidelastic force coefficient components $C_{y'x'}$, $C_{x'y'}$ and $C_{y'y'}$ for the x' - y' coordinate system can be derived in terms of C_{xx} , C_{yx} , C_{xy} and C_{yy} as follows:

$$\begin{bmatrix} C_{x'x'} \\ C_{y'x'} \\ C_{x'y'} \\ C_{y'y'} \end{bmatrix} = \begin{bmatrix} \cos^2(\gamma) & \sin(\gamma) \cos(\gamma) & \sin(\gamma) \cos(\gamma) & \sin^2(\gamma) \\ -\sin(\gamma) \cos(\gamma) & \cos^2(\gamma) & -\sin^2(\gamma) & \sin(\gamma) \cos(\gamma) \\ -\sin(\gamma) \cos(\gamma) & -\sin^2(\gamma) & \cos^2(\gamma) & \sin(\gamma) \cos(\gamma) \\ \sin^2(\gamma) & -\sin(\gamma) \cos(\gamma) & -\sin(\gamma) \cos(\gamma) & \cos^2(\gamma) \end{bmatrix} \begin{bmatrix} C_{xx} \\ C_{yx} \\ C_{xy} \\ C_{yy} \end{bmatrix} \quad (5.22)$$

The transformation matrix in Eq. (5.22) is analogous to the rotation of the plane stresses in solids where C_{xx} and C_{yy} are similar to the normal stresses σ_{xx} and σ_{yy} , and C_{yx} and C_{xy} are similar to the shear stress components τ_{yx} and τ_{xy} , respectively.

By using Eqs. (5.18-a), (5.18-b) and (5.22), the approximate fluidelastic forces can be reconstructed from the known fluidelastic forces of the standard normal and the parallel triangular arrays. These forces are available in literature (Olala & Mureithi, 2015; Sawadogo & Mureithi, 2014). Figure 5.12 and Fig. 5.13 depict comparisons between the calculated fluidelastic forces and their counterparts. These comparisons are extracted directly from the flow simulations for C_{xx} and C_{yy} , respectively, and they are broken down into their magnitude and phase angle values.

Both figures show a good agreement between the calculated forces through the semi-analytical transformation method and the flow simulated forces. The force magnitudes are well predicted for the transverse force in orientations of 37.5° and 55° (Figs. 5.12-a and 5.12-e) and for the streamwise force magnitudes of all of the orientation angles (Figs. 5.12-a, 5.12-c, and 5.12-e), although the magnitude of the transverse force coefficient in Fig. 5.12-c is underestimated for 1 to 0.2 at $U_r > 10$. For Figs. 5.12-b, 5.12-d, and 5.12-f, the phase angles that were calculated for the transverse force at all of the different orientations agree well with the simulations. For the streamwise direction (Figs. 5.13-b, 5.12-d, and 5.13-f) the semi-analytical calculations are within $\pm 15^\circ$ from the values that were obtained from the simulation at $U_r > 5$.

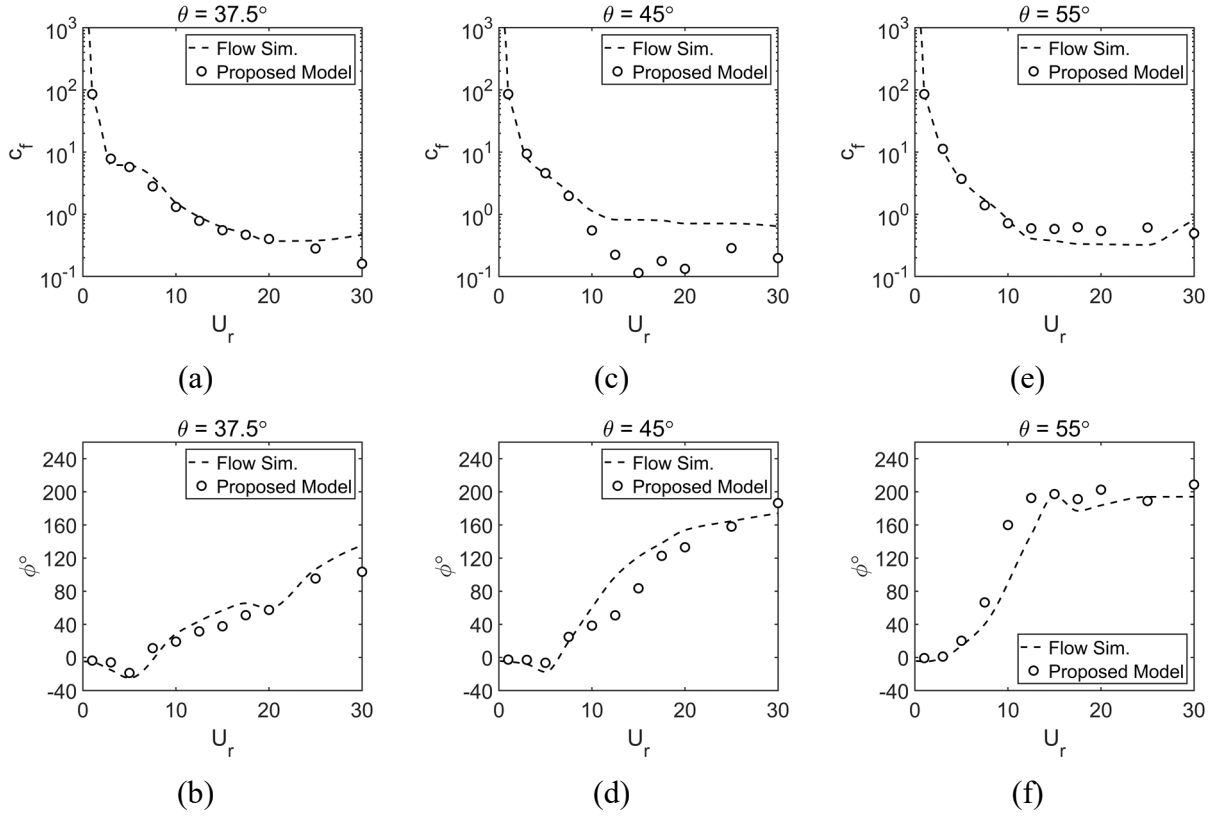


Figure 5.12: The simulated vs. the calculated semi-analytical fluidelastic force in the x-dir for Tube C, at a 0% ~ 80% air void fraction. The force coefficient and the phase angle are for: a) & b) a 37.5° orientation angle; c) & d) a 45° orientation angle; and e) & f) a 55° orientation angle.

5.3.4. Stability analysis

Unconstrained stability analyses were performed for various tube bundle orientations. The tubes in the flexible kernel were adjusted to have the same natural frequency in both the transverse and the streamwise directions; thus, no preferred FEI direction was imposed. The stability analysis was performed in the system of equations presented in Eq. (5.16). This system accounts for the structural and flow-added effects obtained from the dynamic flow force using the CFD simulations in section 5.3.1. The natural frequency and the damping logarithmic decrement for each flexible tube were set to 8 Hz and 0.0069, respectively. For the orientation angle and the flow reduced velocity of a given array, the stability map was determined by starting from a very low mass-damping parameter ($MDP = \frac{m_s \delta}{\rho_m D^2}$) where the kernel is unstable. The mass-damping parameter was then increased incrementally. The stability threshold was determined when the kernel reached stability. A complete map was therefore obtained by considering several values of reduced

velocities and repeating the same process. The mass-damping parameter was controlled by varying the flow density between 1000 kg/m^3 (water) and 1.2 kg/m^3 (air), while keeping the tube mass per unit length (m_s) and the structural logarithmic decrement (δ) fixed.

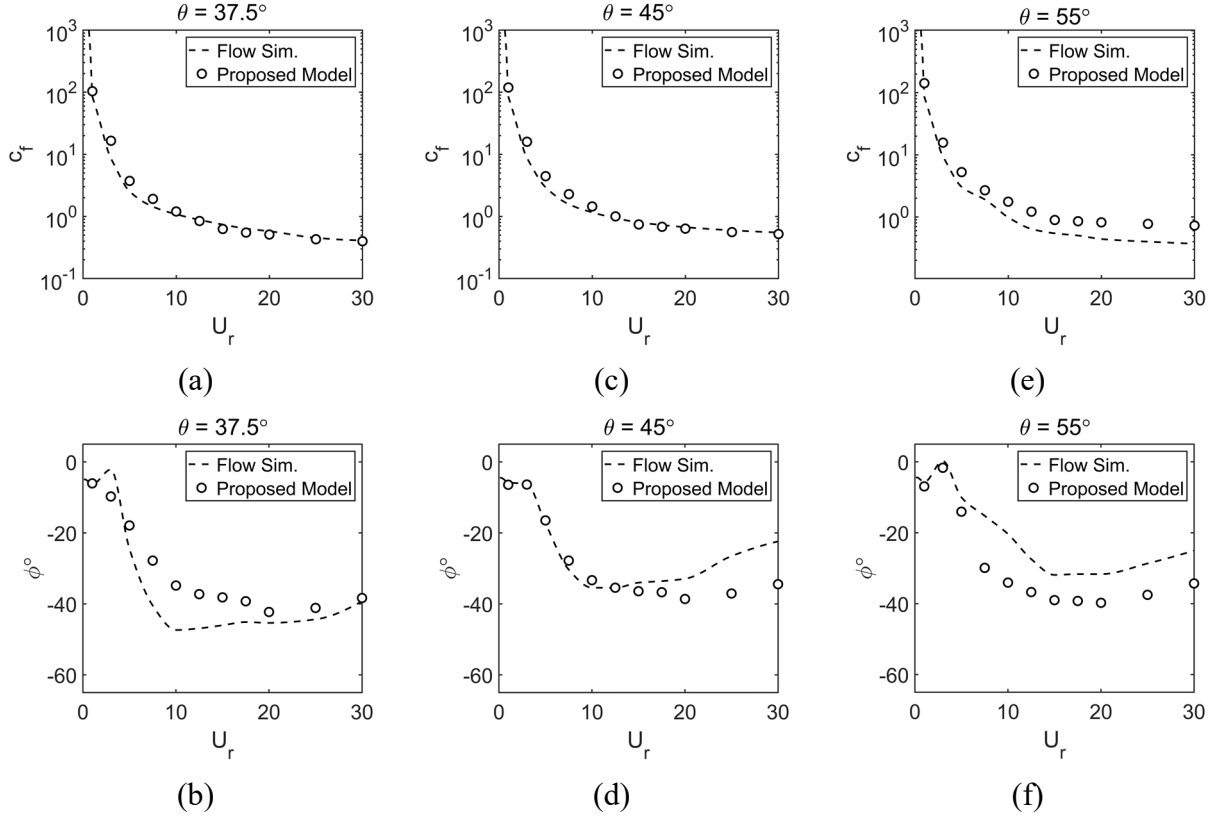


Figure 5.13: The simulated vs. the calculated semi-analytical fluidelastic force in the y-dir for Tube C, at a 0% ~ 80% air void fraction. The force coefficient and the phase angle are for: a) & b) a 37.5° orientation angle; c) & d) a 45° orientation angle; and e) & f) a 55° orientation angle.

Figure 5.14 shows the stability maps for the five different flexible kernels, which are oriented at approach angles of 30° (normal triangle), 37.5° , 45° , 55° , and 60° (parallel triangle). The effect of the approach angle is evident in the low mass-damping parameter region ($MDP < 1$). In this region, the parallel triangular array is the least stable. The 45° and 55° orientations show almost double the stability threshold of the parallel triangular array at an $MDP = 0.0148$ with critical reduced velocity values of 2.1 and 2.4, respectively. This was unexpected since, as discussed in the previous section, the 55° orientation array is very similar to the parallel triangular array in terms of the flow pattern and the fluidelastic forces. Therefore, it was anticipated that the stability threshold for 55° and the parallel triangular arrays would be close. However, experimental observations by Weaver

and Fitzpatrick (1988) showed that at low mass-damping parameters, the measured stability threshold was characterized by a large scattering for all standard arrays. As the approach angle of the array changes towards the normal triangular orientation, the critical reduced velocity increases noticeably. In contrast, the intermediate 37.5° array shows two zones of instability: a major zone, which extends to high values of critical velocities and mass-damping ($MDP > 1$), and a minor instability sub-zone, which only exists at $MDP < 1$. At a low value of $MDP = 0.0148$, this subzone stretches between $U_{r,cr} = 2.8$ to 9.

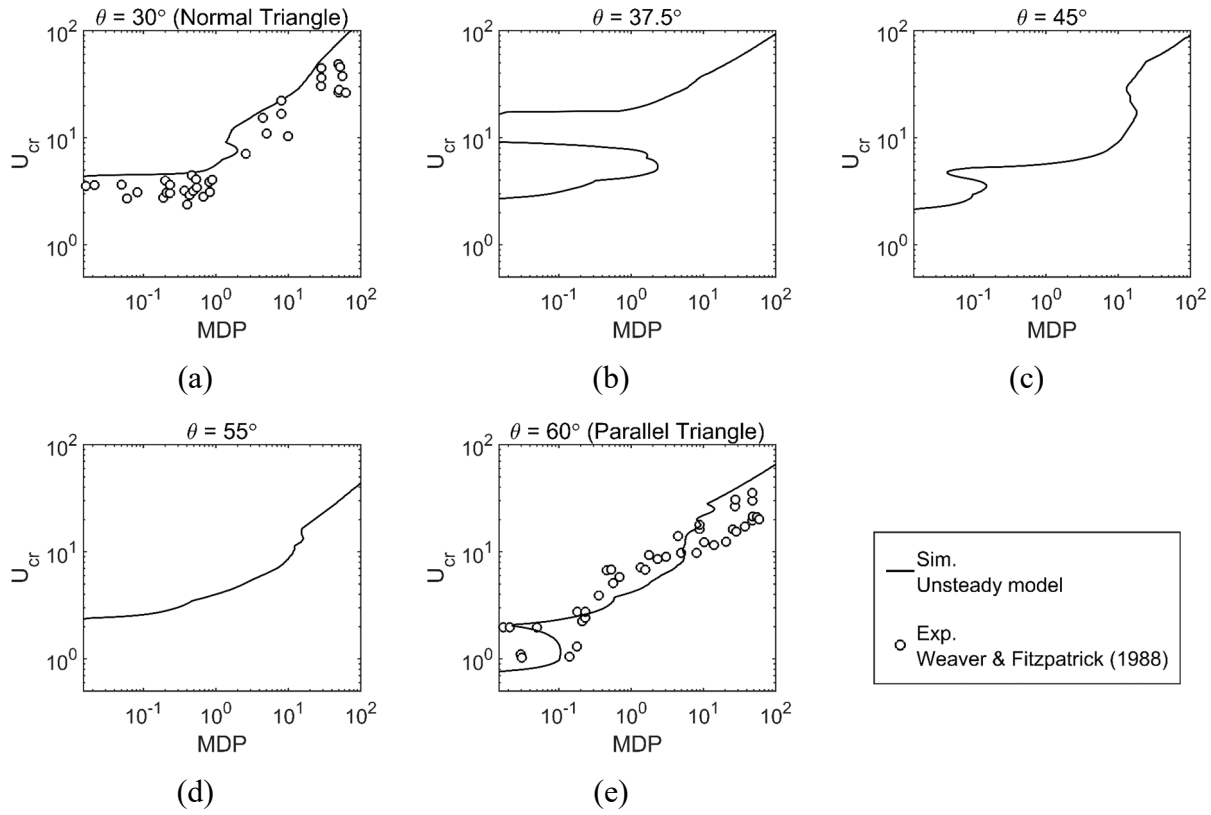


Figure 5.14: FEI stability maps for different flow approach angles: a) 30° orientation (normal triangle), b) 37.5° orientation, c) 45° orientation, d) 55° orientation, and e) 60° orientation (parallel triangle). The experimental values are extracted from Weaver & Fitzpatrick (1988).

The stability maps that were obtained for the normal and the parallel triangular arrays were also compared against the corresponding experimental stability data seen in Fig. 5.14-a and 5.14-e, respectively. This data was provided by Weaver and Fitzpatrick (1988). It is worth noting that the fluidelastic force data obtained from the flow simulations were extrapolated from $U_r = 30$ to 100. This was done to cover the mass damping parameters above $MDP = 12.33$, at which point the flow

is air. This showed an approximation of the stability threshold against the experimental data at high MDP values; therefore, a moderate agreement was expected at these MDP values. For a mass-damping parameter range obtained by changing the flow density from pure water to pure air (MDP = 0.0148 to 12.33), there is an excellent agreement between the predicted and the experimental stability threshold. This is particularly apparent for the parallel triangular array, seen in Fig. 5.14-e. Nevertheless, for the normal triangular array, seen in Fig. 5.14-a, the predicted threshold is acceptable as it matches the upper boundary of the threshold of the uncertainty margin.

The instability threshold was also compared with the experimental measurements obtained by Yeung & Weaver (1983) in their water tunnel for different orientation angles. This comparison is shown in Fig. 5.15. In this 1983 study, the instability threshold was measured for a low mass-damping parameter of 0.0148. Considerable variation was reported in the critical velocities for trials regarding orientation angles of 37°, 40° and 42.5°. The two reported points in these measurements indicated the upper and lower bounds of the measured critical velocities. For example, the variability in the measured stability threshold is about 100% for an approach angle of 38°.

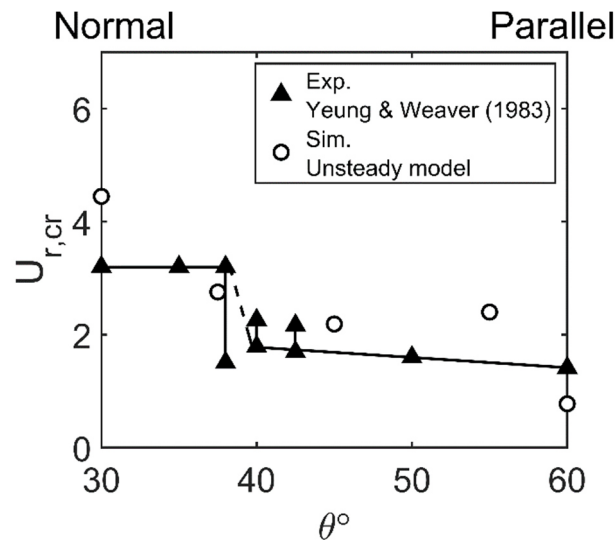


Figure 5.15: Effect of the flow approach angle on the FEI at MDP= 0.0148. The experimental data are obtained from Yeung & Weaver (1983).

The stability thresholds obtained by the current study agree with the experimental part for orientation angles of 60°, 45°, and 37.5°. For the 55° and 30° orientation arrays, the simulations overpredict the stability threshold. As mentioned earlier, scatter was observed in the stability

threshold among various experimental data at low mass-damping parameter values. These deviations are therefore falling within the acceptable limit. In general, the good agreement between the data from the experiments and the simulations lends confidence to the dependability of the flow model that was used.

5.4. Conclusion

This work focused on exploring the effect of the flow approach angle, which is also the orientation angle of the array, on the fluidelastic forces in arrays. As well, the FEI stability threshold was considered for a two-phase air-water flow. The investigation included the effect of different parameters, such as the air void fraction, the reduced velocity, and the orientation angle of the array. Following the success of the work of Sadek et al. (2018, 2020), a flow based numerical technique was employed to achieve these goals. The model utilized a 2-D domain to represent the arrays of different orientation angles. The same flow model parameters used in Sadek et al. (2018, 2020) were implemented in this study including: (1) tube and array dimensions; (2) meshing parameters and element sizing; (3) temporal discretization techniques; (4) turbulence, mixture, and homogenous flow models for the two-phase air-water flow; (5) the method used to extract the fluidelastic forces in the transverse and the streamwise directions; and (6) the unsteady model based approach for fluidelastic coupling and stability threshold prediction.

The results obtained and discussed throughout this work were essential to the understanding the behavior of fluidelastic instability in two-phase flows. These results can be summarized into the following points:

- Six air void fraction values were studied, which included 0% (water), 20%, 40%, 60%, 80%, and 100% (air). The fluidelastic forces in the transverse and the streamwise directions were almost identical for the first five air void fractions (i.e. up to 80%). The 100% void fraction (air flow) showed very distinctive fluidelastic forces from the other cases, which could contribute to an early excitation of fluidelastic instability in a normal triangular array. In the current simulations, it was found that this distinctive change in the forces occurs between air void fractions of 99% and 100%. The hot leg side of the U-bend region of a typical steam generator is characterized by the existence of high steam quality. As such, an

uncertainty in the prediction of the void fraction can lead to large error in the stability threshold, which could result in a catastrophic outcome.

- Five flow approach angles were inspected relative to the normal triangular array. These included angles of 0° , 7.5° , 15° , 25° , and 30° . The last value corresponds to a parallel triangular array. If the flow direction is fixed and the array is rotated, these angles correspond to orientation angles of 30° , 37.5° , 45° , 55° , and 60° . The fluidelastic forces acting at these array orientations were found to be highly dependent on the flow pattern inside the array. Moreover, these forces resembled the fluidelastic forces in both standard normal and parallel triangular arrays. By inspecting the flow streamlines inside each orientation angle, it was found that they could be classified into two groups: one group represents the flow pattern of the normal triangular array, while the other is for the flow pattern of the parallel triangular array. A simple technique was recommended to quantify the weight contribution of each category into the overall picture of the flow distribution.
- Based on this flow pattern decomposition, a semi analytical model involving the FEI force and the approach angle was proposed to calculate and reconstruct the forces at any flow approach angle/orientation angle of the array. This was accomplished by knowing the fluidelastic forces for the standard triangular array and the weight contribution of the corresponding flow pattern beforehand. The proposed method showed an excellent agreement with results obtained from flow simulations for the intermediate orientations. This validated both the proposed model and the flow pattern decomposition hypothesis. Such a model is a viable tool for a better prediction of the onset of FEI in actual steam generators, in which the direction of the flow is spatially related to the array changes.
- The FEI stability threshold was calculated via the unsteady based model for a classical 7-tube kernel for the orientation of each array. No preferred oscillation direction was imposed on the tubes, and the tubes were free to oscillate in both the transverse and the streamwise directions. The stability thresholds that were obtained were then compared against the experimental results provided by Weaver and Fitzpatrick (1988) for parallel and normal triangular arrays, and Yeung and Weaver (1983) for flow approach angles at very low mass-damping parameters. The stability thresholds were in very good agreement with the experimental data sets.

Chapter 6. The mechanisms of fluidelastic instability and the effect of frequency detuning in triangular tube bundles subjected to a two-phase flow

Complete citation

Sadek, O., Mohany, A., & Hassan, M. (2021). The mechanisms of fluidelastic instability and the effect of frequency detuning in triangular tube bundles subjected to a two-phase flow. To be submitted to the *Journal of pressure vessel technology*.

Author's contribution

O. Sadek: Conceptualization, Methodology, Software, Data curation, Writing- Original draft preparation.

A. Mohany: Supervision, Methodology, Writing- Reviewing and Editing, Resources, Funding acquisition.

M. Hassan: Supervision, Methodology, Writing- Reviewing and Editing, Visualization. .

Abstract

For decades, fluidelastic instability (FEI) has been known to cause drastic mechanical failure to steam generator tube bundles. Therefore, it has been extensively studied to mitigate its catastrophic consequences. Most of these studies were conducted in controlled experiments where significant simplifications to the geometry and flow conditions are implemented. One of these simplifications is the assumption that all tubes have the same natural dynamic characteristics. However, in typical steam generators, the natural frequencies of tubes are nonuniform due to manufacturing tolerances and tubes' curvature in the U-bend region. Such cases are unavoidable; thus, investigations commenced to understand the rule of frequency detuning on FEI in two-phase flow. This work attempts to investigate the effect of frequency detuning on transverse and streamwise FEI for air-water mixture flow. Isolation of FEI damping and stiffness mechanisms was carried out over the entire range of air void fraction, or equivalently, the mass-damping parameter. The study focused

on a specific frequency detuning pattern that results from the curvature of tubes in the U-bend region. It was found that frequency detuning could elevate the stability threshold caused by either mechanism at high air void fraction in the case of transverse FEI. Furthermore, the frequency detuning had a marginal effect on the stability threshold for water flow. It was observed that the mass-damping parameter has a critical impact on FEI under detuning conditions.

Keywords

Fluidelastic instability, steam generators, two-phase flow, frequency, detuning, mechanism.

6.1. Introduction

Structural integrity and safety of nuclear power generation equipment are of serious concern. Steam generators are of critical importance as vital components in the power generation cycle. They are often subjected to flow-induced vibrations during their life span. Four significant mechanisms lead to such vibrations: turbulent buffeting, vortex-induced excitation, acoustic resonance, and fluidelastic instability (FEI) (Pettigrew & Taylor, 1991; Weaver et al., 2000). The latter can lead to excessive vibrations and catastrophic failures in a short time. As such, FEI has received critical attention in the literature. Two mechanisms were identified to be responsible for FEI; a damping-controlled mechanism and a stiffness-controlled mechanism (Chen, 1983; M. P. Païdoussis, 1983). The first mechanism is responsible for FEI only requires one tube motion in a single direction (i.e., single-degree-of-freedom). In such a case, the tube's loss of stability is attributed to the reduction of the total damping (summation of structural and flow-added damping) to zero. On the other hand, the stiffness-controlled mechanism requires multiple flexible tubes or multiple degrees-of-freedom to take place. Thus, this mechanism involves coupling between motions of several tubes in a specific pattern to establish the instability. This is the fundamental feature of the displacement mechanism developed by Connors and later reformulated by Blevins (Blevins, 1977; Connors, 1970). As a consequence, if adjacent tubes in an array do not vibrate in a specific synchronous pattern at the same oscillation frequency, the excitation mechanism cannot be established, and the tube motion is stable. Thus, frequency detuning of tubes may affect the threshold of instability.

Frequency detuning may occur due to manufacturing tolerances or the variation in the tube radius inside a tube bundle; for example, in the U-bend region, the span length between supports of the tubes placed outward is different than those placed inward. One of the early studies on the tube detuning effects was done by Chen and Jendrzejczyk (1981). Multiple rows of tubes in inline and staggered arrays were detuned in a water flow. For such a liquid flow, the damping-controlled mechanism is dominant. It was concluded from this experiment that while the detuning had an insignificant effect on the critical flow velocity at which the instability occurs, it would have a more considerable impact if the stiffness-mechanism controlled the instability.

Moreover, Weaver and Koroyannakis (1983) performed an experimental study in a water loop for 2-DOF flexible tubes in a parallel triangular array of 1.375 pitch-to-diameter ratio. The natural frequencies of the two degrees of freedom were controlled. It was found that the stability threshold was elevated by 20% when the bundle was detuned with a small variation in the frequencies (up to 3%). For a more closely-packed square array of 1.33 pitch-to-diameter ratio, Tanaka and Takahara (1981) performed stability analyses to a two-row square bundle. The effect of detuning for air and water flows was investigated. It was shown that for airflow, the detuning of multiple tubes might increase the critical flow velocity up to 60% depending on the arrangement of detuned tubes, while for water flow, the effect is less pronounced. Cheng (1994) experimentally investigated the impact of flow density, or the mass ratio between tubes and displaced fluid, and the structural damping on detuning in an inline square array. They concluded that with a high mass ratio (airflow), the effect of detuning was very distinct on the FEI stability threshold; however, the increase in structural damping would reduce such impact. They suggested that the mass ratio and structural damping should be considered independently rather than combining them in a single non-dimensional mass-damping parameter. Price and Kuran (1991) investigated the FEI threshold for airflow in a rotated square array with a pitch-to-diameter ratio of 2.12. Fluidelastic instability was only observed with three and more flexible tubes, which suggested that the stiffness mechanism controlled the FEI. It was observed that detuning by lowering one tube's frequency would reduce the stability threshold and vice versa. This trend seems unique to the rotated square array and the pitch-to-diameter ratio studied since it was not reported elsewhere.

The study of detuning was revived in the past few years. Olala and Mureithi (2016) investigated the detuning effect on streamwise FEI for a 90% air-water mixture flowing through a parallel triangular array. This type of FEI is characterized by tubes being only flexible in the flow direction,

and the loss of instability in such a case results from the stiffness mechanism. To eliminate the effect of the detuning pattern, assigning random detuning to random tubes was adopted, and a statistical approach was employed. The amounts of detuning were then described in statistical variance. It was concluded that detuning had a favorable effect in stabilizing the array against streamwise FEI.

To make the calculations of the stability threshold tractable, tube arrays are often simplified by considering a kernel of tubes with uniform natural frequencies. Though tubes are not perfectly tuned in a typical steam generator. The detuning has a complex effect on such stability, which depends on many parameters such as array configuration, location of detuned tubes, structure-to-flow mass ratio, structural damping, and FEI flexibility direction. It is not universally accepted that frequency detuning has a significant impact on the stability threshold. While there is a strong belief that detuning would significantly affect if the stiffness mechanism is dominant. However, the FEI excitation mechanism is believed to be a combination of both the stiffness and damping mechanisms. The relative contribution of either of these mechanisms is dependent on the mass-damping parameter. As such, the detuning effect remains unclear. Moreover, most reported studies have focused on single-phase flows, either water or air flows, for which the detuning effect was different. Thus, it is beneficial to explore the impact of various void fraction in a two-phase flow. Therefore, this study will focus on investigating such a frequency detuning effect on FEI under a two-phase flow condition.

6.2. Methodology

The numerical approach is employed in this study. It is based on modeling the flow dynamics in a parallel triangular tube bundle via continuity and Navier-Stokes equations while the two-phase flow interactions is accounted for via drift-flux model (Hibiki & Ishii, 2003; Zuber & Findlay, 1965). A linear harmonic oscillator model is used to present tube flexibility. The flow/structure coupling is achieved by a one-way coupling via the FEI unsteady model (Chen, 1987; Tanaka & Takahara, 1981). Detailed descriptions for the models and validation analyses are provided in chapters 3 and 4 (Sadek et al., 2018, 2020); thus, brief descriptions will be provided here.

6.2.1. Flow domain

A two-dimensional flow domain that resembles a parallel triangular array is employed. It consists of 19 tubes and 14 half tubes arranged in three columns and 13 rows, as shown in Fig. 6.1. Each tube has a diameter D of 38 mm (1.5 in.) and the spacing between two consecutive tubes in the same column is 57 mm (2.25 in). This provides a pitch-to-diameter ratio (P/D) of 1.5. A distance of $5.5 D$ is provided upstream of the array to the inlet boundary to allow for the free development of the flow. On the other hand, plates parallel to the flow are added downstream of the array to reduce the large-scale periodicities behind the tube array (de Pedro et al., 2016). Although these periodicities may materialize behind the last row of tubes (Zdravkovich & Stonebanks, 1990), they are not considered to be linked to FEI. Seven tubes in the middle of the array, namely C , N , NE , NW , S , SE , and SW , are made preferentially flexible in either lift ($x-dir$) or drag ($y-dir$) directions depending on the performed analysis. Their motions are also monitored. All other tubes are rigid in the array.

An unstructured mesh is implemented with an average size of 1 mm for every quadrilateral cell. Finer prism cells are introduced on the surface of each tube, plate, and sidewall to resolve the high wall shear in such regions. For instance, 14 fine prism layers were introduced around each tube. Furthermore, the thickness of the first layer adjacent to the surface is small enough to guarantee that $y^+ \leq 1$. More details about the mesh and its sensitivity analysis are provided in (Sadek et al., 2018, 2020).

6.2.2. Numerical flow and two-phase models

The Reynolds Average Navier-Stokes (RANS) form of the governing fluid dynamics equations is used in this work as shown in Eq. (6.1-a) and Eq. (6.1-b), respectively. The two equations are casted into the mixture form of the drift-flux model to account for the multi-phase nature of the flow. This cast treats the flow as a single mixture for which any property Φ is determined by the volume-based void fraction a of each phase k as described in Eq. (6.2). Here in Eq. (6.1), ρ , μ , \mathbf{u} , P , and \mathbf{g} refer to the density, dynamic viscosity, velocity vector, static pressure, and the gravity field, respectively. The subscript m denotes the flow's mixture.

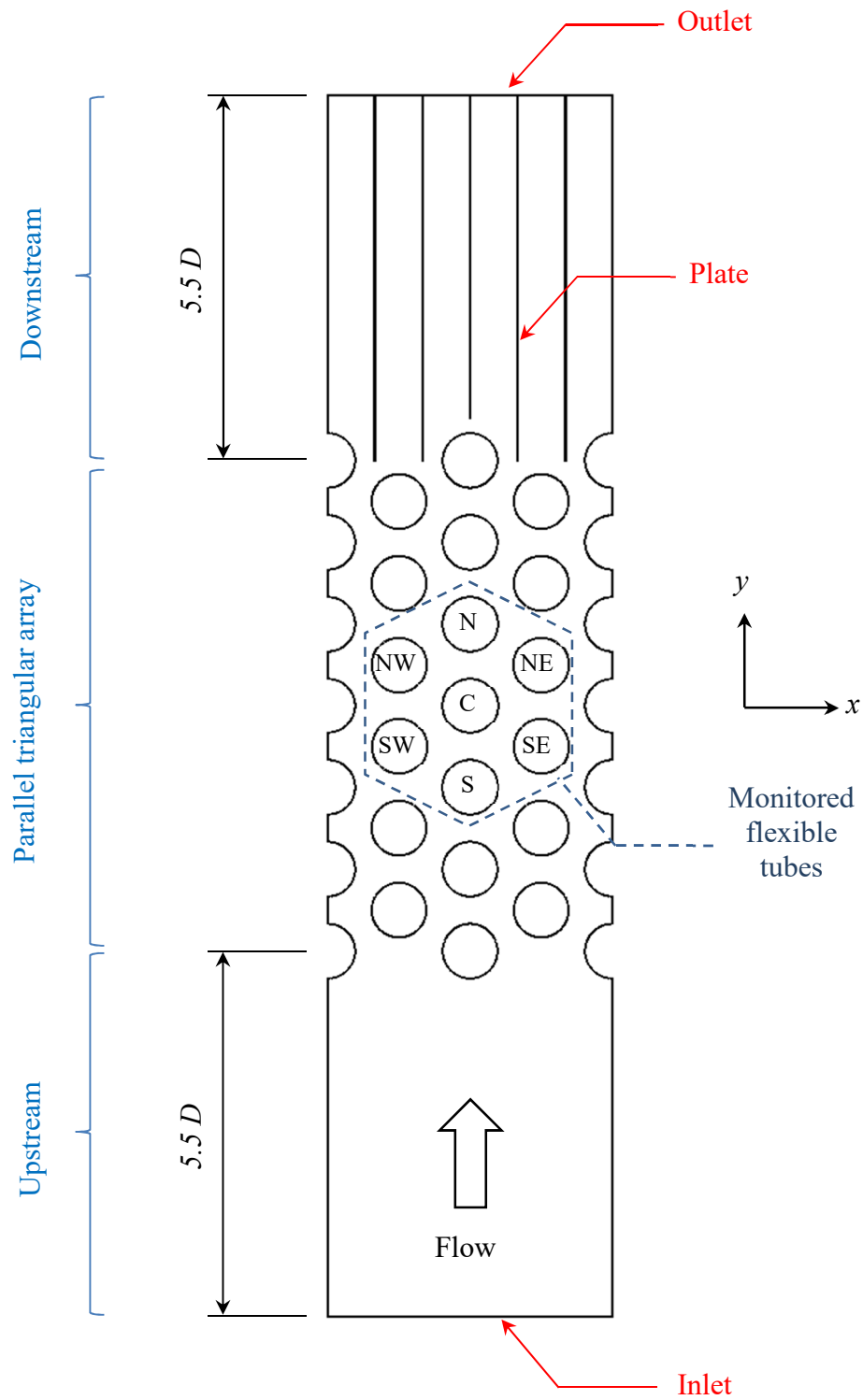


Figure 6.1: Flow domain

$$\frac{\partial}{\partial t}(\rho_m) + \nabla \cdot (\rho_m \mathbf{u}_m) = 0 \quad (6.1-a)$$

$$\begin{aligned} & \frac{\partial}{\partial t}(\rho_m \mathbf{u}_m) + (\mathbf{u}_m \cdot \nabla)(\rho_m \mathbf{u}_m) \\ &= \rho_m \mathbf{g} - \nabla P + \nabla \cdot (\mu_m (\nabla \mathbf{u}_m + (\nabla \mathbf{u}_m)^T)) + \nabla \cdot \left(\sum_{k=1}^n a_k \rho_k \mathbf{u}_{dr,k} \mathbf{u}_{dr,k} \right) \end{aligned} \quad (6.1-b)$$

$$\Phi_m = \sum_{k=1}^n a_k \Phi_k \quad (6.2)$$

The last term on the RHS of Eq. (6.1-b) represents the exchange of momentum between the phases and the mixture's average motion. The drift velocity $\mathbf{u}_{dr,k}$ is defined as the difference between a flow phase vector and the mixture velocity vector ($\mathbf{u}_k - \mathbf{u}_m$). This drift velocity can be estimated through algebraic relations of the drift-flux model; meanwhile, the mixture velocity \mathbf{u}_m is defined as in Eq. (6.3).

$$\mathbf{u}_m = \frac{\sum_{k=1}^n a_k \rho_k \mathbf{u}_k}{\rho_m} \quad (6.3)$$

Reynold's stresses are modeled through the implementation of the Spalart-Almaras turbulence model. This model solves a single transport equation for the eddy viscosity parameter. Such a parameter is then employed to calculate Reynold's stresses through Boussinesq's turbulent viscosity hypothesis. Sadek et al. (2020) have compared several RANS turbulence models in predicting fluidelastic forces in two-phase flows and suggested that Spalart-Almaras model consumes less computational power without sacrificing accuracy.

The void fraction distribution of a phase k is governed by a transport equation that accounts for the convection of such phase in the domain. In this study, the mixture is binary and consisted of air and water (gas and liquid phases, respectively). Therefore, these two phases do not exchange mass due to phase change. Moreover, a single transport equation for the air phase is sufficient to be solved to represent the distribution of both air and water in the domain since both phases must occupy 100% of the domain simultaneously.

6.2.3. Harmonic oscillator model

Each flexible tube is modeled as a lumped mass connected to a stationary reference via a linear spring and a linear damper for each direction of flexibility, as shown in Fig. 6.2. Such a system of flexible tubes can be represented by a linear system of second-order equations (Eq. (6.4)) where $M_{s,i}$, $C_{s,i}$, $K_{s,i}$ are the structural mass per unit length, damping coefficient per unit length, and stiffness per unit length of the i^{th} tube, while $[I]$, $\{z_i\}$, and $\{F_i\}$ are the identity matrix, generalized displacement vector for tubes, and external force vector per tube length acting, respectively. The model assumes that the tubes are structurally uncoupled. Thus, the coupling is only due to the two-phase flow between them.

$$M_{s,i}[I]\{\ddot{z}_i\} + C_{s,i}[I]\{\dot{z}_i\} + K_{s,i}[I]\{z_i\} = \{F_i\} \quad (6.4)$$

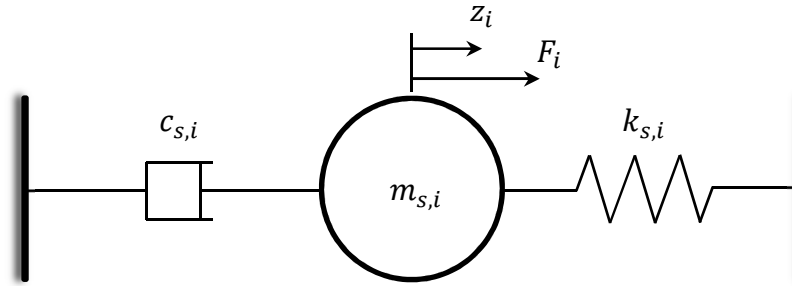


Figure 6.2: Structural harmonic oscillator model

The mass per unit length for each tube is set to be 3 kg/m . The structural stiffness can be related to the mass and natural frequency $f_{n,i}$ by Eq. (6.5-a) while the damping coefficient is related to the structural logarithmic decrement δ as shown in Eq. (6.5-b).

$$K_{s,i} = 4\pi^2 m_{s,i} f_{n,i}^2 \quad (6.5\text{-a})$$

$$C_{s,i} = \frac{4\pi m_{s,i} f_{n,i} \delta}{\sqrt{\delta^2 + 4\pi^2}} \quad (6.5\text{-b})$$

6.2.4. Flow/Structure coupling

The two-phase flow between the tubes leads to FEI occurrence if the critical flow velocity is attained. Based on the unsteady FEI model (Chen, 1987; Tanaka & Takahara, 1981) such coupling can be expressed as:

$$\{F_i\} = [M_{a,ij}]\{\ddot{z}_i\} + [C_{a,ij}]\{\dot{z}_i\} + [K_{a,ij}]\{z_i\} \quad (6.6)$$

The subscript a refers to the added effect of the flow on tubes' motion. The added mass M_a is a constant parameter that is mainly a function of tube location and array geometry (i.e., array's configuration and pitch-to-diameter ratio). On the other hand, the added damping and added stiffness parameters also vary with the flow velocity. If N tubes are flexible only in a single direction, then $[M_{a,ij}]$, $[C_{a,ij}]$, and $[K_{a,ij}]$ are $N \times N$ square matrices. The non-diagonal elements of such matrices (where $i \neq j$) represent the coupling flow added masses, damping coefficients, and stiffnesses between the tubes. All added elements can be calculated from fluidelastic force measurements as reformed from Chen (1987) in Eqs. (6.7):

$$M_{a,ij} = -\frac{\pi\rho_m D^2}{8} c_{ij} \cos(\phi_{ij}) \Big|_{\substack{Quiescent \\ flow}} \quad (6.7-a)$$

$$C_{a,ij} = \frac{\rho_m U_g^2}{2 \omega} c_{ij} \sin(\phi_{ij}) \quad (6.7-b)$$

$$K_{a,ij} = \rho_m U_g^2 \left(\frac{1}{2} c_{ij} \cos(\phi_{ij}) + \frac{4 \pi^2}{\rho_m D^2 U_r^2} M_{a,ij} \right) \quad (6.7-c)$$

where U_g is the gap flow velocity, and it is calculated from the free stream velocity U_∞ as $\frac{P/D}{P/D-1} U_\infty$, while U_r is its non-dimensional form $U_g/f_n D$. On the other hand, c_{ij} and ϕ_{ij} are the non-dimensional fluidelastic force coefficient and the corresponding force's phase angle, respectively. These two parameters are obtained by calculating the fluid force acting on tube i resulting from the forced oscillation to tube j with known amplitude and frequency. and measuring the induced fluid force. The force coefficient represents the magnitude of such measured force, while the phase angle is related to the lag/lead of induced force relative to the imposed motion. Several studies have been dedicated to measure forces either experimentally or numerically and report their values for different flow medium and array geometries (Elhelaly et al., 2020; Hassan et al., 2010; Hassan & Mohany, 2016; Inada et al., 1996; Olala & Mureithi, 2015; Sadek et al., 2018, 2020; Sawadogo & Mureithi, 2014; Tanaka & Takahara, 1981).

Equations (6.6) and (6.4) can be combined to form a characteristic equation for the coupled system as shown in Eq. (6.8-a) or its compact form Eq. (6.8-b):

$$[M_{s,i}[I] - M_{a,ij}]\{\ddot{z}_i\} + [C_{s,i}[I] - C_{a,ij}]\{\dot{z}_i\} + [K_{s,i}[I] - K_{a,ij}]\{z_i\} = 0 \quad (6.8-a)$$

$$[M]\{\ddot{z}_i\} + [C]\{\dot{z}_i\} + [K]\{z_i\} = 0 \quad (6.8-b)$$

Furthermore, Eq. (6.8-b) can be rewritten in its space form. This form represents an eigenvalue problem for the vector $\{q_i\}$, as shown in Eq. (6.9-a). Here, matrix $[A]$ is the state matrix of the dynamic system. The matrix $[A]$ and vector $\{q_i\}$ are related to the parameters in Eq. (6.8-b) as shown in Eq. (6.9-b) and Eq. (6.9-c), respectively.

$$\{\dot{q}\} = [A]\{q\} \quad (6.9-a)$$

$$[A] = \begin{bmatrix} [0] & [I] \\ -[M]^{-1}[K] & -[M]^{-1}[C] \end{bmatrix} \quad (6.9-b)$$

$$\{q_i\} = \begin{Bmatrix} z_i \\ \dot{z}_i \end{Bmatrix} \quad (6.9-c)$$

The solution of Eq. (6.9-a) results in N pairs of complex eigenvalue conjugates λ_i , where each pair is linked to a distinct vibration mode. Such pair is in the form of $\lambda_i = -\zeta_i \omega_i \pm j\sqrt{1 - \zeta_i^2} \omega_i$, where ω_i is the modal vibration frequency and ζ_i is its associated modal damping ratio. For each modal frequency λ_i there is an associated mode shape $\{Q_i\}$. Such a mode shape is often a complex value that can be represented in polar form as $\{r_i\}\angle\{\vartheta_i\}$, where $\{r_i\}$ represents the vibrational amplitude matrix and $\{\vartheta_i\}$ is phase angle shift associated with the time delay between the motion of tubes. As $\Re(\lambda_i) > 0$ the modal damping ζ_i becomes negative, and the associated vibration mode becomes unstable. Therefore, the FEI critical gap velocity $U_{g,cr}$ is defined as the minimum gap flow velocity at which $\Re(\lambda_i) = 0$. In literature, the flow velocity is often casted into its non-dimensional reduced velocity $U_r = U_g/f_n D$, where f_n is the nominal natural frequency of the array's tubes. In the case of untuned tubes, each tube has a deviated natural frequency from the nominal value, which is confusing for choosing the natural frequency basis for the reduced velocity. In this study, the array's nominal natural frequency is $f_n = 8 \text{ Hz}$ and the deviation in

natural frequency of untuned tubes will not exceed $\pm 10\% f_n$. Therefore, the nominal natural frequency will be used as the basis of reduced velocity in this study.

6.2.5. FEI mechanisms isolation

The isolations of the damping- or the stiffness-controlled mechanisms are possible by modifying the system's coupling matrix in Eq(8-a) since it carries the influence of both mechanisms. In the damping-controlled mechanism, the coupling of tubes is controlled by their oscillation velocity (Chen, 1983). Thus, the flow added damping coefficients $C_{a,ij}$ are the terms responsible for tubes oscillation velocity coupling. When these coefficients are discarded, such coupling will not materialize. The system will undergo instability only due to the stiffness mechanism, and hence the stiffness-controlled mechanism is isolated. In the same manner, the damping-controlled mechanism can be isolated by discarding the added flow stiffness coefficients $K_{a,ij}$ from the stiffness matrix $[K]$. The isolated characteristic equation for the damping- and stiffness-controlled mechanisms are shown in Eq. (6.10-a) and Eq. (6.10-b), respectively.

$$[M_{s,i}[I] - M_{a,ij}]\{\ddot{z}_i\} + [C_{s,i}[I] - C_{a,ij}]\{\dot{z}_i\} + [K_{s,i}[I]]\{z_i\} = 0 \quad (6.10-a)$$

$$[M_{s,i}[I] - M_{a,ij}]\{\ddot{z}_i\} + [C_{s,i}[I]]\{\dot{z}_i\} + [K_{s,i}[I] - K_{a,ij}]\{z_i\} = 0 \quad (6.10-b)$$

6.3. Results and discussions

In the U-bend region of a steam generator, the increase in tubes' curvature leads to an increase in tubes' span length in the outward radial direction, as seen in Fig. 6.3-a. This is translated into a decrease in tubes' natural frequency in the outward direction. A relation between the natural frequencies of a curved tube at level i and a radius of curvature R_i to any other tube at level $i + 1$ at a radius of curvature R_{i+1} can be derived as in Eq. (6.11). Thus, by applying Eq. (6.11) on the flexible 7-tube kernel shown in Fig. 6.1, and considering that tube N lies at the kernel's outward location (Fig. 6.3-b), a detuning pattern can be obtained as shown in Table 6.1. The detuning multiplier DM is a parameter used to control detuning while maintaining the same detuning pattern, which is defined in Eq. (6.12). This parameter controls the difference of the radius of curvature, $R_{i+1} - R_i$, between any two tubes with R_i and R_{i+1} as a ratio to the actual spacing between the

tubes defined by the pitch-to-diameter ratio and tube's diameter. Therefore, by considering tube C as a reference tube at level i , a DM value of 0 means no frequency detuning between tube C and the other tubes in the kernel. In contrast, a value of 1 indicates that the detuning amount is equal to what exists for a curved tube bundle at the given pitch-to-diameter ratio and tube diameter. Any value of DM higher than unity is a theoretical exaggeration of the detuning level in the array.

$$\frac{f_{n,i+1}}{f_{n,i}} = \left(\frac{R_i}{R_{i+1}} \right)^{1.5} \quad (6.11)$$

$$DM = \frac{R_{i+1} - R_i}{\frac{1}{2} \frac{P}{D} \times D} \quad (6.12)$$

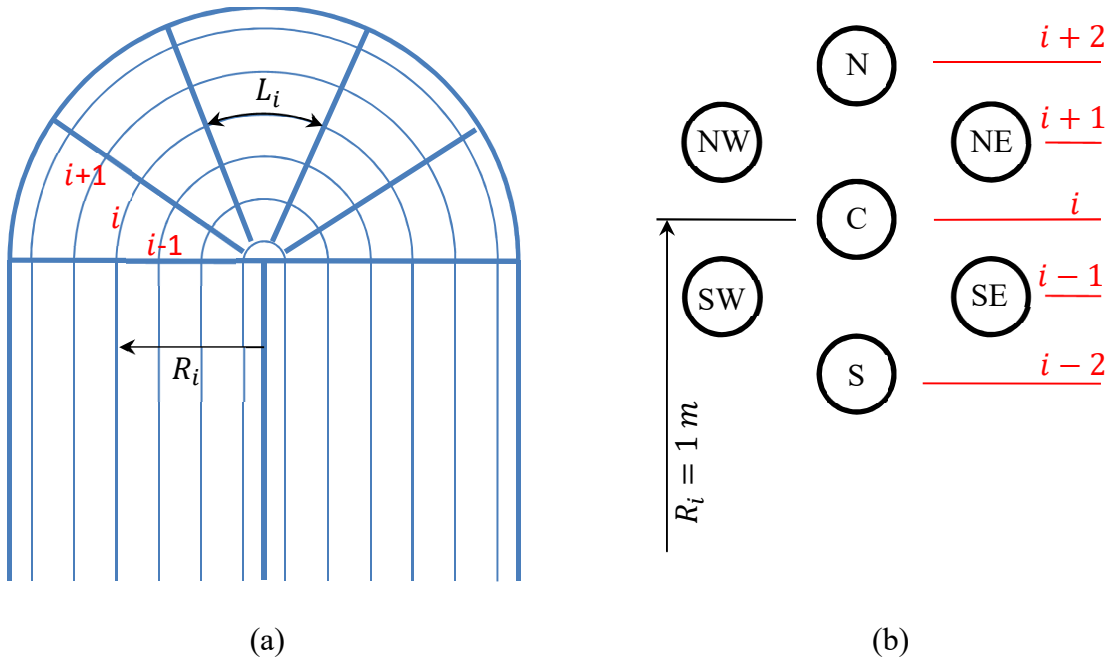


Figure 6.3: Sketch of the U-bend region in a steam generator showing the gradual increase in tube span L_i in the outward radial direction.

The prominence of the frequency detuning effect on the FEI stability threshold has been linked to the prevailing FEI stiffness mechanism. If the damping mechanism controls the FEI mechanism, the system will be less sensitive to frequency detuning and vice versa for the stiffness mechanism. However, it is not necessarily that one mechanism to be dominant. In such a case, the effect of

frequency detuning may not be clearly anticipated. Therefore, the analysis represented focuses on investigating the effect of detuning for each mechanism in the different cases of transverse and streamwise FEI.

Table 6.1: Deviation percent of each tube's natural frequency from the nominal 8 Hz value for the studied parallel triangular array. $D = 38 \text{ mm}$ and $P/D = 1.5$.

DM#	N	NE, NW	C	SE, SW	S
0	0%	0%	0%	0%	0%
0.25	-2.1%	-1.06%	0%	1.08%	2.18%
0.5	-4.13%	-2.1%	0%	2.18%	4.43%
0.75	-6.09%	-3.12%	0%	3.29%	6.77%
1	-7.98%	-4.13%	0%	4.43%	9.2%

6.3.1. Transverse FEI

To benchmark the effect of frequency detuning according to the detuning pattern proposed, a stability threshold map of a tuned case for transverse FEI is shown in Fig. 6.4. The change of air void fraction generally affects the mixture density as well as the fluidelastic forces. The available fluid elastic force data in literature covered a range of air void fractions from 0% up to 90% (Sadek et al., 2018, 2020; Sawadogo & Mureithi, 2014), which showed that fluid elastic forces are insensitive to air void fraction. Therefore, the two-phase flow effect can be approximated by varying the mixture density ρ_m , without a severe sacrifice of accuracy, in the mass-damping parameter expression ($MDP = \frac{m_s \delta}{\rho_m D^2}$). Although the implementation of this assumption can be less accurate at higher air void fraction, it is extended up to 100% air void fraction (air flow). This was done to provide more insight into FEI mechanisms' interaction. This limit corresponds to mass-damping parameter values of 12.33. Moreover, the range has been extended to $MDP = 1000$, as shown by the shaded area, to provide a broader view into the involved FEI mechanisms. This is done by artificially reducing the mixture density to smaller values less than air's density. The stability map shows the stability threshold curves for the isolated damping mechanism, isolated stiffness mechanism, and both damping and stiffness mechanisms combined as calculated using

Eq. (6.10-a), Eq. (6.10-b), and Eq. (6.8-a), respectively. From the figure, it is evident that in the case of a flexible kernel in the transverse direction, FEI is controlled by the damping mechanism for low mass-damping parameter values, $MDP \leq 1$, after which the interaction between damping and stiffness mechanisms becomes dominant up to $MDP = 20$. Such interaction provides a less stable system than each isolated mechanism alone. For higher mass-damping parameter values, the damping mechanism's effect diminishes severely, and stiffness becomes the controlling mechanism.

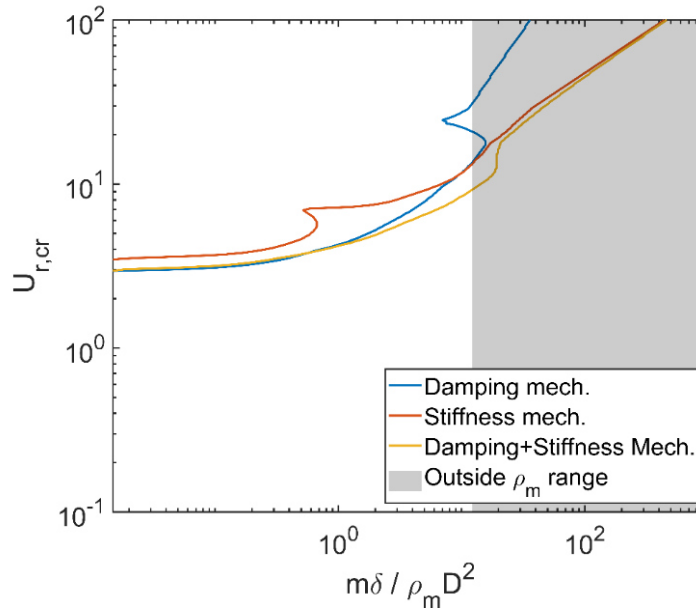


Figure 6.4: Stability map due to different mechanisms for a flexible kernel in the cross-flow direction (x-dir.). No detuning applied ($DM = 0$).

Figure 6.5 shows the modal-to-nominal natural frequency ratio change of the unstable vibration mode for the three cases of damping, stiffness, and combined damping and stiffness mechanisms. At low mass-damping range ($MDP < 1$) the modal frequency of the damping mechanism is lower than the stiffness counterpart. At the same time, it is slightly less for the combined damping and stiffness mechanisms case than the damping mechanism value. Hassan and Weaver (2016) has reported in their analysis that in a case of concurrent transverse and streamwise flexibility, the system will undergo instability in the direction of the least natural frequency. Despite that instability in these directions was known to occur due to different mechanisms (Mureithi et al., 2005; Nakamura et al., 2014), it will be more conservative to limit such criterion to the case of different FEI directions as the focus in this study is given to a particular FEI direction at a time. It

can be seen from Fig. 6.5 that the modal frequency of the damping mechanism is lower than that of the stiffness mechanism within the low mass-damping parameter zone. Moreover, as the mass-damping parameter increases above unity, the modal frequency of both isolated mechanisms as well as their combination approach very closely to the nominal natural frequency. This is more evident in the high *MDP* zone, where the stiffness mechanism is dominant. In such *MDP* range the stiffness mechanism provides a significantly lower instability threshold than the damping mechanism.

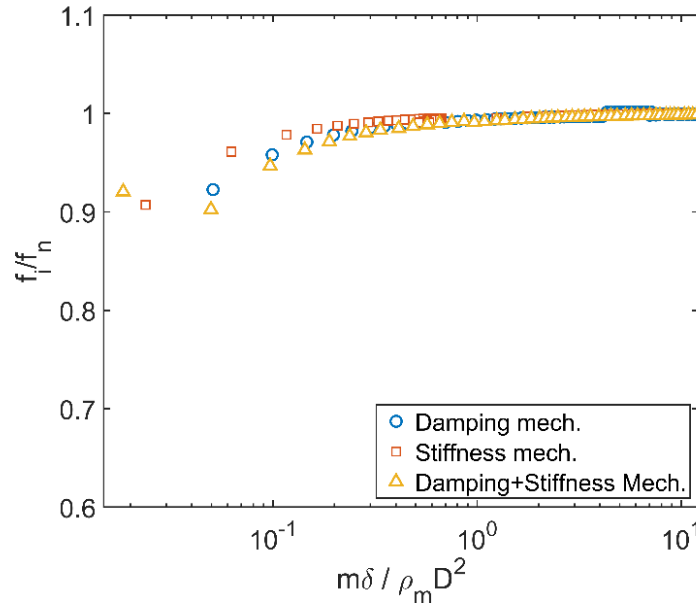


Figure 6.5: Modal-to-natural frequency ratio due to two different mechanisms for a flexible kernel in the cross-flow direction (*x*-dir.). No detuning applied (*DM* = 0).

Since the differences between the modal frequencies for each mechanism's most unstable mode are minimal (i.e., within 5%), the associated mode shapes are also investigated, as shown in Fig. 6.6. Although the tubes are only oscillating in a single direction, an elliptical orbit representation is used to produce an accurate depiction of the tube's position in a single cycle of vibration. Two mass-damping values of 1 and 5 are selected, representing a value on the border of the damping-controlled region and another inside the combined damping and stiffness-controlled region, respectively. Tube C was taken as a reference for both amplitude r_i and motion's phase angle ϑ_i . At *MDP* = 1, the vibrational mode shape associated with the damping mechanism, as shown in Fig. 6.6-a, is similar to the combined damping and stiffness mechanisms in Fig. 6.6-e.

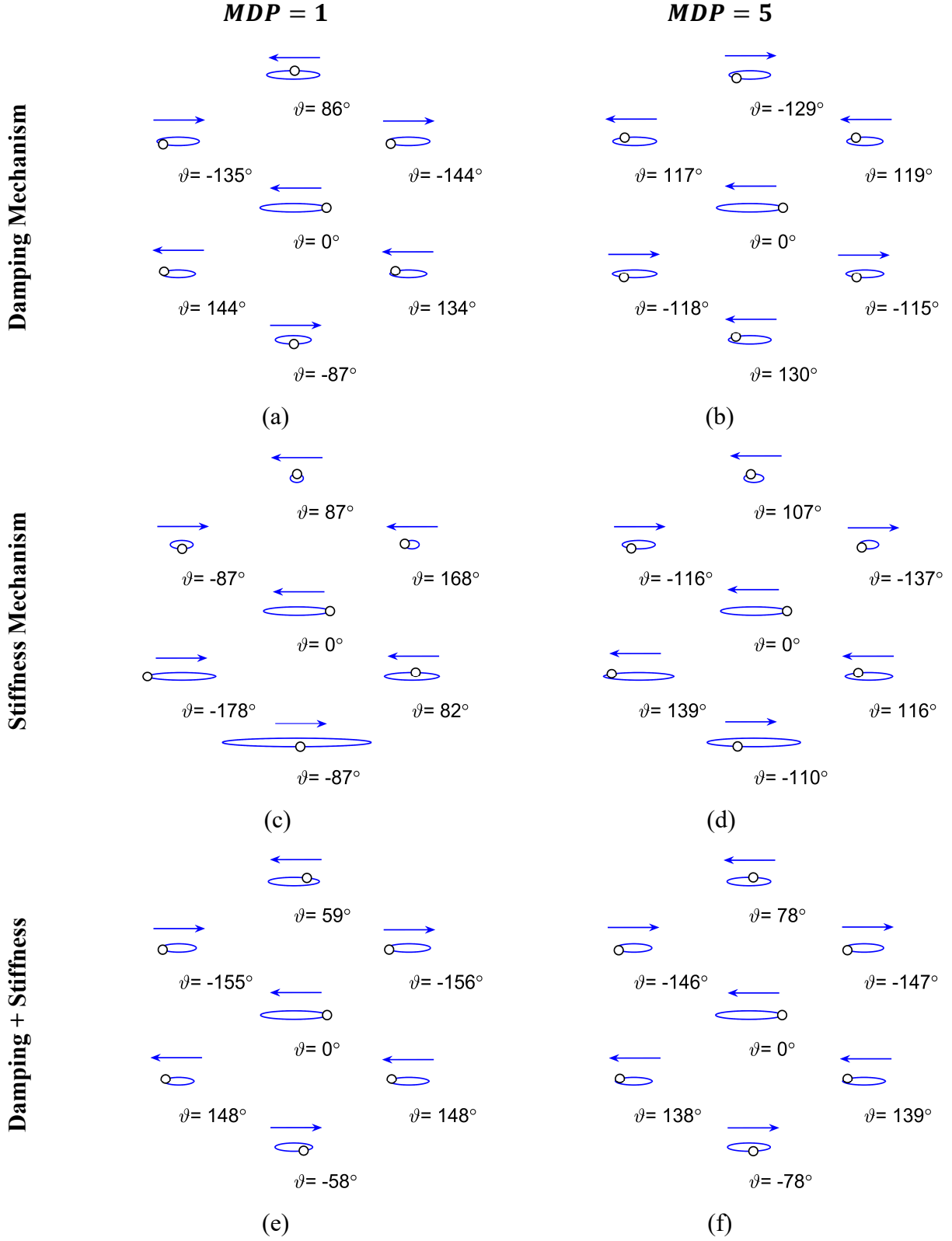


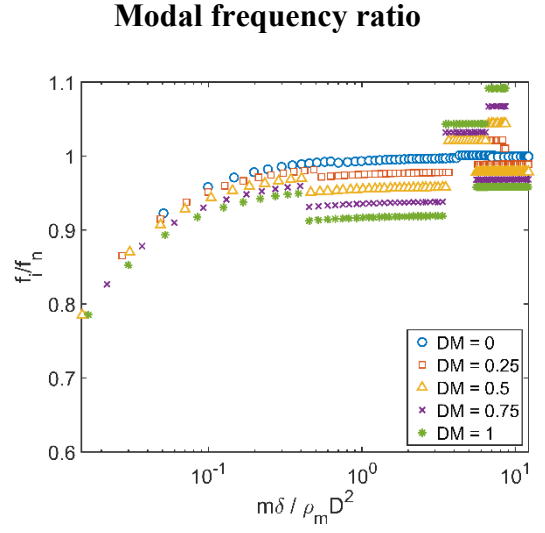
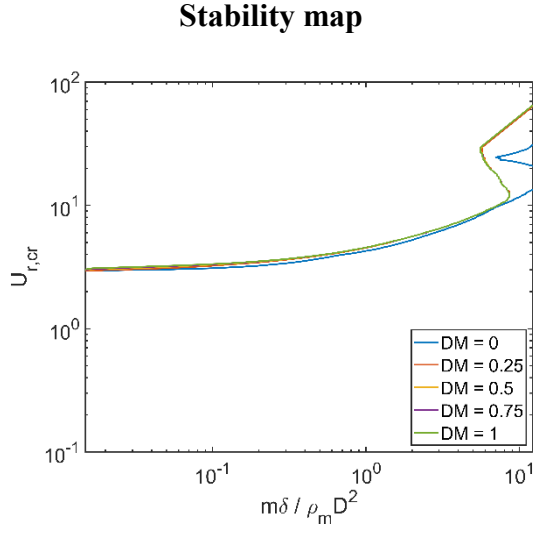
Figure 6.6: Mode shapes at the onset of transverse FEI at $MDP=1$ & 5 for the three cases of: a,b) damping mechanism, c,d) stiffness mechanism, and e,f) damping and stiffness mechanisms combined. No detuning applied ($DM = 0$)

The stiffness mechanism provided a distinctly different mode shape, as shown in Fig. 6.6-c, especially in terms of the phase angle ϑ_i . This supports the early finding from Fig. 6.4 that the damping mechanism controls the FEI at such mass-damping parameter.

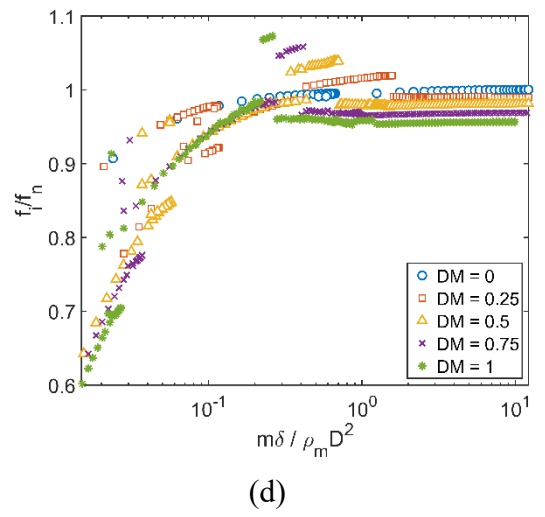
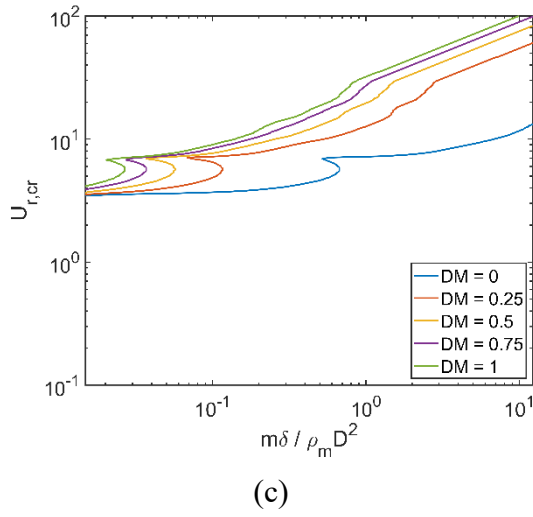
On the other hand, the damping mechanism's mode shape in the combined damping and stiffness-controlled region ($MDP = 5$) changes drastically, as shown in Fig. 6.6-b. Surprisingly, this does not result in a distinct change in the mode shape for the combined damping and stiffness mechanisms seen in Fig. 6.6-f. In fact, this mode shape generally remained unchanged between the two mass-damping values. Moreover, the mode shape linked to the stiffness mechanism shown in Fig. 6.6-d drastically changes to become similar to the combined damping and stiffness mechanism case. This emphasizes the complexity of the interaction between the different FEI mechanisms in the damping- and stiffness-controlled FEI region.

Next, the effect of frequency detuning is investigated on each mechanism scenario for transverse FEI, as shown in Fig. 6.7. Such an effect is prominent on the stability threshold of the stiffness mechanism in Fig. 6.7-c. It can be noticed that the effect is less pronounced with the increase of frequency detuning (the detuning multiplier DM) and the increase of stability threshold diminishes with more detuning. Surprisingly, on the other hand, the frequency detuning has less effect on the stability boundary at the lower mass-damping parameter than at the higher end. On the other hand, from Fig. 6.7-a, the damping mechanism is barely affected by frequency detuning for all $MDP < 5$, after which a sudden jump in the stability threshold occurs relative to the tuned case ($DM = 0$). Such effect was identical for all detuned cases. It is worth noting that structural stiffness remains an essential part of the isolated damping mechanism, as shown in Eq. (6.10-a). Such an effect suggests that structural stiffness becomes a more critical parameter at high mass-damping parameter values. Similar to the isolated damping mechanism, the effect of frequency detuning in the combined mechanism in Fig. 6.7-e is minimal up to $MDP < 5$. Then, a sudden jump in the stability threshold occurs. However, the detuning multiplier effect is observed in stabilizing the array in similar behavior to the isolated stiffness mechanism. This falls within $1 < MDP < 20$, where interaction between damping and stiffness mechanisms occurs, as discussed earlier.

Damping Mechanism



Stiffness Mechanism



Damping + Stiffness

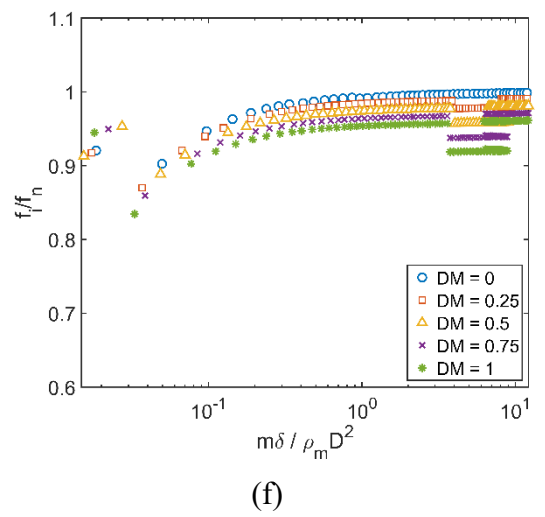
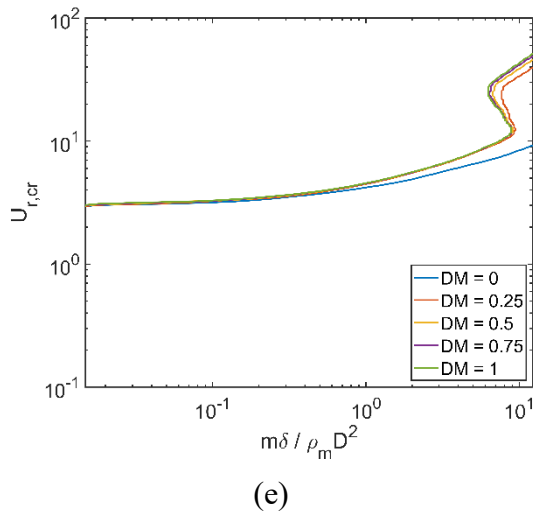


Figure 6.7: Effect of frequency detuning on the cross-flow (x -dir) FEI Mechanisms: a, c, e) stability map; b, d, f) modal frequency ratio. Detuning increases with detuning multiplier DM .

Figure 6.8 provides a clearer picture of such interaction between the mechanisms and the detuning multiplier. The variation of the stability threshold with DM is extracted at $MDP = 10$ for all three cases of the mechanism. While the variation in the stability threshold of the damping mechanism reaches a plateau after $DM = 0.25$ (Fig. 6.8-a), the stiffness mechanism is more affected by a higher detuning amount. However, this effect is not linear and diminishes at higher detuning (Fig. 6.8-b). By combining the two mechanisms, as shown in Fig. 6.8-c, the stability threshold exhibits very minimal dependency on detuning after $DM = 0.25$, similar to the damping mechanism case.

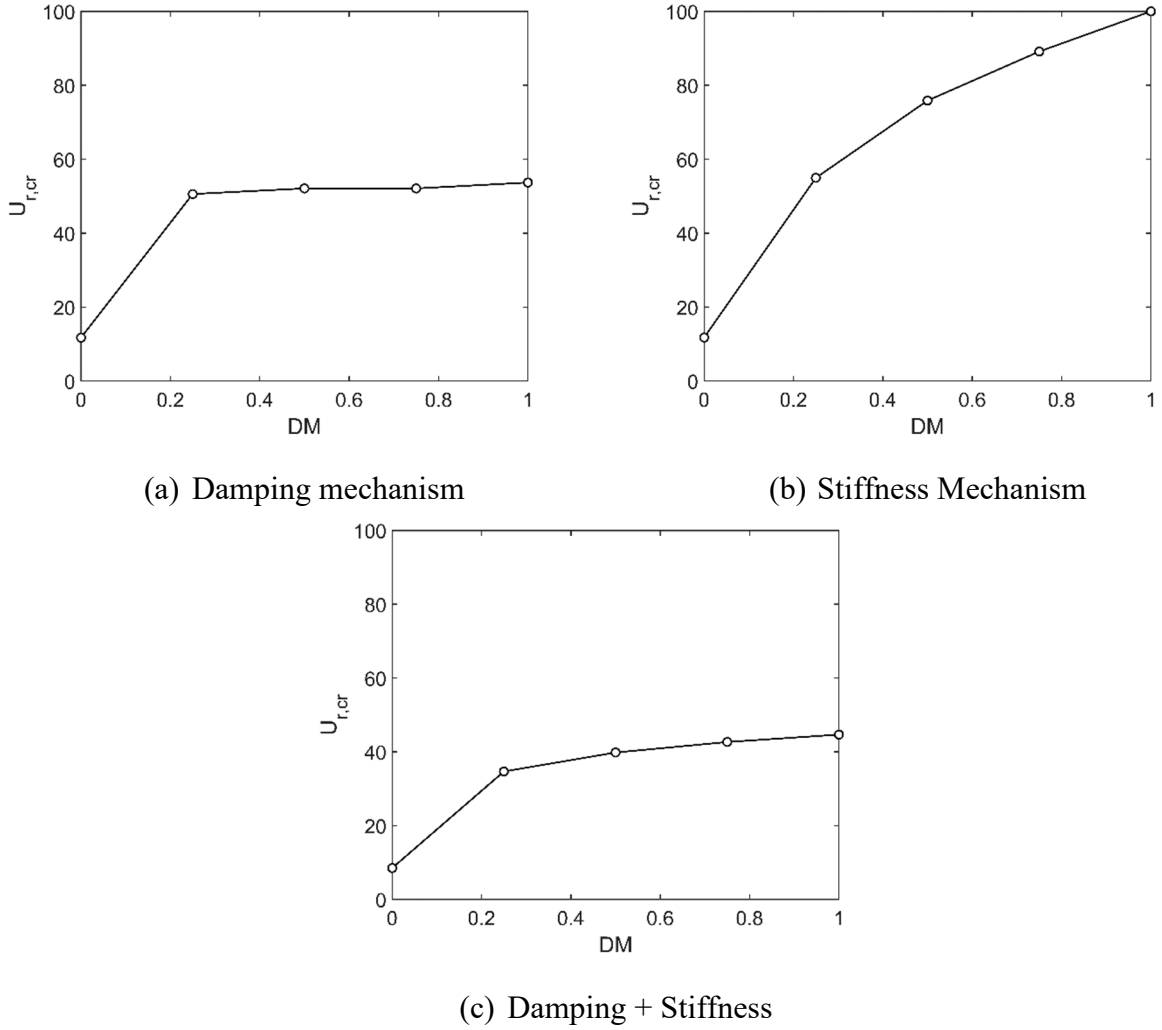


Figure 6.8: Effect of frequency detuning on the cross-flow (x -dir) FEI stability threshold at $MDP = 10$: a) damping mechanism, b) stiffness mechanism, and c) damping+stiffness mechanisms.

This is similar to experimental observations of Weaver and Koroyannakis (1983). The observed high dependency on the mass-damping parameter can be linked to flow coupling strength between

tubes. At high-density flows (e.g., water), the flow-added terms are more considerable than lighter flows (e.g., air); this results in a stronger FEI coupling at small air void fractions and less stability threshold. Moreover, for light flows, the added flow stiffnesses become lower compared to the structural stiffness. This makes the structural stiffness more dominant; hence the effect of detuning becomes more evident in the FEI stability threshold.

Modal frequency is also being investigated for the frequency detuning effect on the three aforementioned mechanism cases, as shown in Figs. 6.7-b, 6.7-d, and 6.7-f, respectively. At a mass-damping parameter lower than 0.4, the effect of added mass is noticeable in reducing the modal frequency for all cases. At such a range, the mass of the displaced fluid, mostly water, is comparable to the tube's mass, which increases the equivalent mass and reduces the modal frequency. Moreover, the increase of frequency detuning level for the studied detuning pattern results in a reduction in the unstable mode shape's modal frequency. The studied detuning pattern involved fixing tube C's natural frequency and reducing the natural frequency of tubes N, NE, and NW while increasing the natural frequency of tubes S, SE, and SW by the same level. This may indicate that the unstable mode frequency is controlled by the tube of the least frequency.

For the isolated damping mechanism case in Fig. 6.7-b, an abrupt fall in the modal frequency took place. In such events, the most unstable mode switches to another mode of a less modal frequency. This occurs in the mass-damping parameter range between 0.4 and 4. In such range, the critical reduced velocity begins to increase at a higher rate compared to $MDP < 0.4$, as shown in Fig. 6.7-a. Such reduction in frequency is followed up by jumps to high frequencies between mass-damping parameter values of 4 and 9. These higher modes result in the abrupt increase in the stability threshold at the same mass-damping range, as shown in Fig. 6.7-a. Similar observations can be drawn for the modal frequency of isolated stiffness mechanism in Fig. 6.7-d and the combined damping-stiffness mechanisms in Fig. 6.7-f. Unlike the damping mechanism, more jumps in the modal frequency and unstable mode changes are observed at the low-end of the mass-damping parameter, where the damping mechanism dominates transverse FEI.

6.3.2. Streamwise FEI

The frequency detuning effect is also investigated for the streamwise FEI in this analysis. The structural logarithmic decrement δ is set to 0.176. A benchmark case of no detuning ($DM = 0$) is depicted in Fig. 6.9. The streamwise stability map is shown in Fig. 6.9-a for the three cases of FEI mechanisms. It is evident that the streamwise FEI is controlled by the stiffness mechanism for $MDP > 2$ (81% air void fraction). In literature, streamwise FEI was never observed experimentally for a single flexible cylinder (Mureithi et al., 2005; Nakamura et al., 2014), suggesting that motion intercoupling between tubes is essential for FEI to occur in this direction, and hence streamwise instability is controlled by stiffness mechanism. On the contrary, Hassan and Weaver (2016) numerical analysis predicted that a single flexible tube might undergo a streamwise FEI at very high reduced velocity ($U_r > 120$). This current analysis reveals that the occurrence of damping controlled FEI remains a possibility in the streamwise direction at high reduced velocity. Moreover, at a low mass-damping parameter less than 2, the general instability threshold is controlled by the interaction between damping and stiffness mechanisms. This conclusion can also be extracted from Fig. 6.9-b for modal frequencies. At such a low mass-damping parameter range, the modal frequency ratio for the combined damping-stiffness mechanisms is constant and equal to the nominal array frequency. In contrast, it is predicted to be 20% less for the stiffness mechanism and more than 50% higher for damping mechanisms.

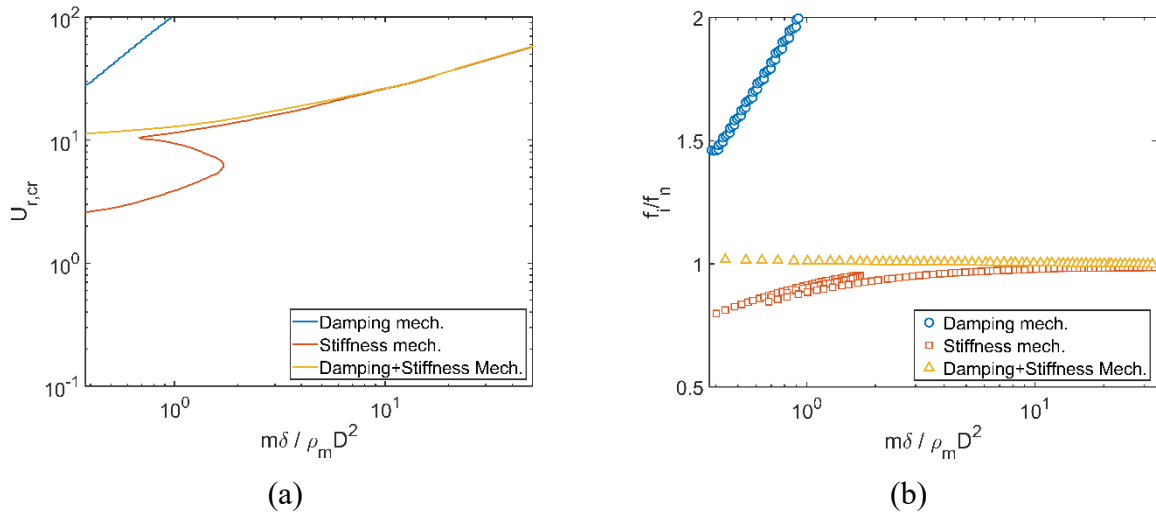


Figure 6.9: Stability map and modal frequency ratio due to two different mechanisms for a flexible kernel in the streamwise direction (y-dir.). No detuning applied ($DM = 0$).

Such high modal frequency of the damping mechanism is attributed to the positive flow-added damping, which increases the total damping and provides stability to a single tube (Sadek et al., 2020). Therefore, the damping mechanism's stability threshold is due to a higher vibration mode, which is controlled by the negative flow-added cross-coupling damping between the tubes. These differences in modal frequency are significant compared to transverse FEI in Fig. 6.5 for the same mass-damping parameter range. Hence, there is a strong interaction between the two mechanisms in the *MDP* range.

The same conclusion can be drawn from the associated mode shape to each of the mechanism cases, as shown in Fig. 6.10. The three mode shapes were extracted for water flow at $MDP = 0.38$ in the region where both damping and stiffness mechanisms are interacting and responsible for the loss of instability. The mode shape of such a case is shown in Fig. 6.10-c. This mode shape is the same as what was experimentally observed for 80% air void fraction ($MDP = 1.9$) by Violette et al. (2006) and later confirmed numerically by Sadek et al. (2020) based on the model presented in this study. The same mode shape is also found at a higher mass-damping value of 3.9 (90% air). At such a high value, the FEI is controlled by the stiffness mechanism according to Fig. 6.9-a. All three mechanisms are found to have similar mode shapes, unlike at lower mass-damping parameter where the interaction between the mechanisms determines the FEI. For example, by comparing the mode shapes in Figs. 6.10-a and 6.10-b, at $MDP = 0.38$, between the damping and stiffness mechanisms, the tubes NE, NW, SE, and SW are all out-of-phase with their corresponding counterparts. In fact, the mode shape of the combined damped and stiffness mechanisms' case is similar to the one of the damping mechanism. Moreover, it was noticed that by increasing the mass-damping parameter, the stiffness mechanism's mode shape approaches the one shown in Fig. 6.10-c, and streamwise FEI becomes purely stiffness-controlled.

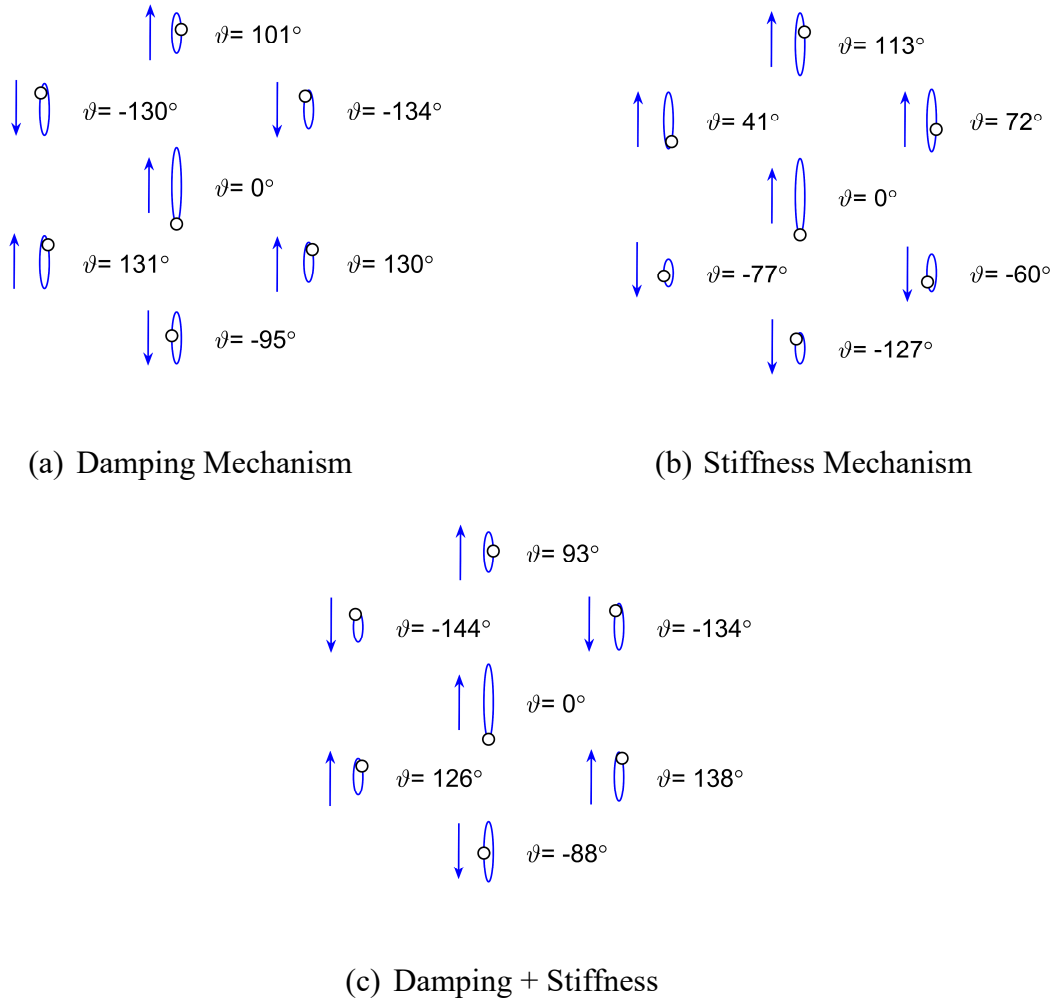
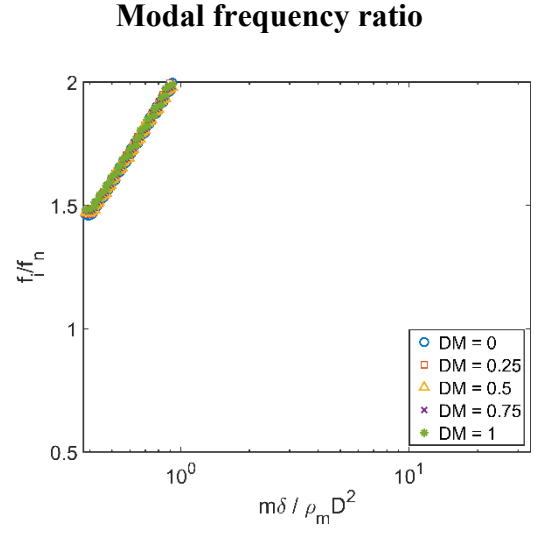
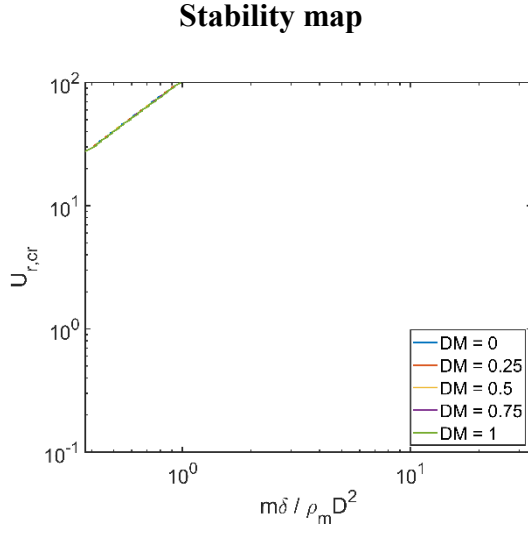


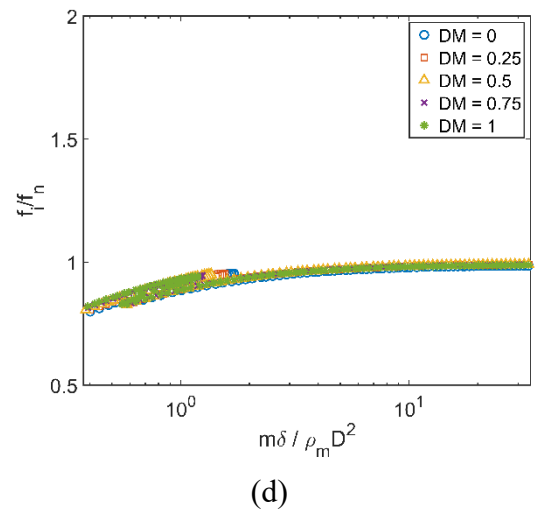
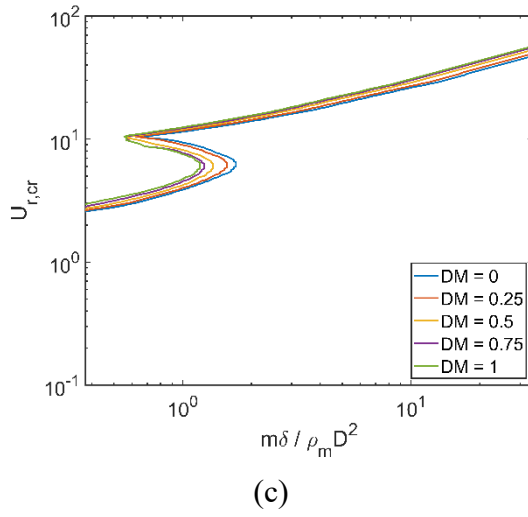
Figure 6.10: Mode shapes at the onset of transverse FEI at MDP= 0.38 (water flow) for the three cases of: a) damping mechanism, b) stiffness mechanism, and c) damping and stiffness mechanisms combined. No detuning was applied ($DM = 0$).

The frequency detuning effect is also studied for streamwise FEI, as presented in Fig. 6.9. The case of isolated damping mechanism is presented in Figs. 6.11-a and 6.11-b for FEI stability threshold and modal frequency ratio, respectively. In such a case, the frequency detuning does not affect the damping mechanism for the studied range of the mass-damping parameter. It does not change either of FEI stability threshold or modal frequency ratio. This is different from the transverse FEI, which showed a marginal dependency on frequency detuning level, specifically when damping and stiffness mechanisms interact.

Damping Mechanism



Stiffness Mechanism



Damping + Stiffness

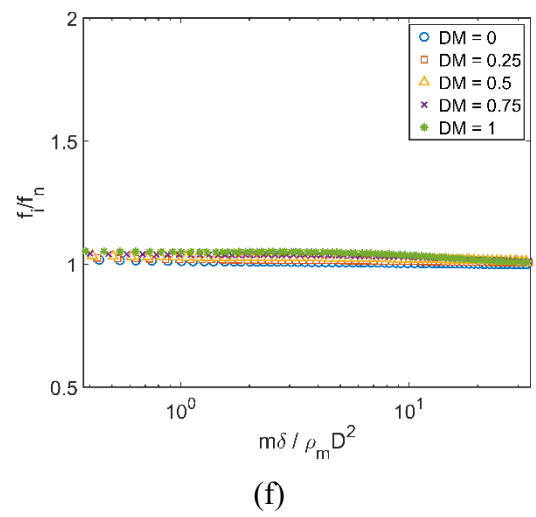
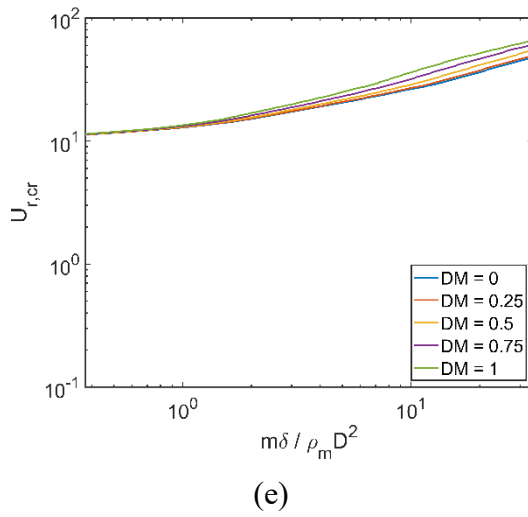


Figure 6.11: Effect of frequency detuning on the streamwise (y -dir) FEI Mechanisms: a, c, e) stability map; b, d, f) modal frequency ratio. Detuning increases with detuning multiplier DM .

On the other hand, the effect of frequency detuning is detectable on the stiffness mechanism, as shown in Fig. 6.11-c. However, it is less sensitive to detuning compared to the transverse FEI counterpart. Though similar to what was observed in Fig. 6.7-c, the detuning increase still does not elevate the stability proportionally. It seems that there is a limit to benefit from the increase of system stability. By moving to the combined case of damping and stiffness mechanisms in Fig. 6.11-e, such finding is less observable. Increasing the detuning has more potential to increase the system's stability, more certainly at high mass-damping parameter (potentially airflow). When the flow is mostly water, FEI stability is almost insensitive to detuning. It is apparent that there is an interaction between the damping and stiffness mechanisms for water flow, which reduces the sensitivity to frequency detuning.

6.4. Conclusion

The FEI is a complex phenomenon that has been investigated for decades. In this study, the frequency detuning effect was investigated numerically on FEI in transverse and streamwise directions. A seven-tube classical flexible kernel representing a parallel triangular array of 1.5 pitch-to-diameter ratio was implemented and subjected to an air-water flow mixture. A stability analysis was performed based on the unsteady model of fluidelastic instability. The performed analysis isolated the damping and stiffness mechanisms and studied the frequency detuning effect on each one separately. Moreover, a complete overview of the frequency detuning effect on stability threshold under both mechanisms combined was also investigated.

Frequency detuning may occur due to manufacturing tolerance or the curvature and geometrical constraints of the tubes in the steam generator's U-bend region. The latter case was the focus of this study. A specific detuning pattern with various detuning levels up to 10% of the nominal natural frequency was applied to the kernel. Mass-damping parameter plays a critical role in controlling such effect for transverse and streamwise FEI. For dense fluids, like water, frequency detuning has little to no effect on the stability threshold.

On the other hand, for lighter fluids, like air, the detuning may substantially increase the stability threshold. This agreed with experimentally reported data in the literature. Unlike an intuitive thought that frequency detuning has a drastic impact on the stiffness mechanism, this observation did not depend on a particular mechanism, especially for transverse FEI. In such a case, the

detuning had a noticeable effect on both the damping and stiffness mechanisms for airflow. Although, in reality, the flow's added stiffness and damping couplings are indivisible, the mass-damping parameter controls how the realistic stability threshold line is affected by each mechanism under the detuning case. This was also confirmed for streamwise FEI.

The modal frequency of the most unstable mode shape was also studied against frequency detuning. The modal frequency's behavior was found to be highly dependant on FEI direction. For transverse FEI, increasing the level of detuning resulted in a proportional decrease in modal frequency. This was very distinct at large mass-damping values. On the contrary, detuning seemed to have an insignificant impact on modal frequency in the case of streamwise FEI. The isolated damping and stiffness mechanisms were also affected in the same manner by frequency detuning for each FEI direction. Therefore, FEI mechanisms are not responsible for such observation. Other parameters, such as structural damping, may play a role. Though such a conclusion should be limited to the studied detuning pattern, and more investigations are needed.

Chapter 7. Summary and Conclusions

7.1. Thesis summary

The modelling of the fluidelastic instability phenomenon in an air-water two-phase mixture was achieved. This research focused on the parallel triangular array since it is the most prone to the fluidelastic instability. The implemented model was based on the Computational Fluid Dynamic (CFD) to simulate the two-phase flow within the tube array. The two-phase drift-flux mixture model was selected to model the two-phase nature of the flow. On the other hand, the flow-structural coupling was carried it via two numerical techniques: 1) a direct flow/structural coupling where the instantaneous flow forces acting on each cylinder are resolved in the time-domain. Then, the forces were integrated into a harmonic oscillator model to calculate its motion's response of each flexible tube and continuously update the flow field. This method establishes a two-way coupling between the flexible structure and the flow. 2) A hybrid analytical-flow model where the coupling is performed by analyzing the periodic fluidelastic forces obtained from CFD simulations and extract the flow added mass, damping and stiffness parameters according with the fluidelastic instability's unsteady model. Although this approach only establishes a one-way coupling between the flow and the flexible structure, it facilitated an in-depth investigation of the phenomenon under different structural and flow conditions. Therefore, this model was implemented in chapters 5 and 6 in the study of flow approach angle and the tubes' frequency detuning effects on the onset of fluidelastic instability, respectively. Detailed descriptions of the used model, numerical techniques, and implementations were provided in chapters 3 and 4.

This research utilized a 2-dimensional spatial domain to simulate the fluidelastic instability phenomenon. The obtained results were validated and verified against experimental data for void fraction distribution, air bubbles' velocity, onset of fluidelastic instability, and fluidelastic force magnitudes and phase angles. The latter two parameters were validated for the fluidelastic instability in both transverse (normal to mean flow) and streamwise (parallel to mean flow) directions and showed good agreement. For the studied and validated cases of fluidelastic instability, the model showed that the air void fraction has an insignificant effect on the fluidelastic

force coefficients and phase angles up to 95% air, which agreed with a published experimental data.

The effect of flow approach angle on the onset of fluidelastic instability was investigated. This was carried out by gradually rotating the tube array relative to the flow direction from a parallel triangular array to normal triangular array. At each angle, the fluidelastic forces acting on the flexible tubes were extracted and analyzed. Based on the visualized time-averaged flow pattern between the tubes at each array's angle, an approximate semi-analytical model was successfully developed to predict the fluidelastic forces' magnitudes and phase angles at any flow approach angle. Such model was able to predict the forces acting on any tube at any two orthogonal directions (e.g. transverse and streamwise). The model only requires the pre-knowledge of the fluidelastic force data for any two orientation angles of a particular array. Such information is already available in the literature for the square and triangular arrays. The results obtained from the approximate semi-analytical model have been compared and validated against the fluidelastic forces

Moreover, a novel analysis is pursued to study the fluidelastic instability and the effect of frequency detuning on its onset. A special detuning pattern was employed which reflects the effect of tubes curvature in the U-bend region, and the level of detuning was controlled by an introduced detuning multiplier. The analysis was based on numerically isolating the each of the damping and stiffness-controlled mechanisms and investigating the contribution of each mechanism to the total instability. Such isolation is not possible experimentally. With the variation of air void fraction was incorporated in the dimensionless mass-damping parameter, the analysis showed that frequency detuning tends to stabilize the tubes specially at high values of the mass-damping parameter. However, such effect is more pronounced for the stiffness-controlled mechanism, and it is barely noticed for damping-controlled mechanism.

Finally, the work presented in this thesis provides a method to predict the onset of fluidelastic instability for any tube geometry which can be relied on in the design of steam generators.

7.2. Conclusions

The following conclusions can be drawn from the study and analyses presented in this research:

1. The use of the drift flux mixture model was adequate to simulate the interactions between the air and water phases within the tube array.
2. Air void fraction had a minimal effect on the fluidelastic forces acting on the tubes in the triangular array up to 95%. Furthermore, a drastic effect was noticed between 99% and 100% air.
3. The onset of fluidelastic instability was predicted in the transverse and streamwise directions, which agreed with data in the literature.
4. The pitch-to-diameter ratio effect on the fluidelastic forces and the onset of instability were investigated. It was found that for pitch-to-diameter ratio less than 1.5, the phase angle is highly affected by the pitch-to-diameter ratio, while at values higher than 1.5 the effect is more observed on the magnitude of the magnitude of the force coefficients.
5. The time-averaged flow pattern within the triangular tube array can approximated as a linear combination of the flow patterns occur in the parallel and normal triangular arrays.
6. For every flow approach angel in a triangular array, the flow can be decomposed into its standard normal and parallel flow pattern components. Then the fluidelastic forces at every approach angle can be fully reconstructed from the known fluidelastic data of these standard orientations in the literature.
7. The frequency detuning of tubes in the parallel triangular array is found to stabilize the system against fluidelastic instability.
8. The effect of frequency detuning is highly dependent on the mass-damping parameter and the fluidelastic mechanism in control. At high values (air flow), such effect is highly pronounced. On the other hand, for low mass-damping parameter (water flow) the effect is much less observed.
9. The analysis introduced a procedure to numerically isolate the stability threshold produced by either damping or stiffness mechanisms.
10. The damping-controlled mechanism is on affected by the frequency detuning (in the increase in system's stability) at high mass-damping parameter, while the stiffness-controlled mechanism is affected regardless of the mass-damping value.
11. In transverse fluidelastic instability, the fluidealstic mechanism which produces a lower stability threshold becomes dominant. For example, the damping-controlled mechanism is dominant up to mass-damping of 1 and stiffness-controlled mechanism becomes dominant

for mass-damping larger than 20. In the range between 1 and 20, both mechanisms provide a similar stability threshold limit. Thus, both mechanisms contribute to the instability. In such range the stability limit is lower than what is predicted by each mechanism.

12. Streamwise fluidelastic instability is found to be affected by both damping and stiffness mechanisms specifically at low mass-damping value (water flow). This is unlike the established experimental knowledge in the literature as it is known that streamwise fluidelastic instability is only controlled by the stiffness mechanism.

7.3. Original contributions

7.3.1. Numerical investigation of the cross flow fluidelastic forces of two-phase flow in tube bundle

1. The development of a transverse fluidelastic instability numerical model based on the Computational fluid dynamics for the two-phase flow.
2. The production of comprehensive fluidelastic force's data which cover the span of void fraction up to 95% for the parallel triangular array with a pitch-to-diameter ratio of 1.5.

7.3.2. Numerical simulation of streamwise fluidelastic instability of tube bundles subjected to two-phase cross flow

1. The model was enhanced to cover the streamwise fluidelastic instability.
2. Extending the fluidelastic force data to cover forces in the streamwise direction for a parallel triangular array with pitch-to-diameter ratios of 1.3, 1.5, and 1.7.

7.3.3. The prediction of fluidelastic forces in triangular tube bundles subjected to a two-phase flow: The effect of the flow approach angle

1. A more detailed inspection of the air void fraction influence on the fluidelastic forces is provided. It was found that such influence is very critical at very high air void fraction between 99% and 100%. Such high void fraction values may exist at the hot leg side of the U-bend region.

2. The time-averaged pattern of the flow within the triangular tube array at different flow approach angles can be represented by a linear combination of the flow patterns within the standard parallel and normal triangular arrays.
3. An approximate semi-analytical model was developed to predict the fluidelastic forces acting on the tubes at any flow approach angle. The model was validated against generated data from the CFD model. The developed semi-analytical model is a quick and efficient tool to inspect the onset of the fluidelastic instability of the tubes in the U-bend region.

7.3.4. The mechanisms of fluidelastic instability and the effect of frequency detuning in triangular tube bundles subjected to a two-phase flow

1. A procedure to isolate the effect of the damping-controlled and the stiffness-controlled mechanisms was introduced and the corresponding threshold of fluidelastic stability was presented and discussed.
2. The effect of tubes' frequency detuning was investigated for a detuning pattern which corresponds to the curvature of the tubes in the U-bend region.
3. The stabilizing effect of frequency detuning was found to be sensitive to mass-damping parameter and the dominant fluidelastic instability's mechanism in the parallel triangular array.

7.4. Recommendations for future work

The work presented in the research is a step towards a detailed understanding of the fluidelastic instability phenomenon and developing new techniques to accurately predict its onset of instability. The following points are brief recommendations to further enhance the current knowledge of fluidelastic instability.

- This work focused on an air-water mixture to resemble the nature of the two-phase flow. Although such mixture does not allow for a phase change between the gas and liquid phases, the mixture is steam-water in typical steam generators which allows for phase change. It will be a critical enhancement to the developed model to be validated against gas-liquid freon and steam-water mixtures.

- The production of fluidelastic forces' data can be extended to cover the standard square array geometries.
- The developed approximate semi-analytical model for the flow approach angle effect shall be validated against the square array geometries.

Bibliography

- Anderson, B., Hassan, M., & Mohany, A. (2014). Modelling of fluidelastic instability in a square inline tube array including the boundary layer effect. *Journal of Fluids and Structures*, 48, 362–375. <https://doi.org/10.1016/j.jfluidstructs.2014.03.003>
- Axisa, F., Villard, B., Gibert, R. J., & Boheas, M. A. (1985). Vibration of tube bundles subjected to steam-water cross flow: a comparative study of square and triangular pitch arrays. *Transactions of the 8. International Conference on Structural Mechanics in Reactor Technology. Vol. B.*
- Blevins, R. D. (1974). Fluid Elastic Whirling of a Tube Row. *Journal of Pressure Vessel Technology*, 96(4), 263. <https://doi.org/10.1115/1.3454179>
- Blevins, R. D. (1977). Flow-induced vibration. *New York, Van Nostrand Reinhold Co., 1977. 377 P., 1.*
- Carlucci, L. N. (1980). Damping and Hydrodynamic Mass of a Cylinder in Simulated Two-Phase Flow. *Journal of Mechanical Design*, 102(3), 597. <https://doi.org/10.1115/1.3254791>
- Chen, S. S. (1983). Instability Mechanisms and Stability Criteria of a Group of Circular Cylinders Subjected to Cross-Flow. Part I: Theory. *Journal of Vibration Acoustics Stress and Reliability in Design*, 105(1), 51–58. <https://doi.org/10.1115/1.3269066>
- Chen, S. S. (1987). A general theory for dynamic instability of tube arrays in crossflow. *Journal of Fluids and Structures*, 1(1), 35–53. [https://doi.org/10.1016/S0889-9746\(87\)90170-8](https://doi.org/10.1016/S0889-9746(87)90170-8)
- Chen, S. S., & Jendrzejcyk, J. A. (1981). Experiments on fluid elastic instability in tube banks subjected to liquid cross flow. *Journal of Sound and Vibration*, 78(3), 355–381. [https://doi.org/10.1016/S0022-460X\(81\)80145-9](https://doi.org/10.1016/S0022-460X(81)80145-9)
- Cheng, B. (1994). *The mechanisms underlying flow-induced instability of cylinder arrays in cross-flow: An investigation of system parameters.* McGill University.
- Connors, H. J. (1978). Fluidelastic Vibration of Heat Exchanger Tube Arrays. *Journal of*

- Mechanical Design*, 100(2), 347–353. <https://doi.org/10.1115/1.3453921>
- Connors, H. J. (1970). Fluidelastic vibration of tube arrays excited by cross flow. *ASME Symposium on Flow-Induced Vibration in Heat Exchanger*, 42–47.
- de Pedro, B., & Meskell, C. (2018). Sensitivity of the damping controlled fluidelastic instability threshold to mass ratio, pitch ratio and Reynolds number in normal triangular arrays. *Nuclear Engineering and Design*, 331(February), 32–40. <https://doi.org/10.1016/j.nucengdes.2018.02.015>
- de Pedro, B., Parrondo, J., Meskell, C., & Oro, J. F. (2016). CFD modelling of the cross-flow through normal triangular tube arrays with one tube undergoing forced vibrations or fluidelastic instability. *Journal of Fluids and Structures*, 64, 67–86. <https://doi.org/10.1016/j.jfluidstructs.2016.04.006>
- El Bouzidi, S., & Hassan, M. (2015). An investigation of time lag causing fluidelastic instability in tube arrays. *Journal of Fluids and Structures*, 57, 264–276. <https://doi.org/10.1016/j.jfluidstructs.2015.06.005>
- El Bouzidi, S., Hassan, M., Fernandes, L. L., & Mohany, A. (2014). Numerical Characterization of the Area Perturbation and Timelag for a Vibrating Tube Subjected to Cross-Flow. *Volume 4: Fluid-Structure Interaction*, V004T04A047. <https://doi.org/10.1115/PVP2014-28452>
- Elbanhawy, O., Hassan, M., & Mohany, A. (2020). Simulation of motion-dependent fluid forces in fuel bundles. *Nuclear Engineering and Design*, 356, 110373. <https://doi.org/10.1016/j.nucengdes.2019.110373>
- Elhelaly, A., Hassan, M., Mohany, A., & Eid Moussa, S. (2020). Effect of the flow approach angle on the dynamics of loosely-supported tube arrays. *Nuclear Engineering and Design*, 368(February 2019), 110802. <https://doi.org/10.1016/j.nucengdes.2020.110802>
- Feenstra, P., Judd, R. L., & Weaver, D. S. (1995). Fluidelastic Instability in a Tube Array Subjected to Two-Phase R-11 Cross-Flow. *Journal of Fluids and Structures*, 9(7), 747–771. <https://doi.org/10.1006/jfls.1995.1042>
- Feenstra, P., Weaver, D. S., & Judd, R. L. (2000). An improved void fraction model for two-phase cross-flow in horizontal tube bundles. *International Journal of Multiphase Flow*, 26(11), 1851–1873. [https://doi.org/10.1016/S0301-9322\(99\)00118-4](https://doi.org/10.1016/S0301-9322(99)00118-4)

- Feenstra, P., Weaver, D. S., & Judd, R. L. (2002). Modelling two-phase flow-excited damping and fluidelastic instability in tube arrays. *Journal of Fluids and Structures*, 16(6), 811–840. <https://doi.org/10.1006/jfls.2002.0442>
- Feenstra, P., Weaver, D. S., & Nakamura, T. (2003). Vortex shedding and fluidelastic instability in a normal square tube array excited by two-phase cross-flow. *Journal of Fluids and Structures*, 17(6), 793–811. [https://doi.org/10.1016/S0889-9746\(03\)00024-0](https://doi.org/10.1016/S0889-9746(03)00024-0)
- Ferng, Y.-M., & Chang, H.-J. (2008). CFD investigating the impacts of changing operating conditions on the thermal-hydraulic characteristics in a steam generator. *Applied Thermal Engineering*, 28(5–6), 414–422. <https://doi.org/10.1016/j.applthermaleng.2007.05.014>
- Garland, W. J. (2014). The Essential CANDU. In *University Network of Excellence in Nuclear Engineering (UNENE)*. <http://www.nuceng.ca/candu/pdf/TheEssentialCANDU.pdf>
- Hassan, M., Gerber, A., & Omar, H. (2010). Numerical Estimation of Fluidelastic Instability in Tube Arrays. *Journal of Pressure Vessel Technology*, 132(4), 041307. <https://doi.org/10.1115/1.4002112>
- Hassan, M., & Hayder, M. (2008). Modelling of fluidelastic vibrations of heat exchanger tubes with loose supports. *Nuclear Engineering and Design*, 238(10), 2507–2520. <https://doi.org/10.1016/j.nucengdes.2008.05.014>
- Hassan, M., & Mohany, A. (2012). Fluidelastic Instability Modeling of Loosely Supported Multispan U-Tubes in Nuclear Steam Generators. *Journal of Pressure Vessel Technology*, 135(1), 011306. <https://doi.org/10.1115/1.4006854>
- Hassan, M., & Mohany, A. (2016). Simulations of fluidelastic forces and fretting wear in U-bend tube bundles of steam generators: Effect of tube-support conditions. *Wind and Structures*, 23(2), 157–169. <https://doi.org/10.12989/was.2016.23.2.157>
- Hassan, M., & Weaver, D. (2017a). Pitch and Mass Ratio Effects on Transverse and Streamwise Fluidelastic Instability in Parallel Triangular Tube Arrays. *Journal of Pressure Vessel Technology*, 139(6), 061302. <https://doi.org/10.1115/1.4037717>
- Hassan, M., & Weaver, D. (2018). Transverse And Streamwise Fluidelastic Instability In Rotated Square Tube Arrays. *9th International Symposium on Fluid-Structure Interactions, Flow-Sound Interactions, Flow-Induced Vibration & Noise*, 1–8.

- Hassan, M., & Weaver, D. S. (2015). The Effect of Flat Bar Supports on Streamwise Fluidelastic Instability in Heat Exchanger Tube Arrays. *Journal of Pressure Vessel Technology*, 137(6), 061302. <https://doi.org/10.1115/1.4029973>
- Hassan, M., & Weaver, D. S. (2016). Modeling of Streamwise and Transverse Fluidelastic Instability in Tube Arrays. *Journal of Pressure Vessel Technology*, 138(5), 051304. <https://doi.org/10.1115/1.4032817>
- Hassan, M., & Weaver, D. S. (2017b). The Effects of Tube Array Geometry on Fluidelastic Instability in Heat Exchanger Tube Arrays in Cross Flow. *Volume 4: Fluid-Structure Interaction*, V004T04A057. <https://doi.org/10.1115/PVP2017-65901>
- Hibiki, T., & Ishii, M. (2003). One-dimensional drift-flux model for two-phase flow in a large diameter pipe. *International Journal of Heat and Mass Transfer*, 46(10), 1773–1790. [https://doi.org/10.1016/S0017-9310\(02\)00473-8](https://doi.org/10.1016/S0017-9310(02)00473-8)
- Hirota, K., Nakamura, T., Kasahara, J., Mureithi, N. W., Kusakabe, T., & Takamatsu, H. (2002). Dynamics Of An In-Line Tube Array Subjected To Steam–Water Cross-Flow. Part III: Fluidelastic Instability Tests And Comparison With Theory. *Journal of Fluids and Structures*, 16(2), 153–173. <https://doi.org/10.1006/jfls.2001.0408>
- Inada, F., Kawamura, K., & Yasuo, A. (1996). Fluid-elastic force measurements acting on a tube bundle in two-phase cross flow. In *Flow-induced vibration-1996. PVP-Volume 328*.
- Inada, F., Kawamura, K., Yasuo, A., & Yoneda, K. (2002). An experimental study on the fluidelastic two-phase cross-flow. *Journal of Fluids and Structures*, 16(7), 891–907. <https://doi.org/10.1006/jfls.2002.0460>
- Ishii, M., & Kim, S. (2001). Micro four-sensor probe measurement of interfacial area transport for bubbly flow in round pipes. *Nuclear Engineering and Design*, 205(1–2), 123–131. [https://doi.org/10.1016/S0029-5493\(00\)00350-2](https://doi.org/10.1016/S0029-5493(00)00350-2)
- Ishii, Mamoru, & Zuber, N. (1979). Drag coefficient and relative velocity in bubbly, droplet or particulate flows. *AIChE Journal*, 25(5), 843–855. <https://doi.org/10.1002/aic.690250513>
- Iwaki, C., Cheong, K. H., Monji, H., & Matsui, G. (2005). Vertical, Bubbly, Cross-Flow Characteristics over Tube Bundles. *Experiments in Fluids*, 39(6), 1024–1039. <https://doi.org/10.1007/s00348-005-0036-2>

- Janzen, V. P., Hagberg, E. G., Pettigrew, M. J., & Taylor, C. E. (2005). Fluidelastic Instability and Work-Rate Measurements of Steam-Generator U-Tubes in Air–Water Cross-Flow. *Journal of Pressure Vessel Technology*, 127(1), 84. <https://doi.org/10.1115/1.1849229>
- Khalifa, A., Weaver, D., & Ziada, S. (2013). Modeling of the phase lag causing fluidelastic instability in a parallel triangular tube array. *Journal of Fluids and Structures*, 43, 371–384. <https://doi.org/10.1016/j.jfluidstructs.2013.09.014>
- Lever, J. H., & Weaver, D. S. (1982). A Theoretical Model for Fluid-Elastic Instability in Heat Exchanger Tube Bundles. *Journal of Pressure Vessel Technology*, 104(3), 147. <https://doi.org/10.1115/1.3264196>
- Lever, J. H., & Weaver, D. S. (1986). On the stability of heat exchanger tube bundles, part I: Modified theoretical model. *Journal of Sound and Vibration*, 107(3), 375–392. [https://doi.org/10.1016/S0022-460X\(86\)80114-6](https://doi.org/10.1016/S0022-460X(86)80114-6)
- Mitra, D., Dhir, V. K., & Catton, I. (2009). Fluid-elastic instability in tube arrays subjected to air-water and steam-water cross-flow. *Journal of Fluids and Structures*, 25(7), 1213–1235. <https://doi.org/10.1016/j.jfluidstructs.2009.07.002>
- Mohany, A., Arthurs, D., Bolduc, M., Hassan, M., & Ziada, S. (2014). Numerical and experimental investigation of flow-acoustic resonance of side-by-side cylinders in a duct. *Journal of Fluids and Structures*, 48, 316–331. <https://doi.org/10.1016/j.jfluidstructs.2014.03.015>
- Mohany, A., Feenstra, P., Janzen, V. P., & Richard, R. (2009). Experimental Modeling of Flow-Induced Vibration of Multi-Span U-Tubes in a CANDU Steam Generator. *Sixth CNS International Steam Generator Conference on “Management of Real-Life Equipment Conditions and Solutions for the Future.”*
- Mohany, A., Janzen, V. P., Feenstra, P., & King, S. (2012). Experimental and Numerical Characterization of Flow-Induced Vibration of Multispan U-tubes. *Journal of Pressure Vessel Technology*, 134(1), 011301. <https://doi.org/10.1115/1.4004796>
- Moran, J. E., & Weaver, D. S. (2013). On the Damping in Tube Arrays Subjected to Two-Phase Cross-Flow. *Journal of Pressure Vessel Technology*, 135(3), 030906. <https://doi.org/10.1115/1.4023421>
- Mureithi, N. W., Zhang, C., Ruël, M., & Pettigrew, M. J. (2005). Fluidelastic instability tests on

- an array of tubes preferentially flexible in the flow direction. *Journal of Fluids and Structures*, 21(1 SPEC. ISS.), 75–87. <https://doi.org/10.1016/j.jfluidstructs.2005.03.010>
- Nakamura, T., Fujita, K., Kawanishi, K., Yamaguchi, N., & Tsuge, A. (1995). Study on the Vibrational Characteristics of a Tube Array Caused by Two-Phase Flow. Part II: Fluidelastic Vibration. *Journal of Fluids and Structures*, 9(5), 539–562. <https://doi.org/10.1006/jfls.1995.1030>
- Nakamura, T., Fujita, Y., & Sumitani, T. (2014). Study on In-Flow Fluidelastic Instability of Triangular Tube Arrays Subjected to Air Cross Flow. *Journal of Pressure Vessel Technology*, 136(5), 051310. <https://doi.org/10.1115/1.4027618>
- Nakamura, T., Nishimura, K., Fujita, Y., & Kohara, C. (2011). Study on In-Flow Vibration of Cylinder Arrays Caused by Cross Flow. *ASME 2011 Pressure Vessels and Piping Conference: Volume 4*, 69–76. <https://doi.org/10.1115/PVP2011-57068>
- Nakamura, T., & Tsujita, T. (2017). Study on the Stream-Wise Fluidelastic Instability of Rotated Square Arrays of Circular Cylinders Subjected on Cross-Flow. *Volume 4: Fluid-Structure Interaction*, V004T04A025. <https://doi.org/10.1115/PVP2017-65162>
- Nakamura, T., Tsujita, T., & Usuki, K. (2016). Study on in-flow fluidelastic instability of normal triangular array. *11th International Conference on Flow-Induced Vibration, Hague*.
- Naudascher, E., & Rockwell, D. (2012). *Flow-induced vibrations: an engineering guide*. Courier Corporation.
- Olala, S., & Mureithi, N. W. (2016). Prediction of Streamwise Fluidelastic Instability of a Tube Array in Two-Phase Flow and Effect of Frequency Detuning. *Journal of Pressure Vessel Technology*, 139(3), 031301. <https://doi.org/10.1115/1.4034467>
- Olala, S., & Mureithi, N. W. (2015). Streamwise Dynamics of a Tube Array Subjected to Two-Phase Cross-Flows. *Volume 4: Fluid-Structure Interaction*, V004T04A044. <https://doi.org/10.1115/PVP2015-45714>
- Païdoussis, M. P. (1983). A review of flow-induced vibrations in reactors and reactor components. *Nuclear Engineering and Design*, 74(1), 31–60. [https://doi.org/10.1016/0029-5493\(83\)90138-3](https://doi.org/10.1016/0029-5493(83)90138-3)
- Païdoussis, M., Price, S., & De Langre, E. (2010). *Fluid-structure interactions: cross-flow-induced*

instabilities. Cambridge University Press.

- Pettigrew, M. J., Carlucci, L. N., Taylor, C. E., & Fisher, N. J. (1991). Flow-induced vibration and related technologies in nuclear components. *Nuclear Engineering and Design*, 131(1), 81–100. [https://doi.org/10.1016/0029-5493\(91\)90319-D](https://doi.org/10.1016/0029-5493(91)90319-D)
- Pettigrew, M. J., & Taylor, C. E. (1991). Fluidelastic Instability of Heat Exchanger Tube Bundles: Review and Design Recommendations. *Journal of Pressure Vessel Technology*, 113(2), 242–256. <https://doi.org/10.1115/1.2928752>
- Pettigrew, M. J., & Taylor, C. E. (1994). Two-phase flow-induced vibration: An overview (survey paper). *Journal of Pressure Vessel Technology*, 116(3), 233–253. <https://doi.org/10.1115/1.2929583>
- Pettigrew, M. J., & Taylor, C. E. (2004). Damping of heat exchanger tubes in two-phase flow: Review and design guidelines. *Journal of Pressure Vessel Technology, Transactions of the ASME*, 126(4), 523–533. <https://doi.org/10.1115/1.1806443>
- Pettigrew, M. J., Taylor, C. E., Janzen, V. P., & Whan, T. (2002). Vibration Behavior of Rotated Triangular Tube Bundles in Two-Phase Cross Flows. *Journal of Pressure Vessel Technology*, 124(2), 144. <https://doi.org/10.1115/1.1462045>
- Pettigrew, M. J., Taylor, C. E., Jong, J. H., & Currie, I. G. (1995). Vibration of a Tube Bundle in Two-Phase Freon Cross-Flow. *Journal of Pressure Vessel Technology*, 117(4), 321. <https://doi.org/10.1115/1.2842130>
- Pettigrew, M. J., Taylor, C. E., & Kim, B. S. (1989). Vibration of Tube Bundles in Two-Phase Cross-Flow: Part 1—Hydrodynamic Mass and Damping. *Journal of Pressure Vessel Technology*, 111(4), 466. <https://doi.org/10.1115/1.3265705>
- Pettigrew, M. J., Taylor, C. E., & Kim, B. S. (2001). The Effects of Bundle Geometry on Heat Exchanger Tube Vibration in Two-Phase Cross Flow. *Journal of Pressure Vessel Technology*, 123(4), 414. <https://doi.org/10.1115/1.1388236>
- Pettigrew, M. J., Tromp, P. G., Taylor, C. E., & Kim, B. S. (1989). Vibration of Tube Bundles in Two-Phase Cross-Flow: Part 2—Fluid-Elastic Instability. *Journal of Pressure Vessel Technology*, 111(4), 478. <https://doi.org/10.1115/1.3265706>
- Pettigrew, M. J., Zhang, C., Mureithi, N. W., & Pamfil, D. (2005). Detailed flow and force

- measurements in a rotated triangular tube bundle subjected to two-phase cross-flow. *Journal of Fluids and Structures*, 20(4), 567–575. <https://doi.org/10.1016/j.jfluidstructs.2005.02.007>
- Price, S. J., & Kuran, S. (1991). Fluidelastic stability of a rotated square array with multiple flexible cylinders, subject to cross-flow. *Journal of Fluids and Structures*, 5(5), 551–572. [https://doi.org/10.1016/S0889-9746\(05\)80005-2](https://doi.org/10.1016/S0889-9746(05)80005-2)
- Price, S. J., & Paidoussis, M. P. (1983). Fluidelastic Instability of an Infinite Double Row of Circular Cylinders Subject to a Uniform Cross-Flow. *Journal of Vibration, Acoustics, Stress, and Reliability in Design*, 105(1), 59–66. <https://doi.org/10.1115/1.3269067>
- Price, S. J., & Paidoussis, M. P. (1984). An improved mathematical model for the stability of cylinder rows subject to cross-flow. *Journal of Sound and Vibration*, 97(4), 615–640. [https://doi.org/10.1016/0022-460X\(84\)90512-1](https://doi.org/10.1016/0022-460X(84)90512-1)
- Roberts, B. W. (1962). *Low frequency, self-excited vibration in a row of circular cylinders mounted in an airstream*. University of Cambridge.
- Roberts, B. W. (1966). *Low Frequency, Aeroelastic Vibrations in a Cascade of Circular Cylinders*. Institution of Mechanical Engineers.
- Romberg, O., & Popp, K. (1999). Fluid-Damping Controlled Instability in Tube Bundles Subjected to Air Cross-Flow. *Combustion, m*, 285–300.
- Sadek, O., Mohany, A., & Hassan, M. (2018). Numerical investigation of the cross flow fluidelastic forces of two-phase flow in tube bundle. *Journal of Fluids and Structures*, 79, 171–186. <https://doi.org/10.1016/j.jfluidstructs.2017.11.009>
- Sadek, O., Mohany, A., & Hassan, M. (2020). Numerical simulation of streamwise fluidelastic instability of tube bundles subjected to two-phase cross flow. *Journal of Fluids and Structures*, 92, 102816. <https://doi.org/10.1016/j.jfluidstructs.2019.102816>
- Sauter, J. (1926). *Die Grössenbestimmung der im Gemischnebel von Verbrennungskraftmaschinen vorhandenen Brennstoffteilchen* (1926th ed.). VDI-Verlag. <https://books.google.ca/books?id=5pcinQEACAAJ>
- Sawadogo, T., & Mureithi, N. (2014). Fluidelastic instability study in a rotated triangular tube array subject to two-phase cross-flow. Part I: Fluid force measurements and time delay extraction. *Journal of Fluids and Structures*, 49, 1–15.

<https://doi.org/10.1016/j.jfluidstructs.2014.02.004>

- Schlegel, J., Hibiki, T., & Ishii, M. (2010). Development of a comprehensive set of drift-flux constitutive models for pipes of various hydraulic diameters. *Progress in Nuclear Energy*, 52(7), 666–677. <https://doi.org/10.1016/j.pnucene.2010.03.007>
- Scott, P. M. (1987). *Flow Visualization of Cross-Flow-Induced Vibrations in Tube Arrays*. McMaster University.
- Selima, Y., Hassan, M., Mohany, A., & Ahmed, W. (2021). Modelling of fluidelastic instability in tube bundles under two-phase bubbly flow conditions. *Journal of Fluids and Structures*, 103, 103256. <https://doi.org/10.1016/j.jfluidstructs.2021.103256>
- Shinde, V., Longatte, E., & Baj, F. (2015). Large Eddy Simulation of Fluid-Elastic Instability in Square Normal Cylinder Array. *Volume 5: High-Pressure Technology; Rudy Scavuzzo Student Paper Competition and 23rd Annual Student Paper Competition; ASME NDE Division*, V005T09A005. <https://doi.org/10.1115/PVP2015-45136>
- Shinde, V., Marcel, T., Hoarau, Y., Deloze, T., Harran, G., Baj, F., Cardolaccia, J., Magnaud, J. P., Longatte, E., & Braza, M. (2014). Numerical simulation of the fluid-structure interaction in a tube array under cross flow at moderate and high Reynolds number. *Journal of Fluids and Structures*, 47, 99–113. <https://doi.org/10.1016/j.jfluidstructs.2014.02.013>
- Spalart, P., & Allmaras, S. (1992). A one-equation turbulence model for aerodynamic flows. *30th Aerospace Sciences Meeting and Exhibit*, 439. <https://doi.org/10.2514/6.1992-439>
- Sun, Z., Sang, W., & Zhang, H. (2009). Measurement of pressure fluctuation in gas-liquid two-phase vortex street. *Journal of Physics: Conference Series*, 147, 012019. <https://doi.org/10.1088/1742-6596/147/1/012019>
- Tanaka, H., & Takahara, S. (1981). Fluid elastic vibration of tube array in cross flow. *Journal of Sound and Vibration*, 77(1), 19–37. [https://doi.org/10.1016/S0022-460X\(81\)80005-3](https://doi.org/10.1016/S0022-460X(81)80005-3)
- Tixier, E., Béguin, C., Étienne, S., Pelletier, D., Hay, A., & Ricciardi, G. (2015). Fluidelastic Instability in Tube Arrays Subject to Two-Phase Cross Flow: A Porous Medium Approach. *Volume 4: Fluid-Structure Interaction*, V004T04A047. <https://doi.org/10.1115/PVP2015-45931>
- Violette, R., Pettigrew, M. J., & Mureithi, N. W. (2006). Fluidelastic Instability of an Array of

- Tubes Preferentially Flexible in the Flow Direction Subjected to Two-Phase Cross Flow. *Journal of Pressure Vessel Technology*, 128(1), 148. <https://doi.org/10.1115/1.2138064>
- Weaver, D. S., & Abd-Rabbo, A. (1985). A Flow Visualization Study of a Square Array of Tubes in Water Crossflow. *Journal of Fluids Engineering*, 107(3), 354–362. <https://doi.org/10.1115/1.3242491>
- Weaver, D. S., & Fitzpatrick, J. A. (1988). A review of cross-flow induced vibrations in heat exchanger tube arrays. *Journal of Fluids and Structures*, 2(1), 73–93. [https://doi.org/10.1016/S0889-9746\(88\)90137-5](https://doi.org/10.1016/S0889-9746(88)90137-5)
- Weaver, D. S., & Koroyannakis, D. (1983). Flow-Induced Vibrations of Heat Exchanger U-Tubes: A Simulation to Study the Effects of Asymmetric Stiffness. *ASME Journal of Pressure Vessel Technology*, 81, 67–75. <https://doi.org/10.1115/1.3269069>
- Weaver, D. S., & Schneider, W. (1983). The Effect of Flat Bar Supports on the Crossflow Induced Response of Heat Exchanger U-Tubes. *Journal of Engineering for Power*, 105(4), 775–781. <https://doi.org/10.1115/1.3227481>
- Weaver, D. S., & Yeung, H. C. (1983). Approach flow direction effects on the cross-flow induced vibrations of a square array of tubes. *Journal of Sound and Vibration*, 87(3), 469–482. [https://doi.org/10.1016/0022-460X\(83\)90474-1](https://doi.org/10.1016/0022-460X(83)90474-1)
- Weaver, D. S., Ziada, S., Au-Yang, M. K., Chen, S. S., Païdoussis, M. P., & Pettigrew, M. J. (2000). Flow-induced vibrations in power and process plant components - progress and prospects. *Journal of Pressure Vessel Technology, Transactions of the ASME*, 122(3), 339–348. <https://doi.org/10.1115/1.556190>
- Wu, Q., Kim, S., Ishii, M., & Beus, S. G. (1998). One-group interfacial area transport in vertical bubbly flow. *International Journal of Heat and Mass Transfer*, 41(8–9), 1103–1112. [https://doi.org/10.1016/S0017-9310\(97\)00167-1](https://doi.org/10.1016/S0017-9310(97)00167-1)
- Yetisir, M., & Weaver, D. S. (1993). An Unsteady Theory For Fluidelastic Instability in an Array of Flexible Tubes in Cross-Flow. Part I: Theory. *Journal of Fluids and Structures*, 7(7), 751–766. <https://doi.org/10.1006/jfls.1993.1044>
- Yeung, H. C., & Weaver, D. S. (1983). The Effect of Approach Flow Direction on the Flow-Induced Vibrations of a Triangular Tube Array. *Journal of Vibration Acoustics Stress and*

Reliability in Design, 105(1), 76. <https://doi.org/10.1115/1.3269070>

- Zdravkovich, M. M., & Stonebanks, K. L. (1990). Intrinsically nonuniform and metastable flow in and behind tube arrays. *Journal of Fluids and Structures*, 4(3), 305–319. [https://doi.org/10.1016/S0889-9746\(05\)80017-9](https://doi.org/10.1016/S0889-9746(05)80017-9)
- Zhang, C., Pettigrew, M. J., & Mureithi, N. W. (2007). Vibration Excitation Force Measurements in a Rotated Triangular Tube Bundle Subjected to Two-Phase Cross Flow. *Journal of Pressure Vessel Technology*, 129(1), 21. <https://doi.org/10.1115/1.2388996>
- Ziada, S., Hassan, M., & Gelbe, H. (2018). Vibrations in heat exchanger tube bundles. In P. Stephan, D. Mewes, S. Kabelac, M. Kind, K. Schaber, & T. Wetzel (Eds.), *VDI-Wärmeatlas : Fachlicher Träger VDI-Gesellschaft Verfahrenstechnik und Chemieingenieurwesen* (pp. 1–43). Springer Berlin Heidelberg. https://doi.org/10.1007/978-3-662-52991-1_115-1
- Zuber, N., & Findlay, J. A. (1965). Average Volumetric Concentration in Two-Phase Flow Systems. *Journal of Heat Transfer*, 87(4), 453. <https://doi.org/10.1115/1.3689137>

Appendix A



This appendix contains the permission given to the author to use the journal papers as part(s) of this thesis in accordance with the Journal of Fluids and Structures' copyrights license agreement.


A.1. Numerical investigation of the cross flow fluidelastic forces of two-phase flow in tube bundle


The following Fig. A.1 is a screenshot from the publisher "Elsevier", which allows the author to use the following article as part of this thesis.


Article


Sadek, O., Mohany, A., & Hassan, M. (2018). Numerical investigation of the cross flow fluidelastic forces of two-phase flow in tube bundle. *Journal of Fluids and Structures*, 79, 171-186. <https://doi.org/10.1016/j.jfluidstructs.2017.11.009>





 Home

 Help

 Email Support

 Sign in

 Create Account



Numerical investigation of the cross flow fluidelastic forces of two-phase flow in tube bundle

Author: Omar Sadek, Atef Mohany, Marwan Hassan
Publication: Journal of Fluids and Structures
Publisher: Elsevier
Date: May 2018

© 2017 Published by Elsevier Ltd.

Journal Author Rights

Please note that, as the author of this Elsevier article, you retain the right to include it in a thesis or dissertation, provided it is not published commercially. Permission is not required, but please ensure that you reference the journal as the original source. For more information on this and on your other retained rights, please visit: <https://www.elsevier.com/about/our-business/policies/copyright#Author-rights>

BACK

CLOSE WINDOW

Figure A.1: Screenshot of permission to use the presented journal article in Chapter 3.

A.2. Numerical simulation of streamwise fluidelastic instability of tube bundles subjected to two-phase cross flow

The following Fig. A.2 is a screenshot from the publisher “Elsevier”, which allows the author to use the following article as part of this thesis.

Article

Sadek, O., Mohany, A., & Hassan, M. (2020). Numerical simulation of streamwise fluidelastic instability of tube bundles subjected to two-phase cross flow. *Journal of Fluids and Structures*, 92, 102816. <https://doi.org/10.1016/j.jfluidstructs.2019.102816>



 Home

 Help

 Email Support

 Sign in

 Create Account



Numerical simulation of streamwise fluidelastic instability of tube bundles subjected to two-phase cross flow

Author: O. Sadek, A. Mohany, M. Hassan
Publication: Journal of Fluids and Structures
Publisher: Elsevier
Date: January 2020

© 2019 Elsevier Ltd. All rights reserved.

Journal Author Rights

Please note that, as the author of this Elsevier article, you retain the right to include it in a thesis or dissertation, provided it is not published commercially. Permission is not required, but please ensure that you reference the journal as the original source. For more information on this and on your other retained rights, please visit: <https://www.elsevier.com/about/our-business/policies/copyright#Author-rights>

BACK

CLOSE WINDOW

Figure A.2: Screenshot of permission to use the presented journal article in Chapter 4.